

A Search for L/T Transition Dwarfs With Pan-STARRS1 and *WISE*. II. L/T Transition Atmospheres and Young Discoveries

William M. J. Best^{1,6}, Michael C. Liu^{1,6}, Eugene A. Magnier¹, Niall R. Deacon², Kimberly M. Aller^{1,6}, Joshua Redstone³, W. S. Burgett⁴, K. C. Chambers¹, P. Draper⁵, H. Flewelling¹, K. W. Hodapp¹, N. Kaiser¹, N. Metcalfe⁵, J. L. Tonry¹, R. J. Wainscoat¹, C. Waters¹

ABSTRACT

The evolution of brown dwarfs from L to T spectral types is one of the least understood aspects of the ultracool population, partly for lack of a large, well-defined, and well-characterized sample in the L/T transition. To improve the existing census, we have searched $\approx 28,000$ deg² using the Pan-STARRS1 and *Wide-field Infrared Survey Explorer* surveys for L/T transition dwarfs within 25 pc. We present 130 ultracool dwarf discoveries with estimated distances $\approx 9 - 130$ pc, including 21 that were independently discovered by other authors and 3 that were previously identified as photometric candidates. Seventy-nine of our objects have near-IR spectral types of L6–T4.5, the most L/T transition dwarfs from any search to date, and we have increased the census of L9–T1.5 objects within 25 pc by over 50%. The color distribution of our discoveries provides further evidence for the “L/T gap,” a deficit of objects with $(J - K)_{\text{MKO}} \approx 0.0 - 0.5$ mag in the L/T transition, and thus reinforces the idea that the transition from cloudy to clear photospheres occurs rapidly. Among our discoveries are 31 candidate binaries based on their low-resolution spectral features. Two of these candidates are common proper motion companions to nearby main sequence stars; if confirmed as binaries, these would be rare benchmark systems with the potential to stringently test ultracool evolutionary models. Our search also serendipitously identified 23 late-M and L dwarfs with spectroscopic signs of low gravity implying youth, including 10 with VL-G or INT-G gravity

¹Institute for Astronomy, University of Hawaii, 2680 Woodlawn Drive, Honolulu, HI 96822, USA; wbest@ifa.hawaii.edu

²Centre for Astrophysics Research, University of Hertfordshire, College Lane Campus, Hatfield AL10 9AB, UK

³Equatune Labs, 89 Antrim Street, #2, Cambridge, MA 02139, USA

⁴GMTO Corporation, 251 S. Lake Ave., Suite 300, Pasadena, CA 91101, USA

⁵Department of Physics, Durham University, South Road, Durham DH1 3LE, UK

⁶Visiting Astronomer at the Infrared Telescope Facility, which is operated by the University of Hawaii under Cooperative Agreement no. NNX-08AE38A with the National Aeronautics and Space Administration, Science Mission Directorate, Planetary Astronomy Program.

classifications and another 13 with indications of low gravity whose spectral types or modest spectral signal-to-noise ratio do not allow us to assign formal classifications. Finally, we identify 10 candidate members of nearby young moving groups (YMG) with spectral types L7–T4.5, including three showing spectroscopic signs of low gravity. If confirmed, any of these would be among the coolest known YMG members and would help to determine the effective temperature at which young brown dwarfs cross the L/T transition.

Subject headings: brown dwarfs — stars: late-type — stars: atmospheres — stars: kinematics and dynamics — binaries: general

1. Introduction

Over the past 20 years some 1,500 brown dwarfs have been discovered in the field, yet fundamental questions about their formation, evolution, and atmospheres remain. Without sustained hydrogen fusion in their cores, brown dwarfs cool continuously, creating an observational degeneracy between their masses, ages and luminosities. Their photospheres are dominated by molecules and dusty condensates, and undergo significant chemical changes as they cool (e.g., Burrows et al. 2001). The relationship between the observable properties (fluxes and spectra) and the underlying physical properties (masses, ages, metallicities, and gravities) of ultracool dwarfs is therefore complex and challenging to disentangle, and evolutionary trends are difficult to identify.

This is particularly true in the L/T transition (spectral types \approx L6–T4.5), where spectral features undergo significant changes and near-infrared colors become bluer by ≈ 2 magnitudes over a narrow range of effective temperature ($T_{\text{eff}} \approx 1400 - 1200$ K; Golimowski et al. 2004; Stephens et al. 2009). These changes are thought to arise from the depletion of thick condensate clouds as brown dwarfs cool (e.g., Allard et al. 2001; Burrows et al. 2006; Saumon & Marley 2008). Several scenarios have been proposed wherein condensate clouds thin gradually, rain out suddenly, or break up (e.g., Ackerman & Marley 2001; Knapp et al. 2004; Tsuji 2005; Marley et al. 2010). The process is still not well understood, however, and state-of-the-art evolutionary and atmospheric models typically yield inaccurate luminosities and inconsistent temperatures for L/T objects with dynamical masses and/or age determinations (e.g., Dupuy et al. 2009; Liu et al. 2010; Dupuy et al. 2014). Color-magnitude diagrams with accurate luminosities are still rather sparsely populated in the L/T transition (Dupuy & Liu 2012), hindering our ability to test the models.

A large and well-defined sample is a necessary starting point, but L/T transition dwarfs are known to be more elusive than those with higher and lower effective temperatures. At optical wavelengths, L/T transition dwarfs are faint. In the near-infrared, where they are brightest, their colors make them difficult to distinguish from low-mass stars (e.g., Reid et al. 2008). The most productive previous searches so far each focused on $\lesssim 10\%$ of the sky: Chiu et al. (2006) used the Sloan Digital Sky Survey (SDSS; York et al. 2000) to find 46 L6–T4.5 dwarfs over $\approx 3,500$ deg²,

and Marocco et al. (2015) found 48 L6–T4.5 dwarfs in $\approx 4,000 \text{ deg}^2$ by cross-matching the UKIRT Infrared Deep Sky Survey (UKIDSS; Lawrence et al. 2007) Large Area Survey with SDSS. What has been missing is an all-sky search specifically targeting nearby, bright L/T transition dwarfs.

To address this deficiency, we have conducted an extensive search with these key features: (1) We used the new Pan-STARRS1 Survey (PS1; Kaiser et al. 2010) cross-matched with the Wide-Field Infrared Survey Explorer (*WISE*; Wright et al. 2010) All-sky Release, thereby exploiting the combined broad wavelength coverage of these optical and mid-infrared surveys; (2) we searched $\approx 28,000 \text{ deg}^2$, nearly the full area of the PS1 3π survey; and (3) we searched to within 3° of the Galactic plane, whereas most previous searches stopped at $b = 10^\circ$ or $b = 15^\circ$ (e.g., Cruz et al. 2003; Scholz et al. 2011). In Best et al. (2013, hereinafter Paper I), we presented seven initial discoveries from our search, all bright L/T transition dwarfs within 15 pc. In this paper, we present the complete results of our search, including 79 total L/T transition dwarfs and 23 young or potentially young late-M and L dwarfs.

We describe our search in Section 2 and our observations in Section 3. In Section 4 we present the results of our search, including descriptions of interesting individual objects. In Section 5 we discuss implications of our discoveries for evolutionary models of the L/T transition. We discuss our young discoveries in more detail in Section 6 and summarize our findings in Section 7.

2. Search Method

2.1. Input Catalogs

The PS1 3π survey (K. C. Chambers et al., in preparation) has obtained an average of ≈ 12 epochs of imaging in five optical bands ($g_{P1}, r_{P1}, i_{P1}, z_{P1}, y_{P1}$) with a 1.8-meter wide-field telescope on Haleakala, Maui, covering the entire sky north of -30° declination. Images were processed nightly through the Image Processing Pipeline (IPP; Magnier 2006, 2007; Magnier et al. 2008), with photometry on the AB magnitude scale (Tonry et al. 2012). Imaging began in May 2010 and concluded in March 2014. We conducted our search using PS1/IPP Processing Version 1 photometry, and constructed object names according to the PS1 convention using object coordinates as of January 2012. The *WISE* All-sky Source Catalog (Cutri et al. 2012) comprises data taken between January and August 2010 in four mid-infrared bands: *W1* ($3.6 \mu\text{m}$), *W2* ($4.5 \mu\text{m}$), *W3* ($12 \mu\text{m}$), and *W4* ($22 \mu\text{m}$).

2.2. Search Parameters

Our search is described in detail in Paper I. Briefly, we merged all PS1 detections through January 2012 with the *WISE* All-sky catalog using a $3.0''$ matching radius. We removed objects within 3° of the Galactic plane and in the heavily reddened areas of the sky defined by Cruz et al.

(2003), except for objects in these regions for which PS1 reported a proper motion with $S/N > 3$. We searched between $\delta = -30^\circ$ (the southern limit of PS1) and $\delta = +70^\circ$ (the northern limit of the NASA Infrared Telescope Facility (IRTF), which we used for spectroscopic follow-up). We identified candidate L/T dwarfs using a suite of quality and color cuts applied to our merged PS1+*WISE* database. After visually screening these candidates using images from PS1, *WISE*, and the Two Micron All Sky Survey (2MASS; Skrutskie et al. 2006), we obtained near-infrared photometry from 2MASS, UKIDSS, and our own observations (Section 3.1), and used this to apply a final screening based on colors and magnitudes. We summarize our photometric criteria here:

1. Detected in at least two separate y_{P1} frames with $S/N > 5$ in each.
2. Good quality photometry in y_{P1} , no saturated objects or cosmic rays.
3. No more than one total detection in either g_{P1} or r_{P1} .
4. $i_{P1} - z_{P1} \geq 1.8$ mag (only applied when the i_{P1} and z_{P1} photometry for an object met the same quality standards required for y_{P1}).
5. $i_{P1} - y_{P1} \geq 2.8$ mag (only applied when i_{P1} photometry met the same quality standards required for y_{P1}).
6. $z_{P1} - y_{P1} \geq 0.6$ mag (only applied when z_{P1} photometry met the same quality standards required for y_{P1}).
7. $W1$ and $W2$ detections have $S/N > 2$ (for most candidates, PS1 establishes the sensitivity limit).
8. $W1$ and $W2$ detections are point sources, not saturated, and unlikely to be variable.
9. $y_{P1} - W1 \geq 3.0$ mag.
10. $W1 - W2 \geq 0.4$ mag.
11. $W2 - W3 \leq 2.5$ mag.
12. $y_{P1} - J_{2MASS} \geq 1.8$ mag or $y_{P1} - J_{MKO} \geq 1.9$ mag.

We then obtained and classified near-IR spectra for 142 candidates using standard procedures described in Section 3. In Table 1 we present the PS1 and *WISE* photometry for the objects we observed spectroscopically, and Table 2 shows their near-infrared photometry. We did not observe objects also found by other concurrent PS1 searches for ultracool dwarfs (M. C. Liu et al., in preparation).

2.3. A *WISE* Photometric Criterion for L/T Transition Dwarfs Within 25 pc

Prior to obtaining spectra for our candidates, we used photometry to estimate distances. In Paper I, we noted that y_{P1} absolute magnitudes are roughly flat across the L/T transition, and we identified $y_{P1} = 19.3$ mag as a limit for single objects expected to lie within 25 pc. We therefore used $y_{P1} < 19.3$ mag to prioritize candidates for spectroscopic observations (though in the end, we did observe a few objects with $y_{P1} > 19.3$ mag.) However, some of our first spectroscopic confirmations proved to be L/T transition dwarfs with spectrophotometric distances of 30 – 35 pc and earlier L dwarfs at greater distances, so we sought a better criterion than the y_{P1} cutoff.

We examined the relationships between colors and magnitudes in the PS1, 2MASS, and *WISE* bands and the distances to ultracool dwarfs with known parallaxes from Dupuy & Liu (2012)¹. We identified an inequality in the $W1$ vs. $W1 - W2$ color-magnitude diagram that selects L/T transition dwarfs with $d < 25$ pc:

$$W1 \leq 2.833 \times (W1 - W2) + 12.667 \text{ mag} \quad (1)$$

This inequality excludes nearly all ultracool dwarfs with trigonometric distances beyond 25 pc for $0.5 \lesssim W1 - W2 \lesssim 1.2$ mag, equivalent to spectral types $\approx L8 - T3.5$ (Figure 1). For earlier and later spectral types, there is still contamination from distant objects, but the relationship helps.

Once we identified this inequality, we used it instead of $y_{P1} < 19.3$ mag to prioritize candidates for spectroscopic follow-up. This increased our rate of success at confirming late-L and T dwarfs within 25 pc, but also meant that our final sample of 142 candidates was heterogeneously selected. If we had used the $W1$ vs. $W1 - W2$ inequality from the beginning of the search, we would have observed almost none of our discoveries with spectral types earlier than $\approx L7$.

3. Observations

3.1. Near-infrared Photometry

Following our initial PS1+*WISE* database search, our candidates all had red-optical (y_{P1} , possibly i_{P1} and z_{P1}) and mid-infrared ($W1$ and $W2$, possibly $W3$) photometry. Our red-optical and mid-IR photometry were drawn from single sources, so we sought a similarly homogenous set of near-IR photometry. The only near-IR survey covering our entire search area is 2MASS, but most of our candidates were too faint to have been well detected ($S/N > 10$) by 2MASS, and $\approx 30\%$ were not detected at all. Thus, we obtained additional near-IR photometry in order to further vet our candidates prior to spectroscopic observations.

¹An updated list can be found in the Database of Ultracool Parallaxes maintained by Trent Dupuy at http://www.as.utexas.edu/~tdupuy/plx/Database_of_Ultracool_P parallaxes.html. Here we used the version posted on 2013-09-09.

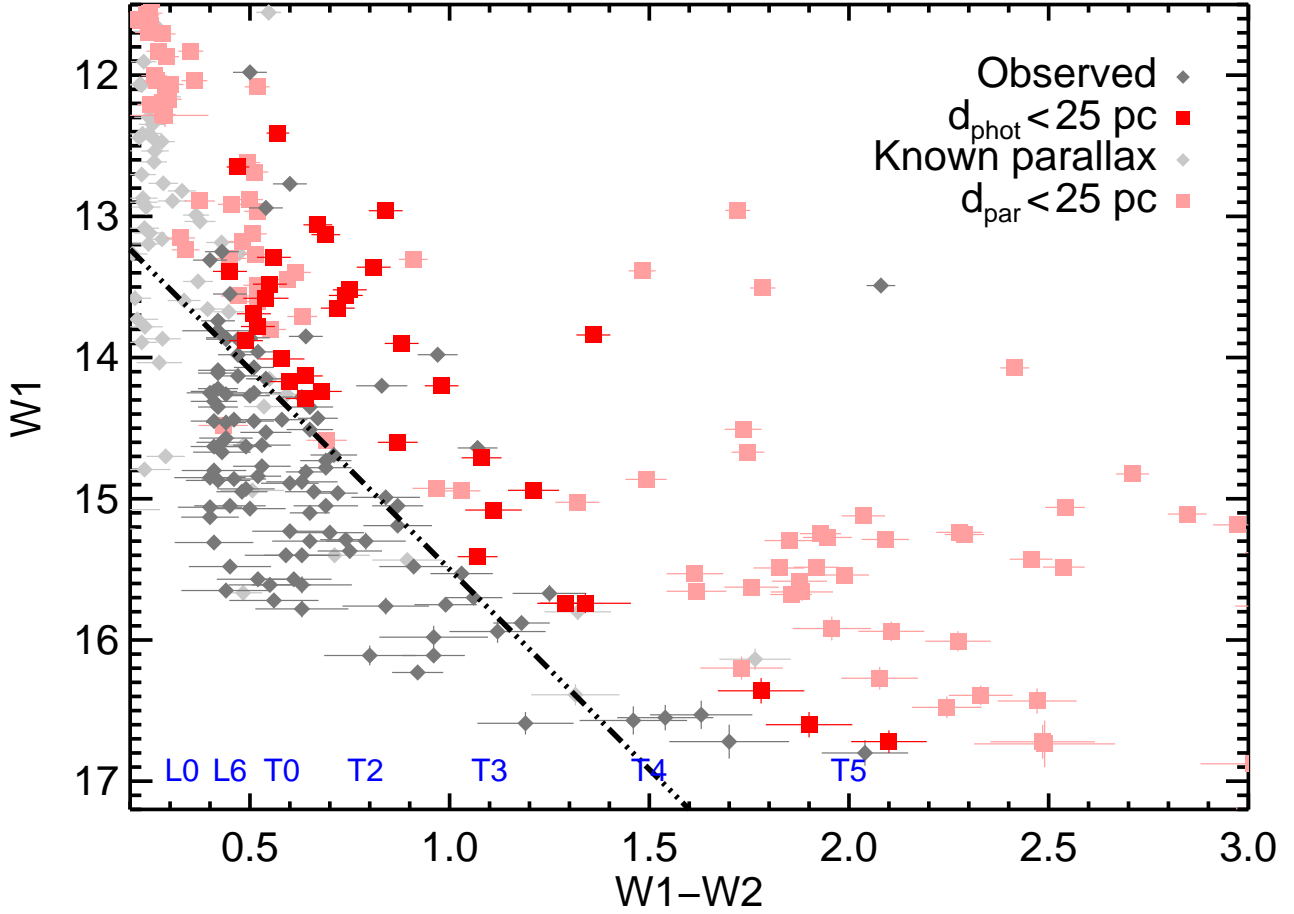


Fig. 1.— $W1$ vs. $W1 - W2$ diagram for known ultracool dwarfs. Objects with known parallaxes (Dupuy & Liu 2012) and within 25 pc are shown as pink squares; those beyond 25 pc are light gray diamonds. Our new discoveries with photometric distances (Section 4) less than 25 pc are plotted with red squares, and those with $d_{\text{phot}} > 25$ pc are dark gray diamonds. Approximate spectral types for $W1 - W2$ colors are indicated in blue along the bottom. The region above and to the right of the black dashed-dotted line, $W1 \leq 2.833 \times (W1 - W2) + 12.667$ mag, includes 100% of our L/T transition discoveries with $d_{\text{phot}} < 25$ pc but only 33% beyond 25 pc.

We therefore searched the UKIDSS Data Release 9 (DR9; Lawrence et al. 2013) and VISTA Hemisphere Survey (VHS; Cross et al. 2012) catalogs for JHK photometry of our candidates on the Mauna Kea Observatories (MKO) filter system (Simons & Tokunaga 2002; Tokunaga et al. 2002). For objects not found in either survey, we obtained follow-up images using WFCAM (Casali et al. 2007) on the 3.8-meter United Kingdom InfraRed Telescope (UKIRT) as part of the UKIRT Service Programme. Observations took place on multiple nights spanning 2010 September to 2013 December. We obtained J band images for all observed targets, as well as H and K bands when time constraints permitted. Integrations were $5 \text{ sec} \times 5$ dithers in J and H bands and $10 \text{ sec} \times 5$ dithers in K band, sufficient to reach $S/N > 20$ in most cases. Data were reduced and calibrated at the Cambridge Astronomical Survey Unit using the WFCAM survey pipeline (Irwin et al. 2004; Hodgkin et al. 2009).

For objects for which we did not obtain both H and K band images, we used our near-IR spectra (Section 3.2) to synthesize photometry in the missing band(s), using our measured J magnitudes to flux-calibrate the synthetic magnitudes. For nine candidates with existing 2MASS photometry for which we did not obtain UKIRT photometry, we synthesized MKO JHK photometry from the near-IR spectra using the corresponding 2MASS magnitudes to calibrate each synthetic magnitude. All observed and synthetic magnitudes are included in Table 2. Altogether we have MKO system JHK photometry for all but one of our 142 candidates.

3.2. Near-infrared Spectroscopy and Spectral Typing

We obtained low-resolution near-IR spectra for our candidates between 2012 July and 2014 January using the NASA Infrared Telescope Facility (IRTF). We used the facility spectrograph SpeX (Rayner et al. 2003) in prism mode with the $0.5''$ ($R \approx 120$) and $0.8''$ ($R \approx 75$) slits. We re-observed eight targets between 2015 January and June with the $0.5''$ slit to obtain higher S/N and assess possible low-gravity spectral signatures (Section 4.4). Details of our observations are listed in Table 3. Contemporaneously with each science target, we observed a nearby A0V star for telluric calibration. All spectra were reduced in the standard way using versions 3.4 and 4.0 of the Spxtool software package (Vacca et al. 2003; Cushing et al. 2004). We aimed for $S/N \gtrsim 30$, sufficient for accurate spectral typing based on overall morphology (i.e., visual comparison of JHK bands).

Spectral typing of our observed objects was performed by visually comparing our spectra to the near-infrared M and L dwarf standards of Kirkpatrick et al. (2010) and T dwarf standards of Burgasser et al. (2006), substituting the T3 standard SDSS J1206+2813 suggested by Liu et al. (2010). When assigning M and L types we followed the procedure of Kirkpatrick et al. (2010), first comparing only the $0.9 - 1.4 \mu\text{m}$ portions of the spectra to evaluate the goodness of fit, and subsequently determining if the object’s $1.4 - 2.4 \mu\text{m}$ flux was unusually red or blue for its spectral type. For T dwarfs, we compared our spectra to the standards over the entire $0.9 - 2.4 \mu\text{m}$ window simultaneously. Our visual typing was able to identify spectra whose features clearly placed them

in between consecutive spectral standards, so we assume a default uncertainty of ± 0.5 sub-types. In cases of larger uncertainty, we use “:” (e.g., spectral type L6:) to indicate an uncertainty of ± 1 sub-type, and “::” to indicate larger uncertainties.

We also determined spectral types for our discoveries using two index-based systems, which enable objective spectral typing based on specific spectral features. Allers & Liu (2013a, hereinafter AL13) developed a system of near-IR indices that are sensitive to spectral type while insensitive to differences in gravity. At least one index is defined for each spectral sub-type spanning M4–L7, so we calculated these indices for our discoveries in that range (M7–L7). Following Aller et al. (2015), we determined the spectral type uncertainties derived from each index by performing Monte Carlo simulations for each object to propagate the measurement errors of our reduced spectra and the rms uncertainties on index-spectral type conversions into the index calculations. We calculated a final index-based spectral type for each object equal to the weighted average of spectral types from all Monte Carlo runs, excluding those that fell outside the valid range for each index.

The second system of near-IR indices we used is that of Burgasser et al. (2006, hereinafter B06), assigning spectral types based on each index using the polynomial fits from Burgasser (2007). The indices were originally designed to classify T dwarfs, but the polynomials for three of the five indices are valid for L dwarfs as well. We calculated a final B06 spectral type for each object as the mean of the individual index-based types, following the approach of Burgasser (2007). For uncertainties, we use the standard deviations of the individual index-based types, which are typically 1.0 – 2.0 subtypes for L dwarfs and 0.5 – 1.5 subtypes for T dwarfs.

Neither of these index-based systems covers the full spectral type range of our objects, whereas visual typing was performed for every object. Therefore, we adopt the visually-assigned types as final spectral types for our discoveries.

4. Results

4.1. Ultracool Discoveries

Our search found 130 ultracool dwarfs, comprising 92% of our 142 spectroscopic targets. Of these, 106 are completely new discoveries. Twenty-one were independently discovered and published by other teams during our search, and 3 are previously identified photometric candidates for which we present the first spectroscopic confirmation. The SpeX prism spectra for 122 of our ultracool discoveries are presented in Figure 2, and their spectral types are listed in Table 4. The remaining eight discoveries are candidate members of the Scorpius-Centaurus Association and the Taurus star-forming region, and their spectra will be presented in a future paper (W. M. J. Best et al., in preparation). We include these eight objects in the summary figures of this paper in order to accurately characterize the overall results of our search. The objects previously published by other teams are listed in Table 5. Seven of our discoveries, all with photometric distances less than 15 pc,

were initially presented in Paper I. We also identified 12 non-ultracool objects including a carbon star, an emission line galaxy, and background stars, which are detailed in Table 6.

Figure 3 shows the spectral type distribution of our ultracool discoveries. These include 79 L6–T4.5 dwarfs ($\approx 55\%$ of our sample), giving us the largest number of L/T transition dwarfs identified by any search to date. Figure 4 compares the spectral type distributions within 25 pc of our 30 L/T transition discoveries and all known L/T transition dwarfs. Note that some previously published L/T transition dwarfs have spectral types based on optical spectra, while others have near-IR spectral types. For a fair comparison with our near-IR discoveries, we can only use near-IR spectral types for known objects because optical and near-IR types may not be the same for a given object (e.g., Kirkpatrick et al. 2010), and the optical spectral standards for L dwarfs do not include type L9 (Kirkpatrick et al. 1999). To obtain as complete a sample as possible of near-IR spectral types for known L/T transition dwarfs, we searched the literature and identified eight brown dwarfs within 25 pc with optical spectral types $\geq L4$ but no near-IR spectral types. Two of these have spectra in the SpeX Prism Library² which we used to determine near-IR spectral types (Table 7) following the visual method described in Section 3.2. Two more have optical spectral types L6 and L7, respectively, and we adopt these as the near-IR types for use in Figure 4. The remaining four all have optical spectral types of L5, so we do not include them in the known L/T transition sample. Figure 4 shows that our contribution is most significant for spectral types L9–T1.5, a range of particular interest for studies focused on photometric variability induced by clouds clearing in photospheres (Radigan et al. 2014). Our 19 L9–T1.5 discoveries have increased the 25 pc census by over 50%.

We note also that the $W1$ vs. $W1 - W2$ inequality we identified in Section 2.3 (Figure 1) preserves all of our L/T transition discoveries within 25 pc while excluding two-thirds of those farther away, and also excludes almost all of our discoveries having earlier spectral types (which all lie beyond 25 pc).

Eleven of our discoveries have spectral features we deemed unusual enough to assign the object’s spectral type a “peculiar” designation. All of these objects were identified as candidate unresolved binaries, and we discuss them in Section 4.5.

4.2. Spectral Indices and Spectral Types

In Section 3.2, we described three methods we used to determine spectral types for our discoveries: visual comparison with field standards, and two index-based methods which applied to limited spectral type ranges. Because visual typing was the only method used for all objects, we adopted those types as the final spectral types for our discoveries. Here we describe the results of the index-based methods and compare our visual and index-based spectral types.

²<http://pono.ucsd.edu/~adam/browndwarfs/spexprism>

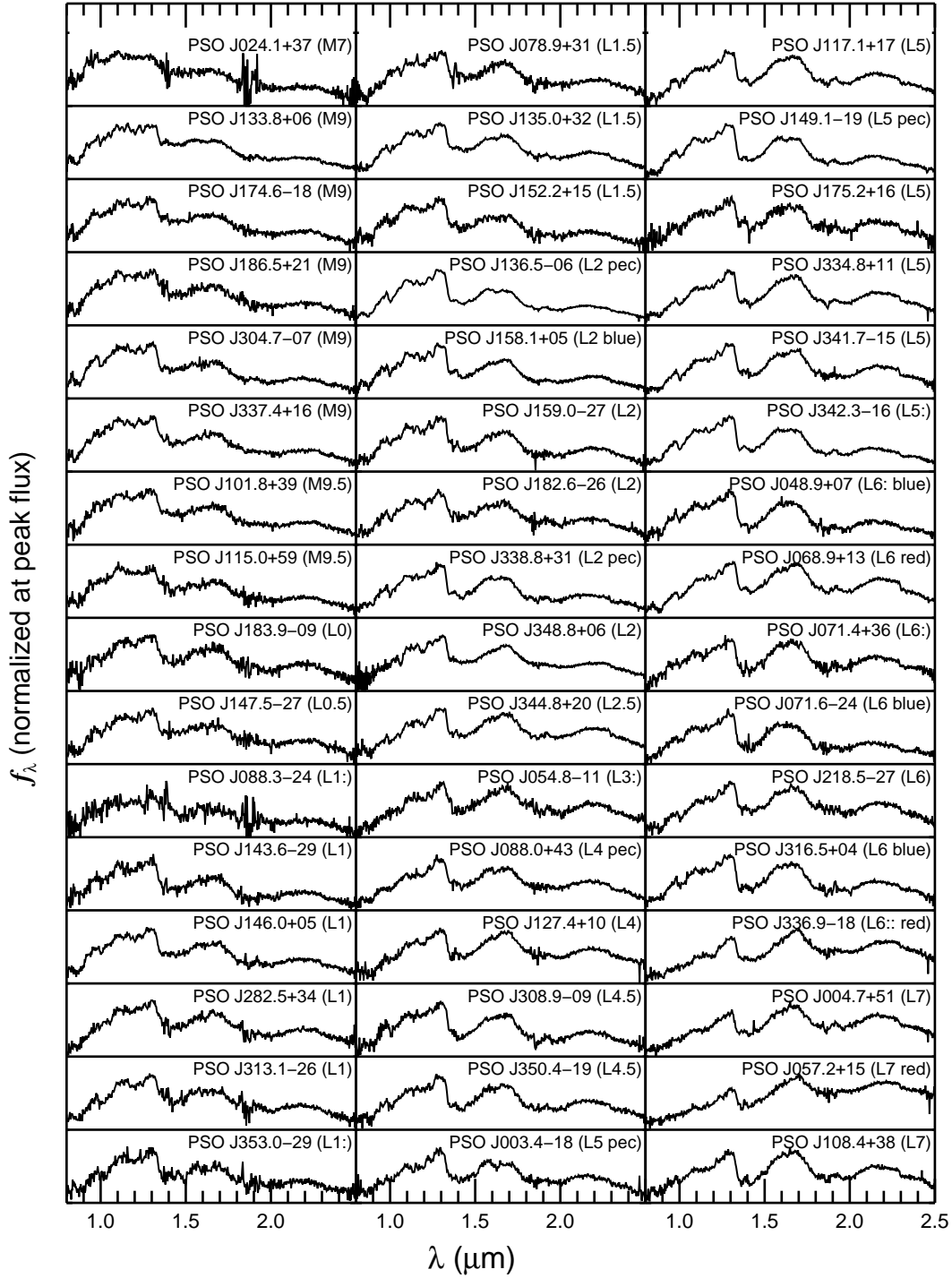


Fig. 2.— SpeX prism spectra for our discoveries, normalized at the peak flux value for each spectrum and arranged from earliest to latest spectral type. Spectra were typed by visual comparison with the near-infrared standards defined by Burgasser et al. (2006) and Kirkpatrick et al. (2010).

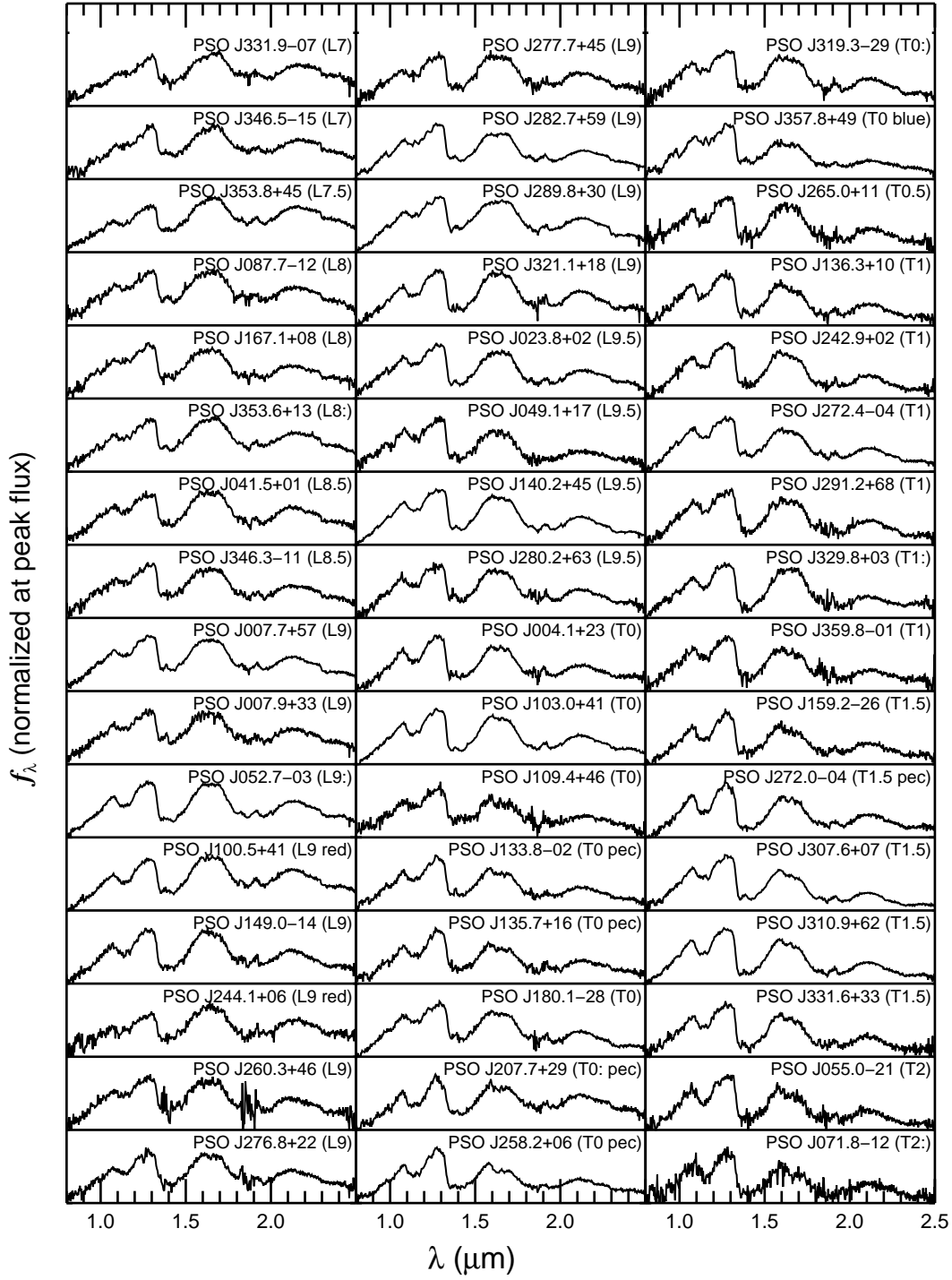


Fig. 2.— continued.

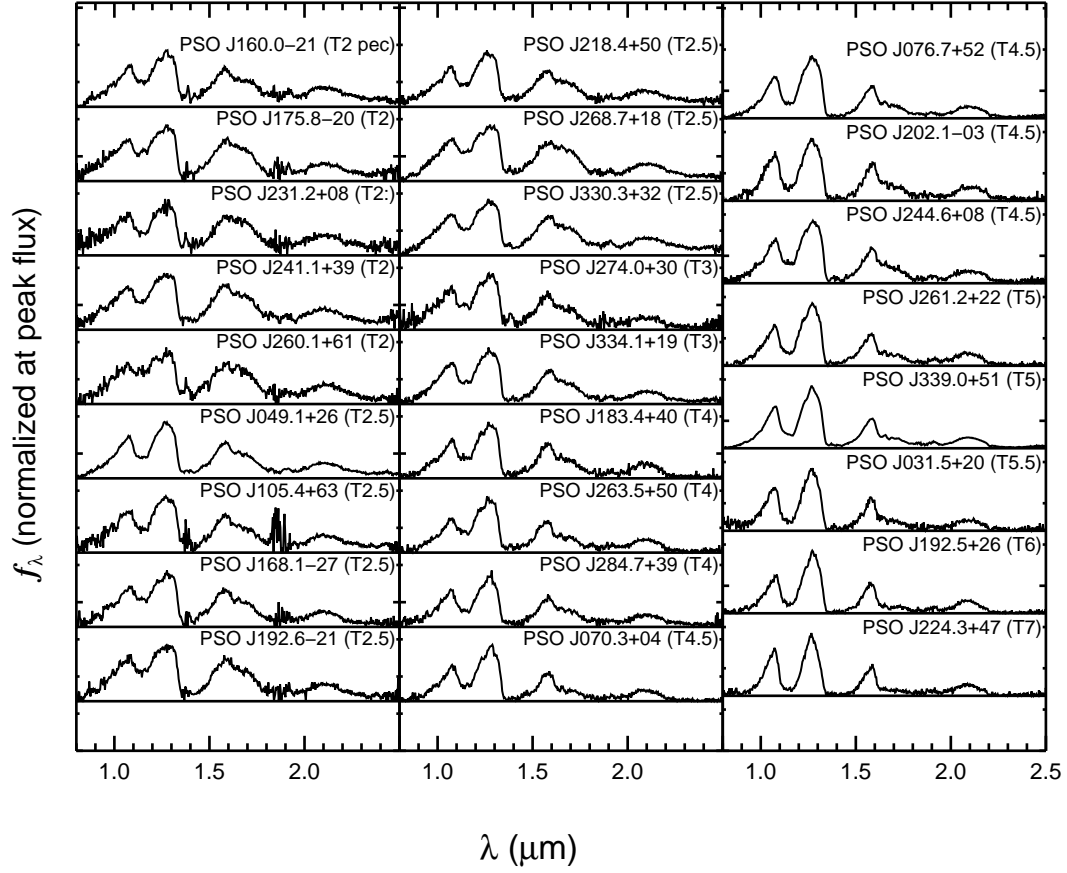


Fig. 2.— continued.

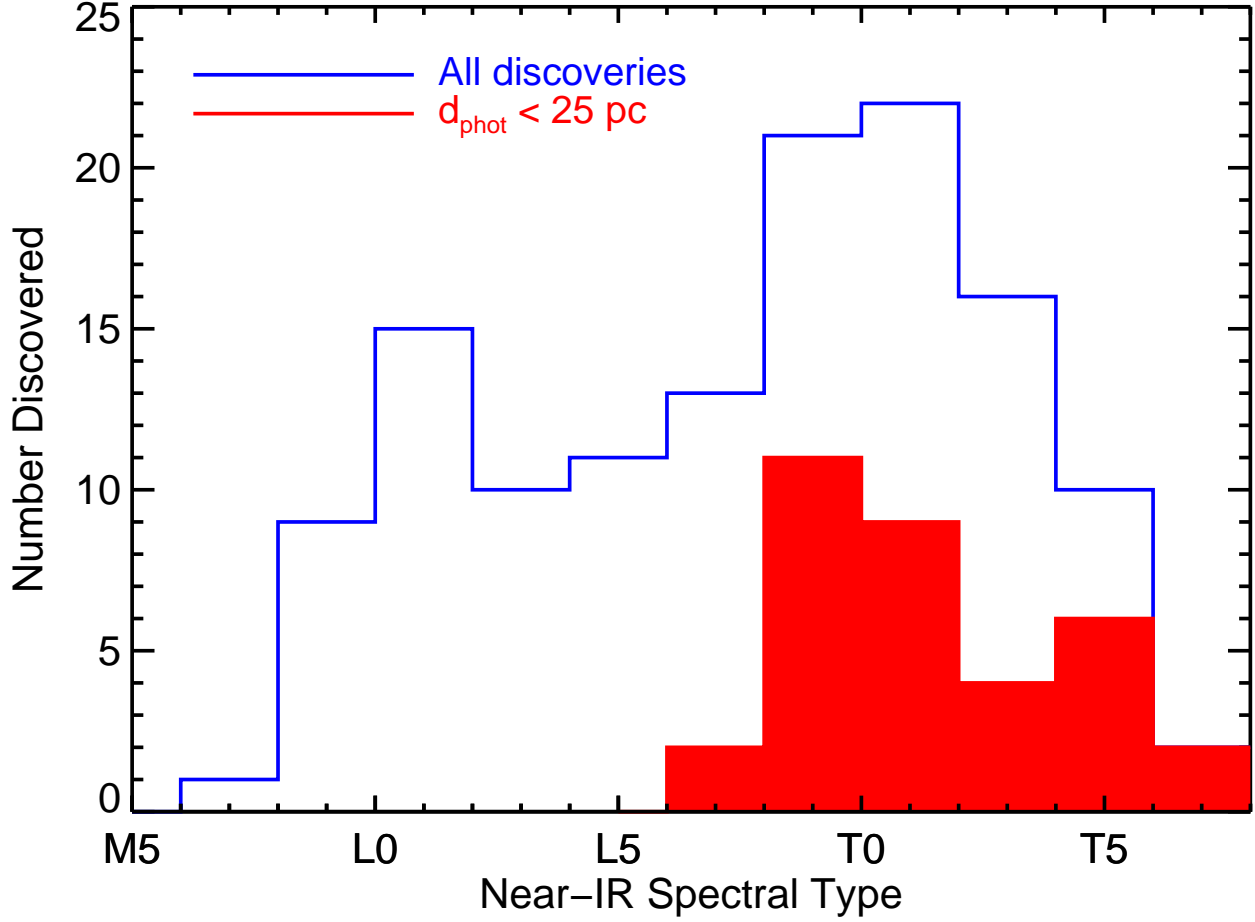


Fig. 3.— The spectral type distribution of our ultracool discoveries (blue open histogram), highlighting objects with W2 spectrophotometric distances less than 25 pc (solid red). We identified 79 objects with spectral types L6–T4.5, including 30 within 25 pc.

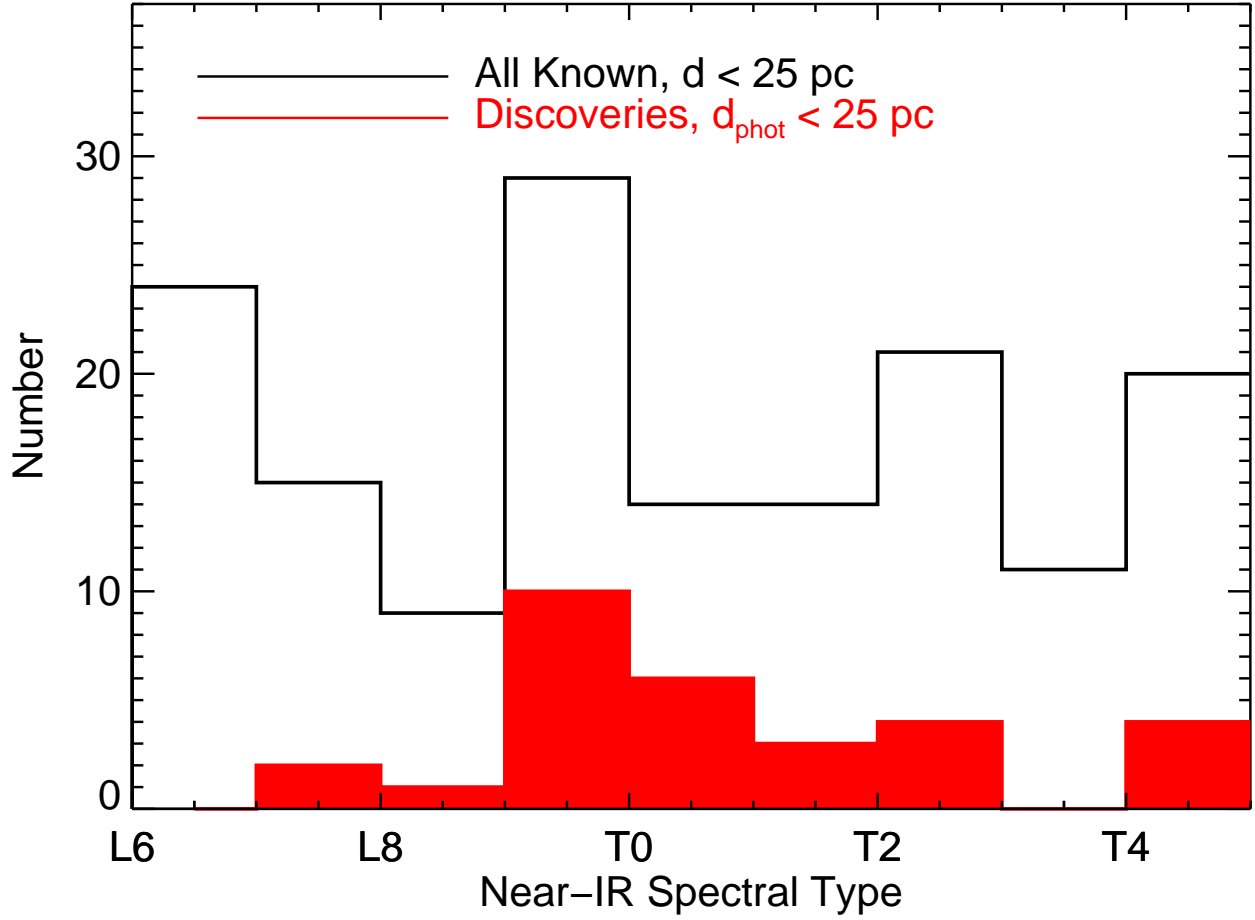


Fig. 4.— The near-infrared spectral type distribution of all known L/T transition dwarfs within 25 pc including our discoveries and previously published objects (black open histogram), compared with just our discoveries within 25 pc (solid red). In the middle of the L/T transition (L9–T1.5), our discoveries increase the census by over 50%.

4.2.1. *Allers & Liu (2013) Indices*

Spectral types determined using the AL13 indices are presented in Table 8, along with our visual spectral types for these objects. Figure 5 compares our visual and index-derived spectral types. The final index spectral types are mostly consistent with our adopted visual spectral types, agreeing within the joint 1σ uncertainties in 49 out of 60 cases. Of the remaining 11 objects, only one (PSO J057.2+15, discussed below) has an index-derived spectral type more than 2σ different from the visual type, and none are candidate binaries (Section 4.5). Figure 5 shows an apparent tendency for visual spectral types to be slightly later ($\approx 0.5 - 1$ subtypes) than the AL13-based types, but the bias is within the uncertainties of both typing methods, and does not appear correlated with low-gravity objects or with possible binaries. Overall, our results generally support the effectiveness and insensitivity to gravity of the AL13 low-resolution spectral type indices.

We now discuss the objects whose index-derived spectral types are different from our adopted visual types by more than 1σ . The overall tendency here is for the AL13 index-based spectral types to be earlier than our visual types for unusually red objects.

PSO J004.7+51 (visual L7, index $L5.4 \pm 0.8$) — The index-based spectral type is determined by only one index (H_2OD) and is too late-type for the other indices to apply. The spectrum is redder overall than the L7 standard, and this has probably affected the H_2OD index which measures the depth of the $\approx 1.9 \mu m$ water absorption band.

PSO J057.2+15 (visual L7 red, index $L2.0 \pm 0.9$) — This late-L dwarf is very red. As with PSO J004.7+51, the index-based spectral type is determined by only the H_2OD index, and is 3.6σ different (joint uncertainties) from the visual L7 type. The $\approx 1.9 \mu m$ water absorption band measured by the H_2OD index is significantly shallower than for the L7 standard.

PSO J068.9+13 (Hya12) (visual L6 red, index $L4.6 \pm 0.8$) — Another unusually red object, cool enough that only the H_2OD index is available to determine the spectral type. Visually, the J band is an excellent match to the L6 standard. The object was first identified photometrically by Hogan et al. (2008) and confirmed by Lodieu et al. (2014) as an L3.5 dwarf based on its optical spectrum. Lodieu et al. (2014) classify Hya12 as a candidate member of the Hyades based on its sky location, proper motion, and photometric distance. We tentatively assign this object a gravity classification of INT-G (Section 4.4), which would imply a younger age than the Hyades. A higher-S/N spectrum would confirm the youth of PSO J068.9+13, and parallax and radial velocity measurements are needed to assess its membership in the Hyades.

PSO J127.4+10 (visual L4, index $L2.5 \pm 0.8$) — Also a redder object, with three indices contributing to the final index type, but with a good visual J band match to the L4 standard. We tentatively give this object a gravity classification of VL-G (Section 4.4), noting the triangular H band profile, but the lower S/N of the spectrum precludes a firm gravity determination.

PSO J143.6–29 (visual L1, index $L3.1^{+1.2}_{-1.3}$) — The S/N of this spectrum limits our ability to declare a firm spectral type and increases the uncertainties in the index-based type, but the J band

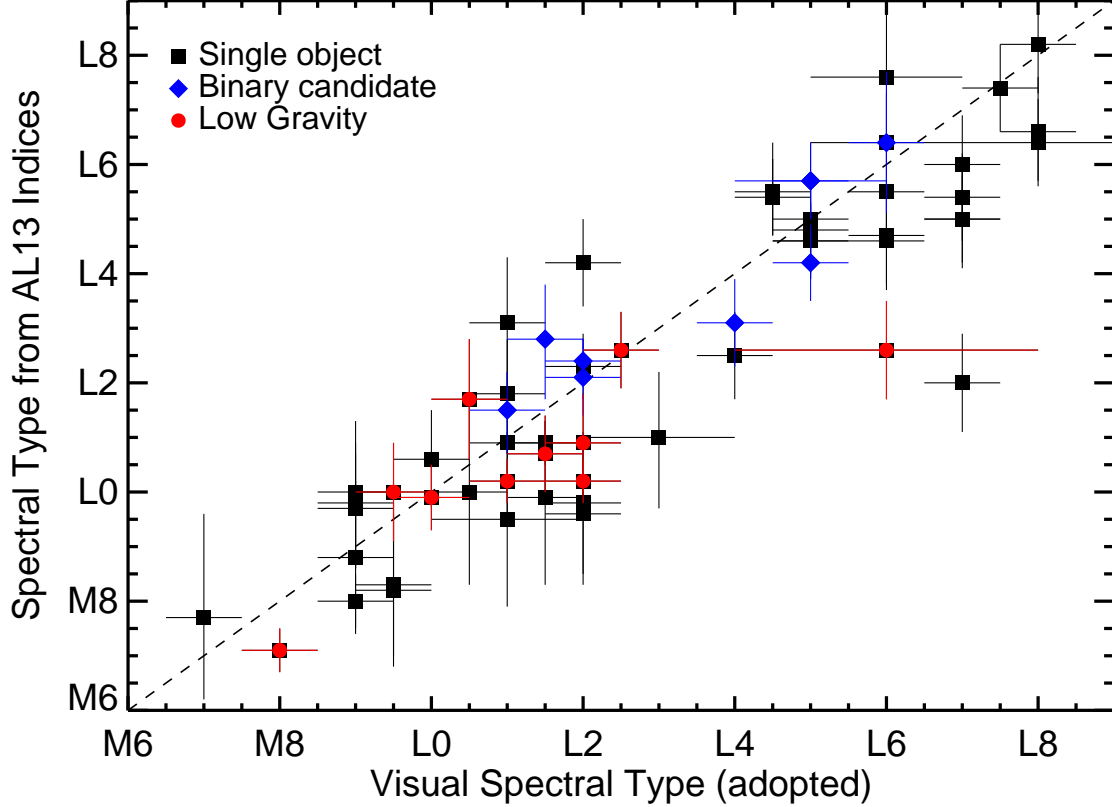


Fig. 5.— Comparison of our visual spectral types with spectral types calculated using the indices of Allers & Liu (2013a). Single objects are marked with black squares, binary candidates (Section 4.5) with blue diamonds, and objects having INT-G or VL-G gravity classifications (Section 4.4) with red circles. The dashed black line indicates equal spectral types. There is an overall tendency for our visual spectral types to be ≈ 1 sub-type later than the index-based types, but no other trend is apparent in the typing of binary candidates or low-gravity objects.

matches the L1 standard quite well. This object is also discussed in Section 4.2.2.

PSO J159.0–27 (visual L2 blue, index $L4.2 \pm 0.8$) — The object is atypically blue for an L2, which may increase the depth of the water absorption bands used by the indices to determine the spectral type. Visually it is a good match in J band to the L2 standard and shows signs of low gravity. We tentatively assign this object a gravity classification of INT-G (Section 4.4).

PSO J218.5–27 (visual L6, index $L3.9 \pm 0.8$) — The modest S/N of this spectrum affects the indices (and results in the noise spikes in the H band peak). The J band spectrum is a good match to the L6 standard.

PSO J331.9–07 (visual L7, index $L5.0 \pm 0.8$) — This object is an excellent visual match to the L7 standard, and the index-based spectral type is determined by only one index (H_2O).

PSO J336.9–18 (visual L6:: red, index $L2.1 \pm 0.7$) — This extremely red L dwarf has a VL-G gravity class (Section 4.4). Visually, it is not a clear J band match to any field standard, but the shape of the J band peak and the depth of the $\approx 1.4 \mu\text{m}$ water absorption band are decent matches to the L6 standard. The index-based type depends on two indices. This object demonstrates the difficulty in assigning spectral types to unusually red L dwarfs.

PSO J346.5–15 (visual L7, index $L5.0 \pm 0.9$) — This object is a good visual match to the L7 standard, albeit slightly blue, and the index-based spectral type is determined by only one index (H_2O) in the fairly noisy spectrum.

PSO J348.8+06 (visual L2, index $L0.2 \pm 0.4$) — We classify this object as VL-G (Section 4.4), as it shows many signs of low gravity in its spectra. The J band spectrum is a good match to the L2 standard.

4.2.2. Burgasser et al. (2006) Indices

We show spectral types calculated using the B06 indices for all of our L and T dwarf discoveries in Table 9, along with the adopted visual spectral types. Figure 6 compares our visual and B06 index-based spectral types. The spectral types from the two methods agree very well for T dwarfs (none differ by more than 1σ). 17 of the 70 L dwarfs have $>1\sigma$ differences in spectral type, even though the uncertainties on the L dwarf spectral types are larger. This larger scatter in L dwarf types is consistent with the smaller number of indices used as well as the wider variety of spectral features and colors seen in L dwarfs than in T dwarfs (e.g., Kirkpatrick et al. 2010), and was previously noted by Burgasser et al. (2010) who compared literature and B06 spectral types. The visual types appear to skew ≈ 1 sub-type earlier than the B06 types for early-L dwarfs and ≈ 1 sub-type later for late-L dwarfs. We see no significant correlation between low gravity and the differences in visual and B06 spectral types. The uncertainties in the index-based types are typically larger than the rms uncertainties of the Burgasser (2007) polynomials but do not appear to be correlated with the S/N of our spectra. Overall, our results strongly support the effectiveness of the B06 indices for T

dwarf classification, but B06 index-based spectral types for L dwarfs may differ visually determined ones by $\approx 0.5 - 1.0$ subtypes.

Below we comment on objects whose B06 index-derived spectral types differ from our adopted visual types by more than 1σ .

PSO J003.4–18 (2MASS J0013–1816) (visual L5 pec, index $L8.0 \pm 2.3$) — We identify this object as a strong binary candidate in Section 4.5.1. Our visual L5 type was determined by the J band shape, but H and K bands have features typical of cooler dwarfs.

PSO J007.9+33 (visual L9, index $L7.6 \pm 0.4$) — We find a good fit to this object’s J band profile with the L9 standard, but PSO J007.9+33 has slightly shallower water absorption bands at $\approx 1.15 \mu\text{m}$ and $\approx 1.4 \mu\text{m}$ which are suggestive of an earlier spectral type.

PSO J087.7–12 (visual L8, index $L6.0 \pm 1.1$) — Low S/N likely affects the indices for this spectrum, which is a good visual fit to the L8 standard.

PSO J088.3–24 (visual L1:, index $L6.8 \pm 4.1$) — This spectrum has only $S/N \approx 10$. The overall early-L morphology is apparent, but more accurate typing by any method will require a higher S/N spectrum.

PSO J136.5–06 (visual L2 pec, index $L6.6 \pm 3.1$) — This strong binary candidate (Section 4.5.1) shows multiple signs of an L+T blend, and consequently the individual indices gives spectral types ranging from L4.2 to T1.2.

PSO J143.6–29 (visual L1, index $L3.0 \pm 0.6$) — This is the only object among our discoveries whose visual spectral type disagrees by more than 1σ with spectral types derived from both the AL13 (Section 4.2.1) and B10 indices. The index-based classifications are L3.1 and L3.0, in close agreement, but this spectrum is noisy enough to make those types unreliable. We see a good J band match to the L1 standard.

PSO J149.0–14 (visual L9, index $T0.5 \pm 0.5$) — This medium-ranked binary candidate (Section 4.5.2) shows an overall L9 morphology, but there are subtle signs of methane absorption that shift the index-based type to a T dwarf.

PSO J149.1–19 (visual L5, index $L7.0 \pm 0.6$) — One of our strongest binary candidates (Section 4.5.1), this object’s spectrum shows several L+T dwarf blend features along with a good J band fit to the L5 standard.

PSO J158.1+05 (visual L2 blue, index $L3.5 \pm 0.3$) — The J-band spectrum is a good fit to the L2 standard, but the overall bluer spectral slope includes deeper water bands that point to a later index-based spectral type.

PSO J183.9–09 (visual L0, index $L1.0 \pm 0.4$) — The spectral types differ by only 1.1σ , which is actually surprising given the very low S/N of this early-L spectrum.

PSO J244.1+06 (visual L9 red, index $L7.8 \pm 0.5$) — The spectral types differ by only 1.2σ . This

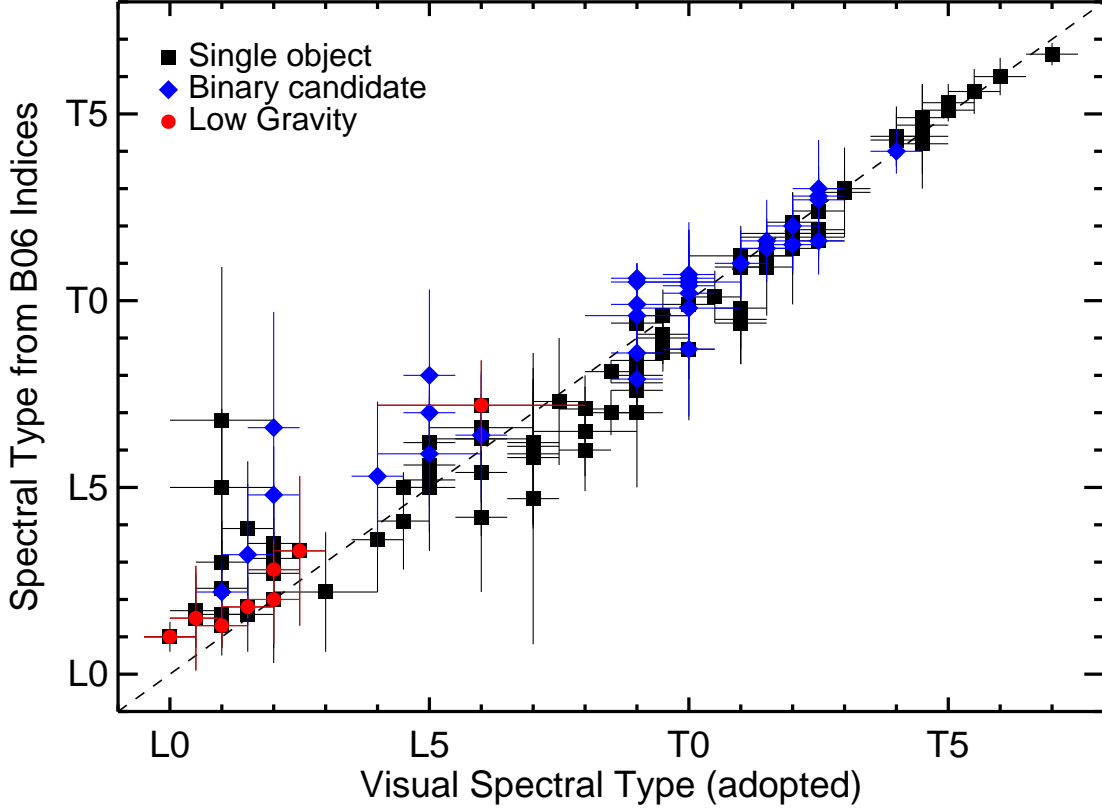


Fig. 6.— Comparison of our visual spectral types with spectral types calculated using the indices of Burgasser et al. (2006), using the same symbols as Figure 5. Compared to the index-based spectral types, our visual spectral types are ≈ 1 sub-type earlier for early-L dwarfs, ≈ 1 sub-type later for late-L dwarfs, and in good agreement for T dwarfs. No other trend is apparent in the typing of low-gravity objects, but the objects with the largest discrepancy in types tend to be binary candidates. The two objects with visual L1 types and index-based types $\geq L5$ have spectra with $S/N < 20$, so their index-based types are not reliable.

minor discrepancy may be due to the modest S/N of the spectrum and/or the object’s unusually red color.

PSO J282.7+59 (WISE J1851+5935) (visual L9, index $L7.9 \pm 0.4$) — This weak binary candidate (Section 4.5.3) was discussed in detail in Paper I, and was assigned a spectral type of L9 pec by Thompson et al. (2013). The object’s blue color may contribute to the slightly earlier index-based spectral type.

PSO J321.1+18 (visual L9, index $T0.6 \pm 0.4$) — This weak binary candidate (Section 4.5.3) features water absorption bands and an H band peak more similar to an early-T dwarf, which explains the T0.6 index-based type.

PSO J338.8+31 (visual L2 pec, index $L4.8 \pm 1.3$) — The deeper water absorption bands of this strong binary candidate (Section 4.5.1) lead to a later index-based spectral type.

PSO J346.3–11 (visual L8.5, index $L7.0 \pm 0.6$) — The J band shape is a clear fit to the L8 and L9 standards. Surprisingly, this object was assigned an earlier spectral type by the indices despite the depth of the water absorption bands and the slightly bluer color.

PSO J353.0–29 (visual L1:, index $L5.0 \pm 2.1$) — This spectrum has only $S/N \approx 15$. The overall early-L morphology is apparent, but more accurate typing by any method will require a higher S/N spectrum.

4.3. Colors and PS1 Photometry

Figures 7–11 show the colors of our discoveries and previously known ultracool dwarfs that we used to identify the candidate L/T transition dwarfs in our search (Section 2). Those color criteria were designed using PS1 photometry from January 2012 (Processing Version 1). Since then, ongoing PS1 observations and image processing have produced more detections and improved measurements. We have chosen to use PS1 data from March 2015 (Processing Version 2) to make Figures 7–11 because of the improved photometric precision and the increased number of detections, particularly valuable in i_{P1} . WISE photometry is from the All-sky release (Cutri et al. 2012).

These figures demonstrate the success of our color criteria. In particular, Figure 7 shows the two colors at the core of our screening process, $y_{P1}-W1$ and $W1-W2$. Our $y_{P1}-W1 \geq 3.0$ mag cut is very effective, removing only a few T dwarfs at the cool end of the L/T transition (spectral type $\approx T4-T5$). Our $W1-W2 \geq 0.4$ mag cut is similarly effective, excluding some L6–L7 dwarfs but also culling many more earlier-type objects. We also note that four of our discoveries now have $y_{P1}-W1 < 3.0$ mag with the updated PS1 photometry; these objects have spectral types M7, T4, T4.5, and T5.5.

The updated PS1 photometry includes i_{P1} detections of 50 of our spectroscopic targets (compared with only 3 detections from the January 2012 PS1 photometry), nearly all of which have

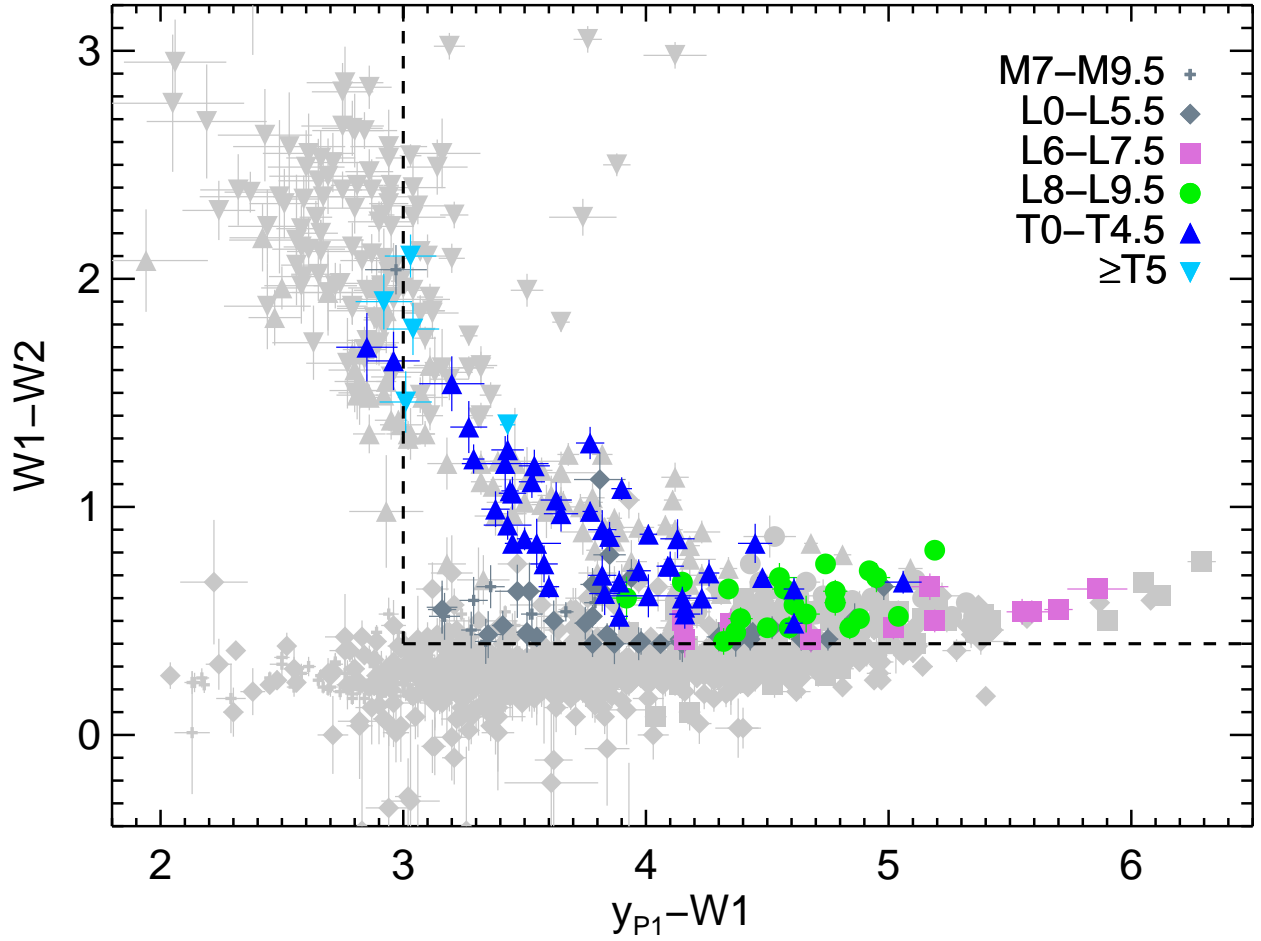


Fig. 7.— $W1-W2$ vs. $y_{P1}-W1$ diagram showing our discoveries in dark gray and colors for spectral type bins (see legend at upper right), and previously known ultracool dwarfs in light gray using the same symbols as for our discoveries. We selected objects above and to the right of the dashed lines using y_{P1} photometry from 2012 January; this plot shows y_{P1} values as of 2015 March. Only 4 of our 130 discoveries would have been excluded from our search using the newer y_{P1} photometry.

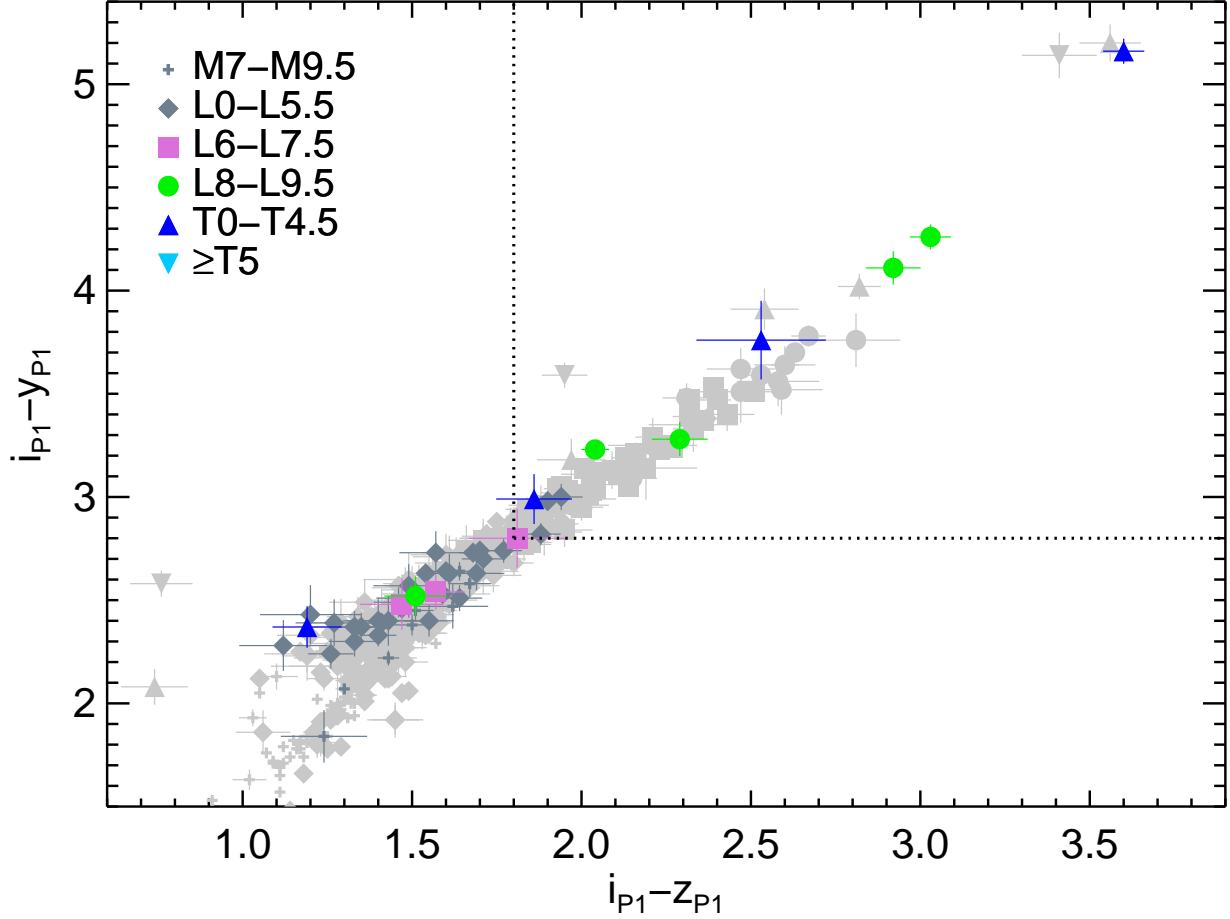


Fig. 8.— $i_{P1}-y_{P1}$ vs. $i_{P1}-z_{P1}$ diagram for our discoveries and known ultracool dwarfs, using PS1 photometry from 2015 March and the same symbols as in Figure 7. The dotted black lines indicate the color cuts used in our search; we selected objects above and to the right of the dotted lines, but only enforced each cut for objects having $\sigma < 0.2$ mag and at least two detections in both i_{P1} and z_{P1} in the 2012 January epoch of PS1 photometry. Most of our discoveries with spectral types less than L6 would have been culled from our search using the most recent PS1 photometry, which has many more detections in i_{P1} for our objects. This would have resulted in a significantly higher fraction ($\approx 80\%$) of L/T transition discoveries, but far fewer discoveries of young objects.

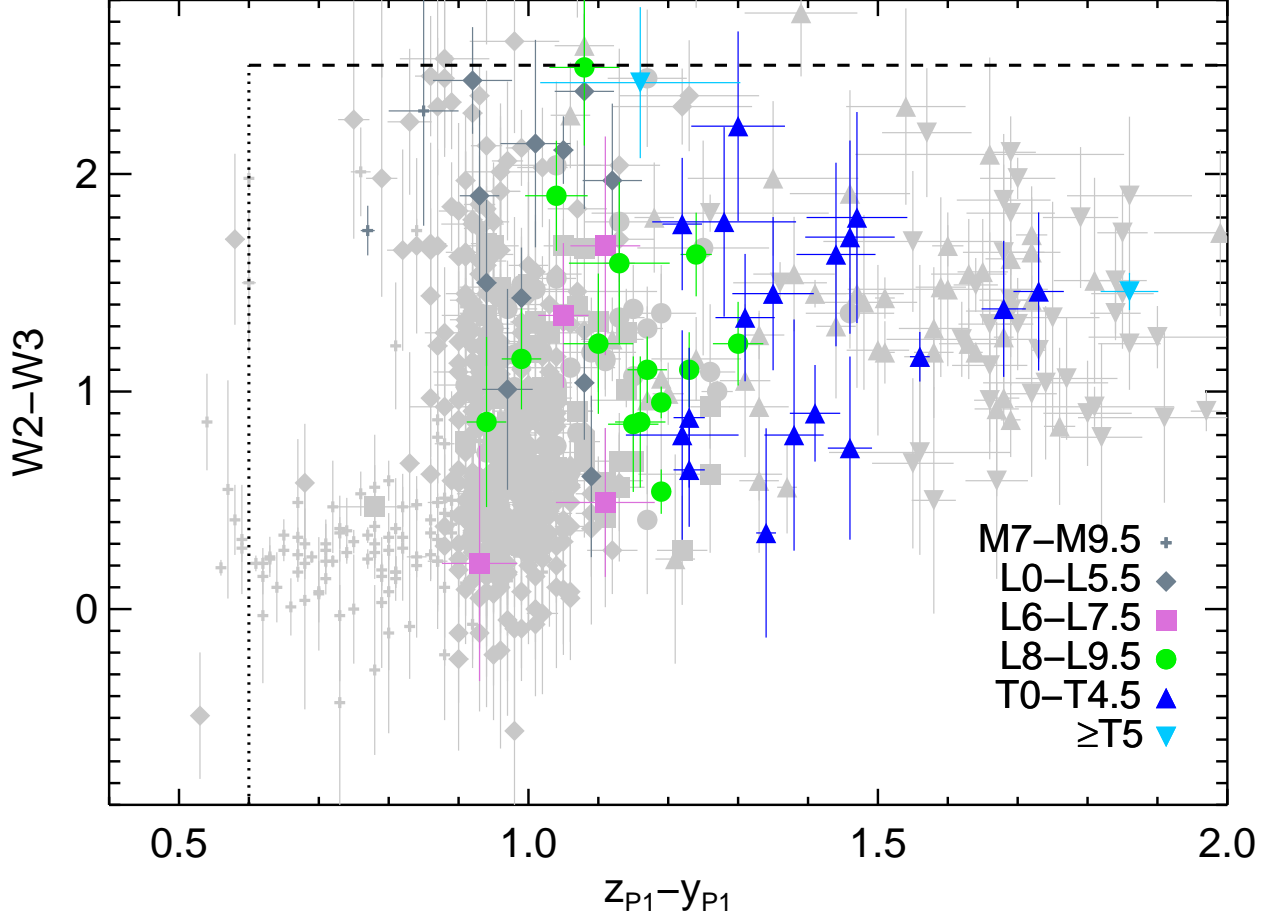


Fig. 9.— $W2 - W3$ vs. $z_{P1} - y_{P1}$ diagram for our discoveries and known ultracool dwarfs, using PS1 photometry from 2015 March and the same symbols as in Figure 7. The vertical dotted line indicates our $z_{P1} - y_{P1}$ cut, which we applied only to objects with $\sigma_z < 0.2$ mag and having at least two z_{P1} detections in the 2012 January epoch of PS1 photometry. The horizontal dashed line represents our $W2 - W3$ cut, which we applied to all objects in our search in order to exclude galaxies. We selected objects below and to the right of these lines.

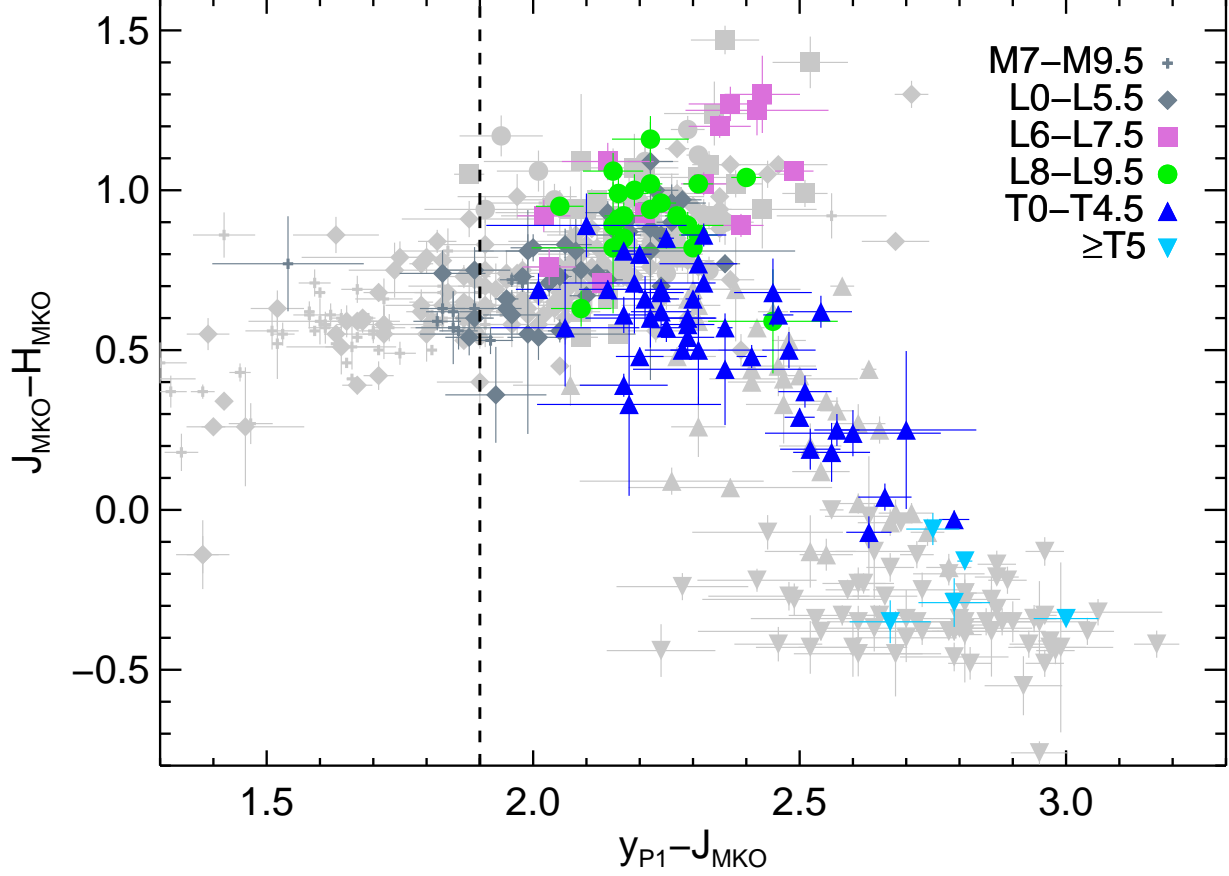


Fig. 10.— $J_{\text{MKO}} - H_{\text{MKO}}$ vs. $y_{\text{P1}} - J_{\text{MKO}}$ diagram for our discoveries and known ultracool dwarfs, using y_{P1} photometry from 2015 March and the same symbols as in Figure 7. We selected objects to the right of the dashed line using y_{P1} photometry from 2012 January. (We did not use $J - H$ color to screen targets in our search, but it has been used in many previous near-IR searches for T dwarfs.) The updated PS1 photometry has shifted eleven late-M and early-L dwarfs outside of our $y_{\text{P1}} - J_{\text{MKO}} \geq 1.9$ mag cut.

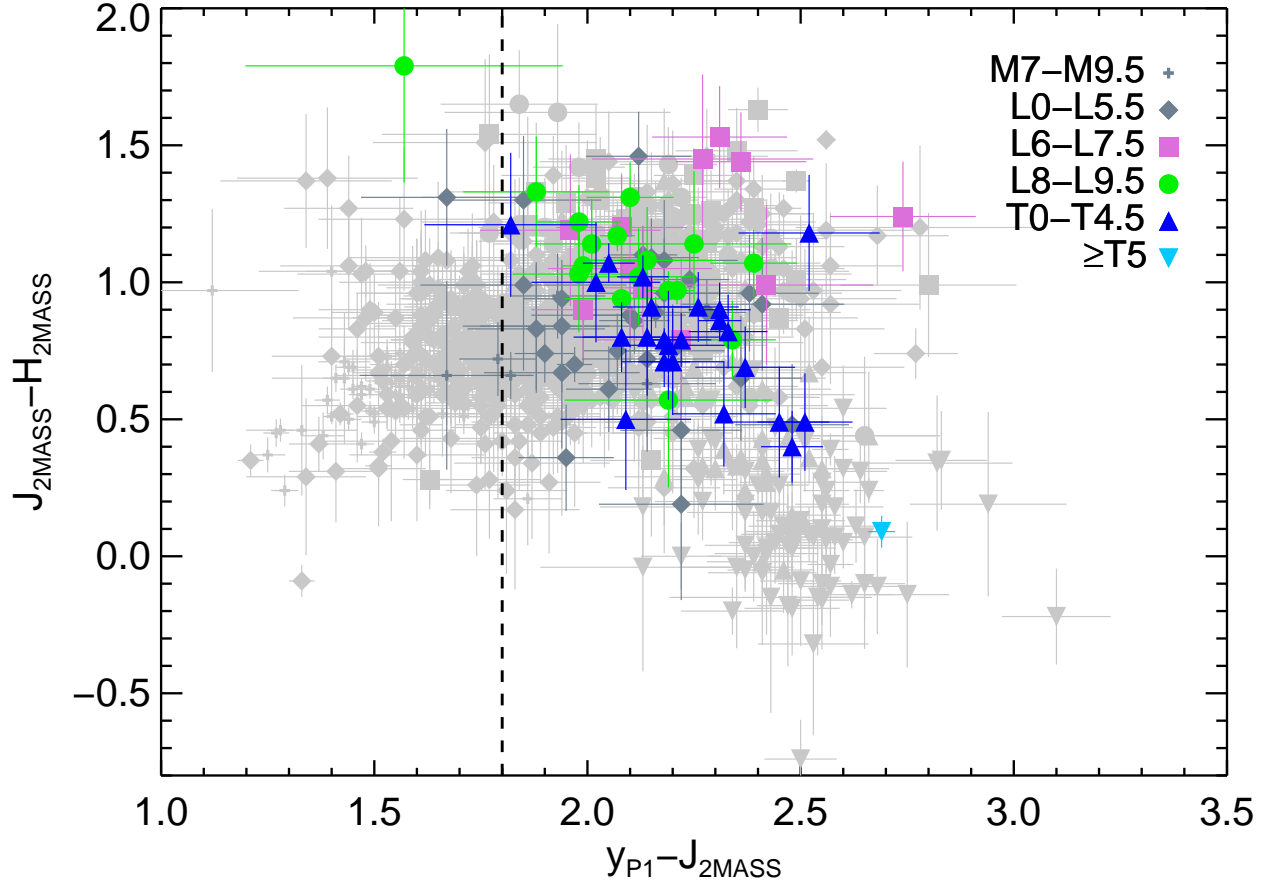


Fig. 11.— Same as Figure 10, but using 2MASS photometry for J and H bands instead of MKO. The updated PS1 photometry has revised the unusually blue $y_{P1} - J_{2MASS}$ colors of discoveries we presented in Paper I, bringing them in line with other field objects.

spectral types earlier than L6. The new $i_{P1}-y_{P1}$ and $i_{P1}-z_{P1}$ colors (Figure 8) would actually have culled most of these $\text{SpT} < \text{L6}$ objects from our candidate list, significantly increasing the efficiency of our search for L/T transition dwarfs (from 55% to $\approx 80\%$) but also eliminating most of our young discoveries (Section 4.4). i_{P1} detections of T dwarfs remain rare (≈ 10 in Processing Version 2), as these objects are optically extremely faint. Figure 9 shows the usefulness of $z_{P1}-y_{P1}$ for separating M dwarfs from L and T dwarfs, and similarly for $y_{P1} - J_{\text{MKO}}$ in Figure 10. The new y_{P1} photometry would also have rejected 11 of our late-M and early-L dwarf discoveries which now have $y_{P1} - J_{\text{MKO}} < 1.9$.

In Paper I, we reported unusually blue $y_{P1} - J_{2\text{MASS}}$ colors for six of our bright nearby discoveries. We note that this color deviation has now disappeared. The updated y_{P1} photometry for these objects is slightly fainter, which brings the $y_{P1} - J_{2\text{MASS}}$ colors of these discoveries into the locus of other field objects (Figure 11).

4.4. Low-Gravity Objects

Signatures of low gravity in the spectra of ultracool dwarfs are a reflection of the extended radii of young objects that are still contracting. AL13 identified a set of near-IR spectral indices at low ($R \approx 100$) and intermediate ($R \approx 1000$) spectral resolution to assess the surface gravity of M4–L7 dwarfs, and thereby to identify ultracool dwarfs younger than ≈ 200 Myr. Briefly, the low-resolution indices measure the depths of the FeH_z ($0.99 \mu\text{m}$), VO_z ($1.06 \mu\text{m}$), and K I_J ($1.24 \mu\text{m}$) absorption features relative to the continuum, as well as the shape of the H band continuum over $1.47 - 1.67 \mu\text{m}$. Based on these indices, an object is assigned a score of 0, 1, or 2, which correspond to classes of field gravity (FLD-G, ages $\gtrsim 200$ Myr), intermediate gravity (INT-G, ages $\approx 50 - 200$ Myr), and very low gravity (VL-G, ages $\approx 10 - 30$ Myr), respectively. (Note that the age calibration of these gravity classes is only notional, and more work is needed in this area.) The median value of the index scores is the final gravity score for the object.

We calculated low-resolution indices and gravity scores for our M and L dwarfs (through L7) using the approach described in Aller et al. (2015), performing Monte Carlo simulations for each object to propagate the measurement errors of our reduced spectra into the index calculations. Most of our spectra have $R \approx 75$, so the indices were computed using only a few resolution elements. We found that spectra with a mean S/N $\lesssim 30$ measured over the interval $1.20 - 1.31 \mu\text{m}$ (encompassing the bulk of the J-band flux for L dwarfs) produced gravity scores with uncertainties too large to contain useful information, and we discarded the scores for those objects. We visually inspected the remaining (higher S/N) spectra to confirm the gravity class, and flagged those with low enough S/N that we could not confirm the gravity class by eye.

Altogether, we classify 10 objects having low gravity (9 as VL-G, 1 as INT-G) and 9 more as FLD-G. Figure 12 plots the gravity classes derived from the four spectral indices for these objects against their spectral types. Our final gravity classifications are listed in Table 10, excluding six

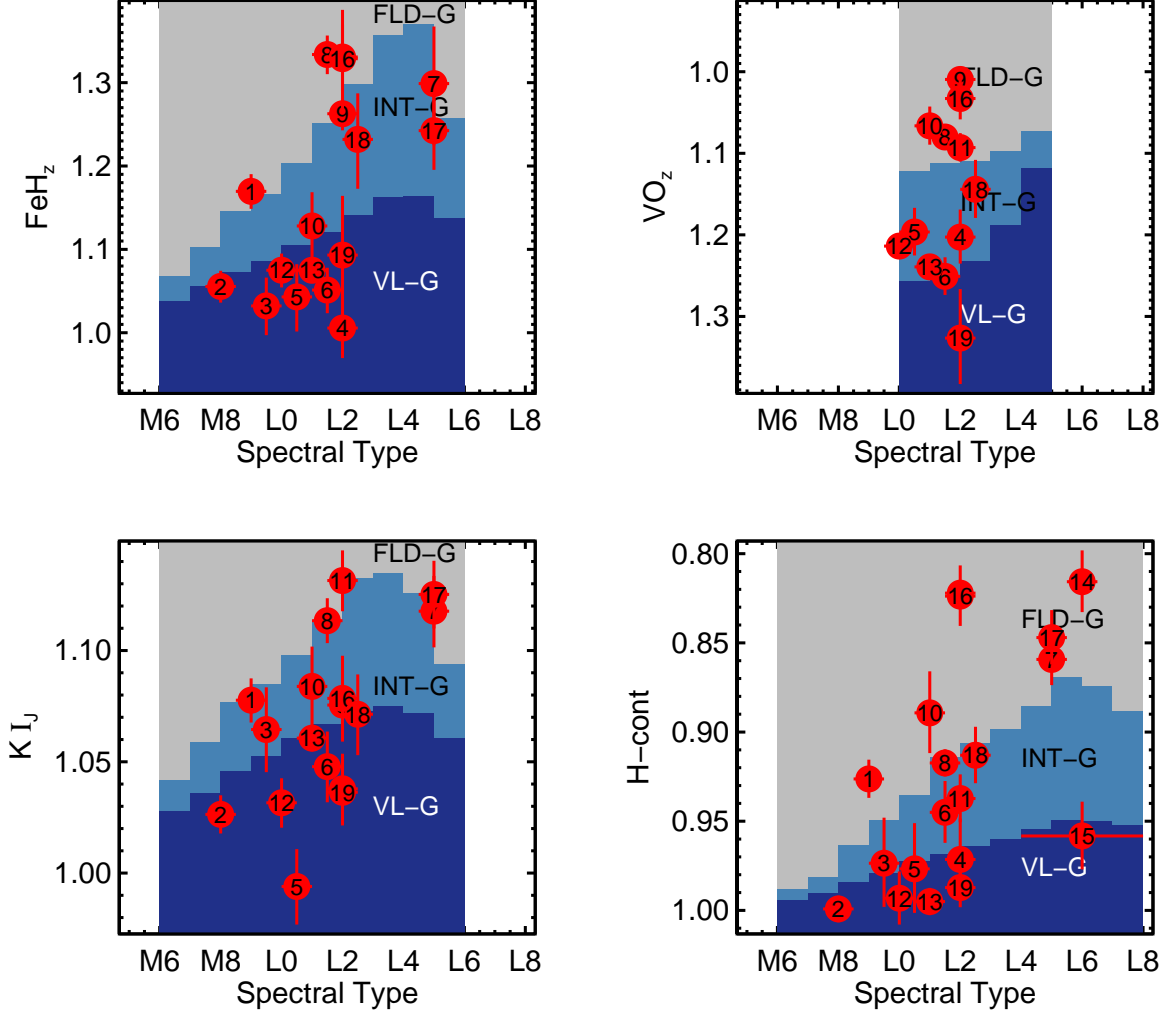


Fig. 12.— Values of the low-resolution gravity-sensitive spectral indices from Allers & Liu (2013a) for the objects whose gravity classes we confirm visually, including 9 FLD-G, 1 INT-G, and 9 VL-G objects. The index values are plotted in red, with values for the same object in different plots labelled with the same number. The gray, slate, and dark blue bars represent the ranges of index values corresponding to the FLD-G, INT-G, and VL-G gravity classes, respectively, and indicate the spectral types for which each index is valid for gravity classification. Given that our search targeted field L/T transition dwarfs and not young M and L dwarfs, discovering this many objects with low-gravity spectral signatures was unexpected.

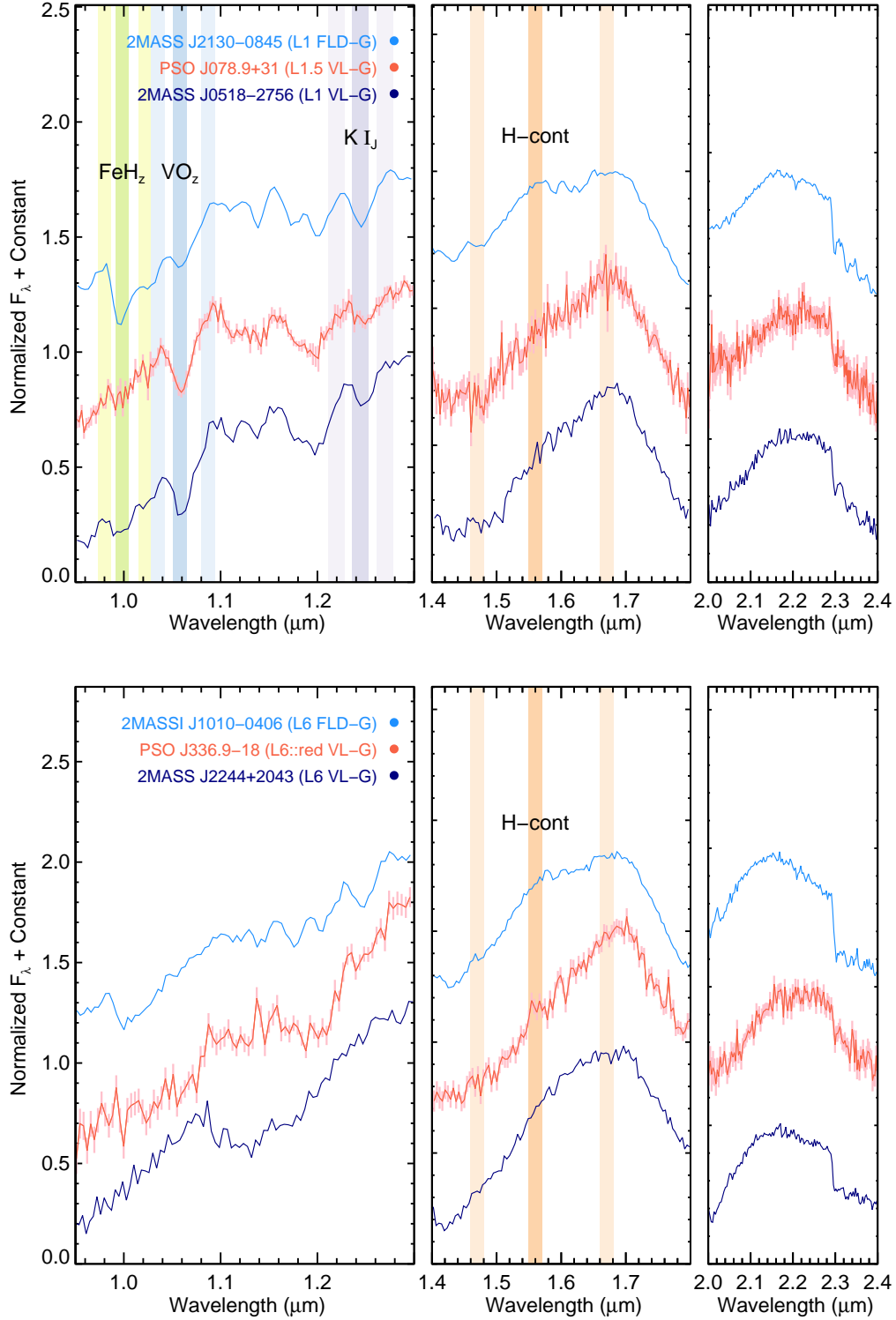


Fig. 13.— Plots showing our four newly identified field INT-G and VL-G objects (middle, with error bars) compared with field standards (top) from Kirkpatrick et al. (2010) and VL-G standards (bottom) from AL13 of the same spectral type (within 0.5 subtypes). The vertical colored bars show the spectral regions used to calculate the indicated indices, for visual comparison. Each plot shows only the indices that are valid for the object’s spectral type.

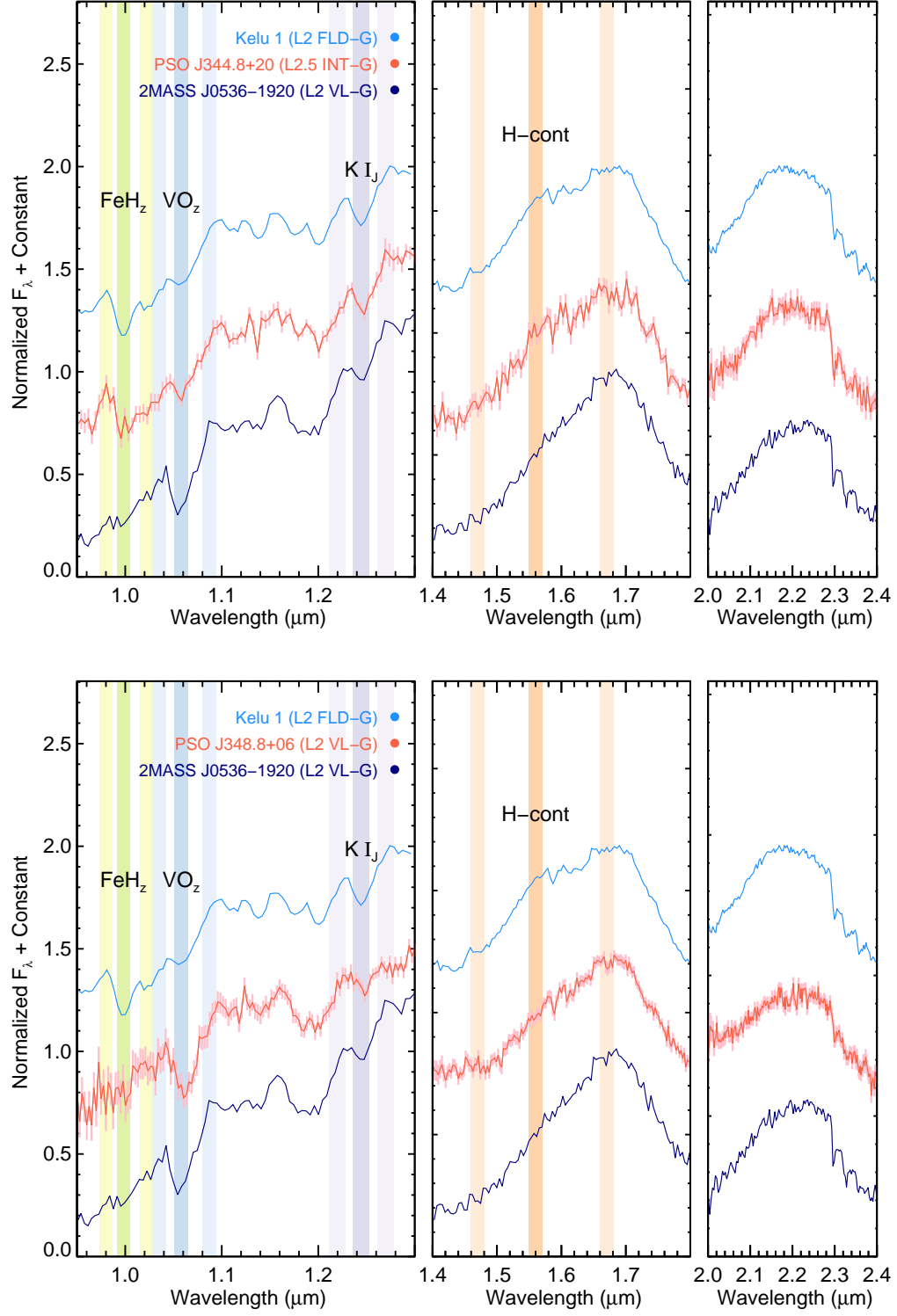


Fig. 13.— continued.

candidate members of the Scorpius-Centaurus Association and the Taurus star-forming region that will be presented in a future paper (Best et al., in prep). The remaining four, PSO J078.9+31 (L1.5 VL-G), PSO J336.9–18 (L6:: red VL-G), PSO J344.8+20 (L2.5 INT-G), and PSO J348.8+06 (L2 VL-G), appear to be young field objects, and their spectra are shown in Figure 13 along with field standards from Kirkpatrick et al. (2010) and VL-G standards from AL13 for comparison. Three of the objects (excluding PSO J336.9–18) show weak $0.99\ \mu\text{m}$ FeH_z and strong $1.06\ \mu\text{m}$ VO_z absorption features and a triangular H band shape, all signs of youth. PSO J336.9–18 is an L6 dwarf, too late-type for the FeH_z and VO_z features to yield reliable information about gravity (AL13), but featuring a triangular H-band shape and very red colors. While these are both recognized signatures of youth, AL13 caution that the triangular H-band shape can also appear in spectra of objects that have evidence of old age (based on kinematics). Therefore, while our classification of VL-G is formally correct for PSO J336.9–18, further evidence is needed to support the conclusion that the object is young.

We identify another 7 objects as potentially low-gravity based on their indices, but higher S/N spectra are needed to securely classify them. Among these is PSO J068.9+13 (L6 red, candidate INT-G), identified by Lodieu et al. (2014) as a candidate member of the Hyades (see discussion in Section 4.2.1). Figure 14 shows the gravity classes vs. spectral types for these 7 potentially low-gravity objects, and Figure 15 compares their spectra to the field and VL-G standards.

In Table 11, we list six more objects whose spectra show indications of youth, but for which the AL13 indices were not useful because of the spectral type of the object or the low S/N (< 30) of our spectrum. These indications include the redder-than-normal colors and triangular H-band shape described above. Three are candidate members of young moving groups (Section 6.2), and three are field objects.

4.5. Candidate Binaries

Roughly 15 – 30% of ultracool dwarfs are binaries (e.g., Basri & Reiners 2006; Liu et al. 2006; Burgasser 2007). Binary systems are important benchmarks, as the binary components are equidistant, coeval, and have common metallicities. If resolved with high-resolution imaging, these systems can be monitored to determine their orbits and dynamical masses (e.g., Liu et al. 2008; Konopacký et al. 2010; Dupuy et al. 2010), breaking the mass/age degeneracy and providing stringent tests for atmospheric and evolutionary models (e.g., Dupuy et al. 2014, 2015b).

We have examined our discoveries for unusual spectral features that suggest unresolved binarity, using the spectral index criteria of Bardalez Gagliuffi et al. (2014, hereinafter BG14) for our M7–L7.5 dwarfs and Burgasser et al. (2010, hereinafter B10) for our L8 and later dwarfs. We first ranked our discoveries by the number of index criteria satisfied, and then visually reviewed all spectra for peculiar features indicating blends (see descriptions of individual objects below). We rejected objects with J band ($1.20 - 1.31\ \mu\text{m}$) S/N < 25 , as several objects with S/N below this

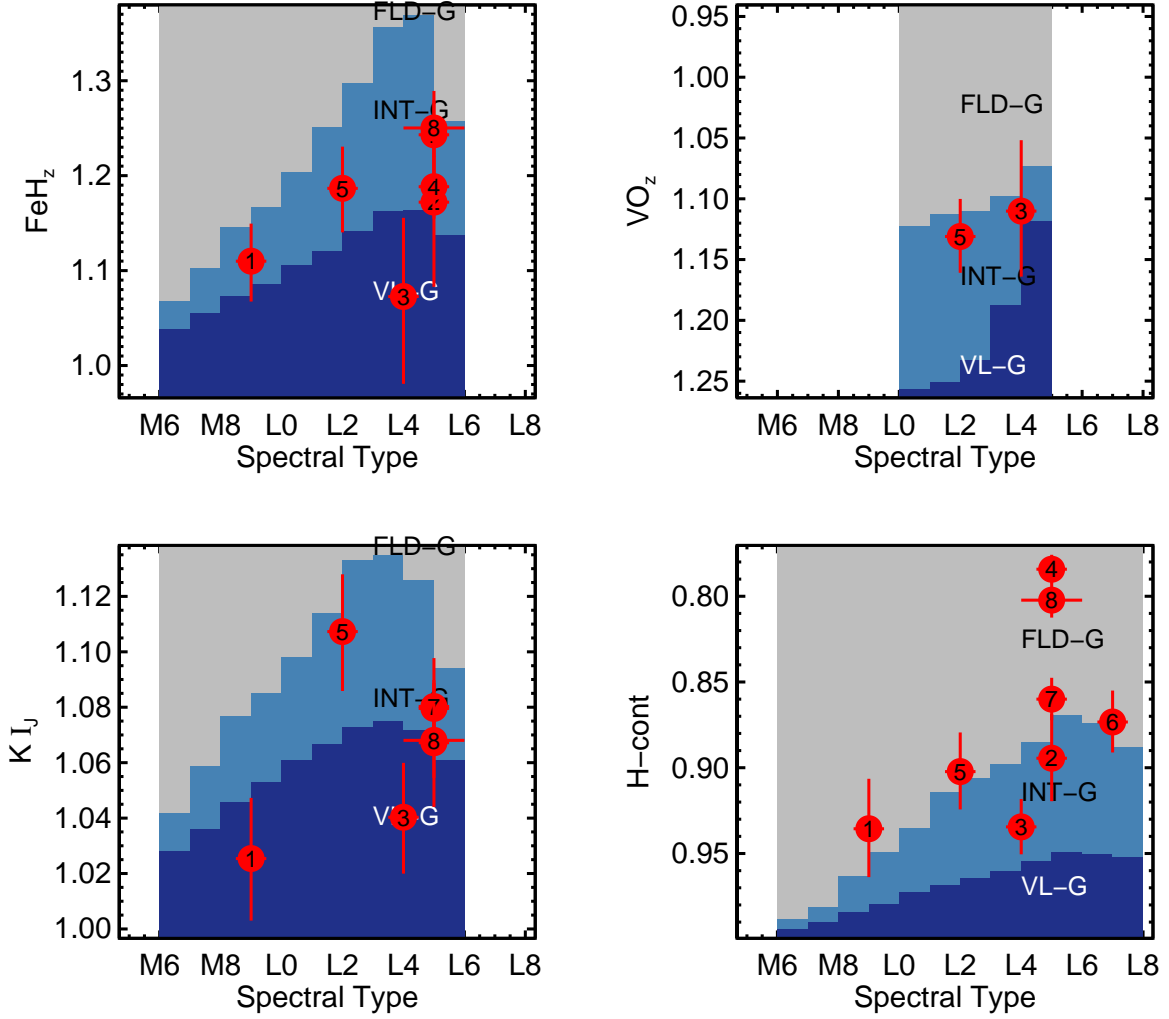


Fig. 14.— Same as Figure 12, but for objects whose index-based gravity classes we determine only tentatively due to modest S/N in the spectra.

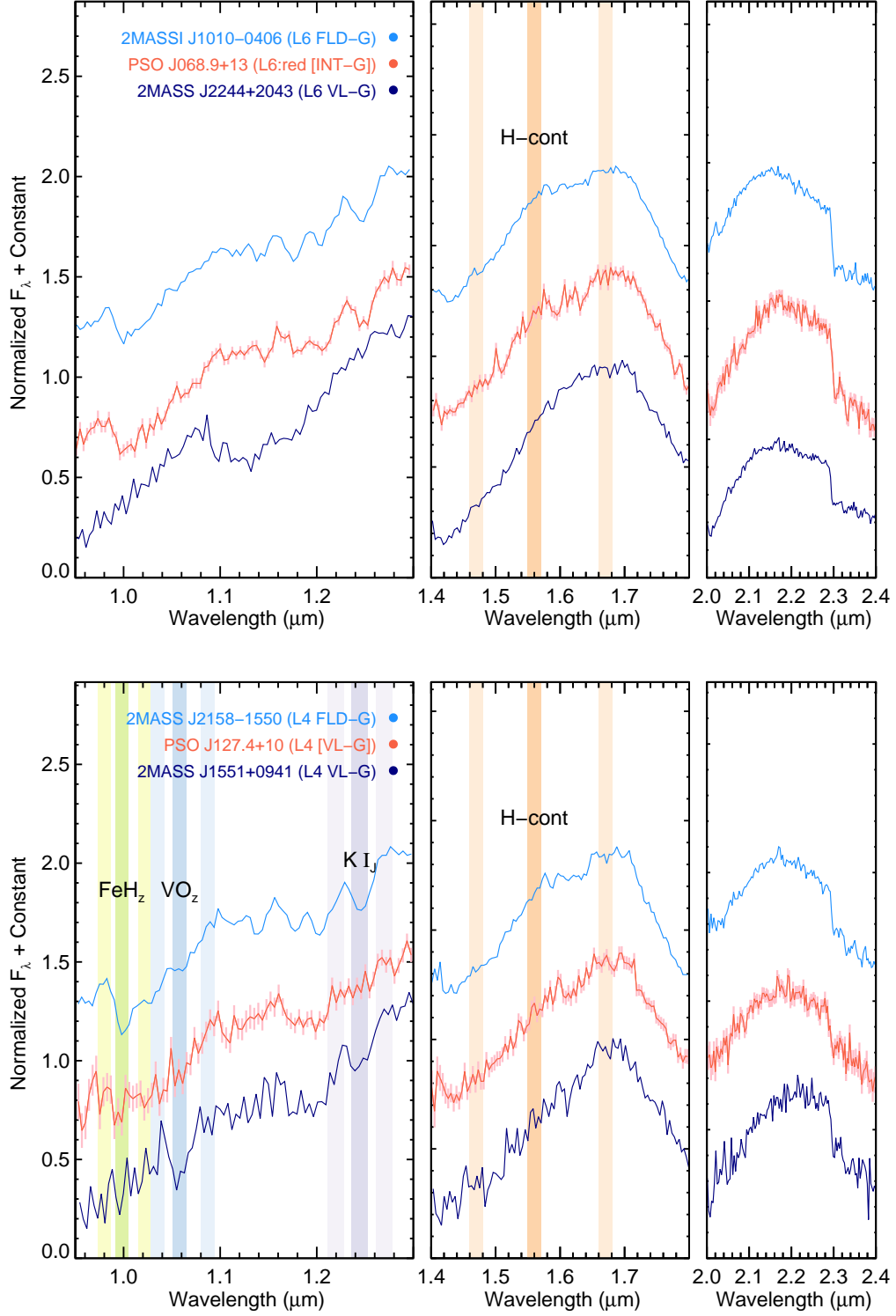


Fig. 15.— Same as Figure 13, but for objects whose index-based gravity classes we determine only tentatively (classes indicated in brackets as in Table 10) due to modest S/N in the spectra.

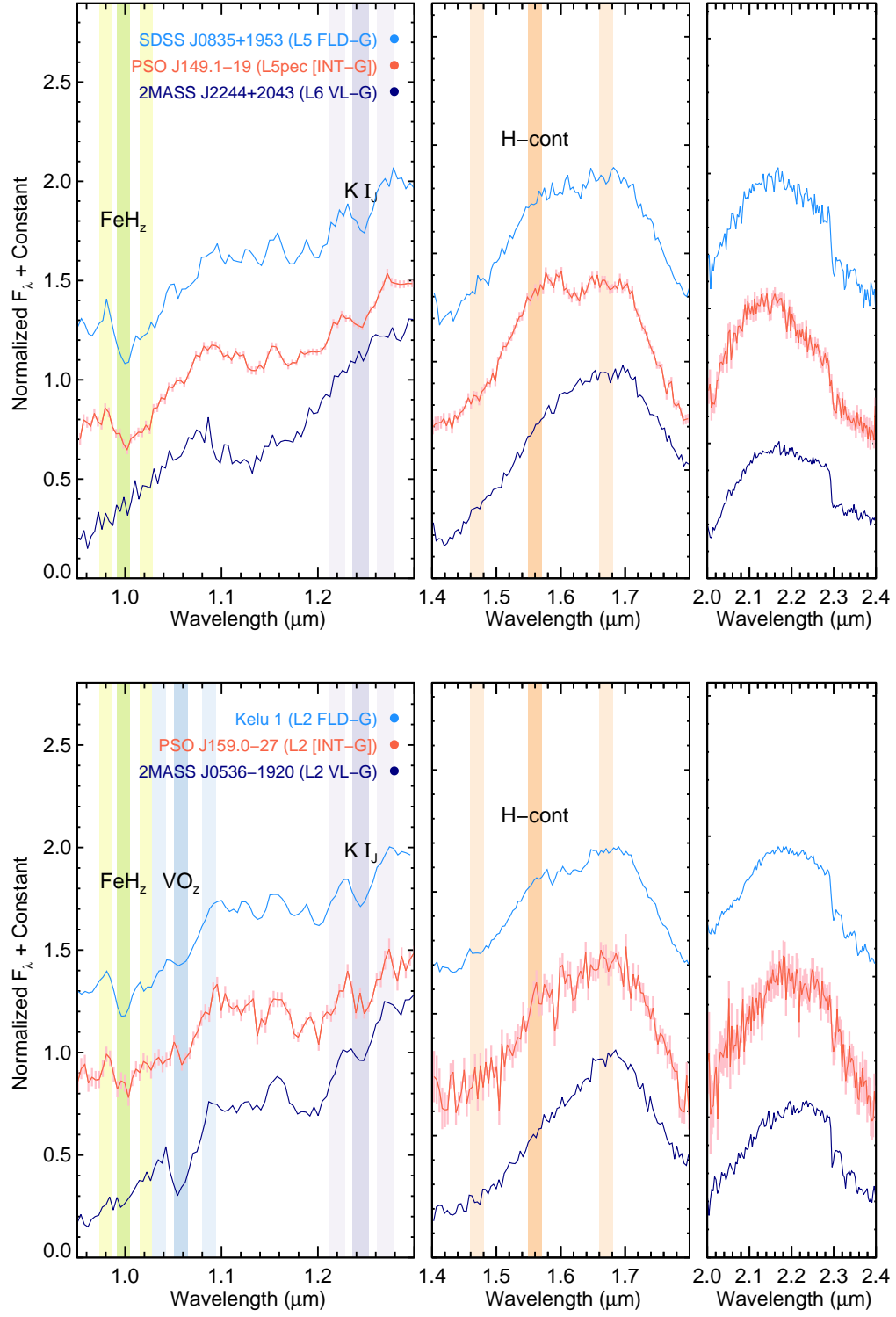


Fig. 15.— continued.

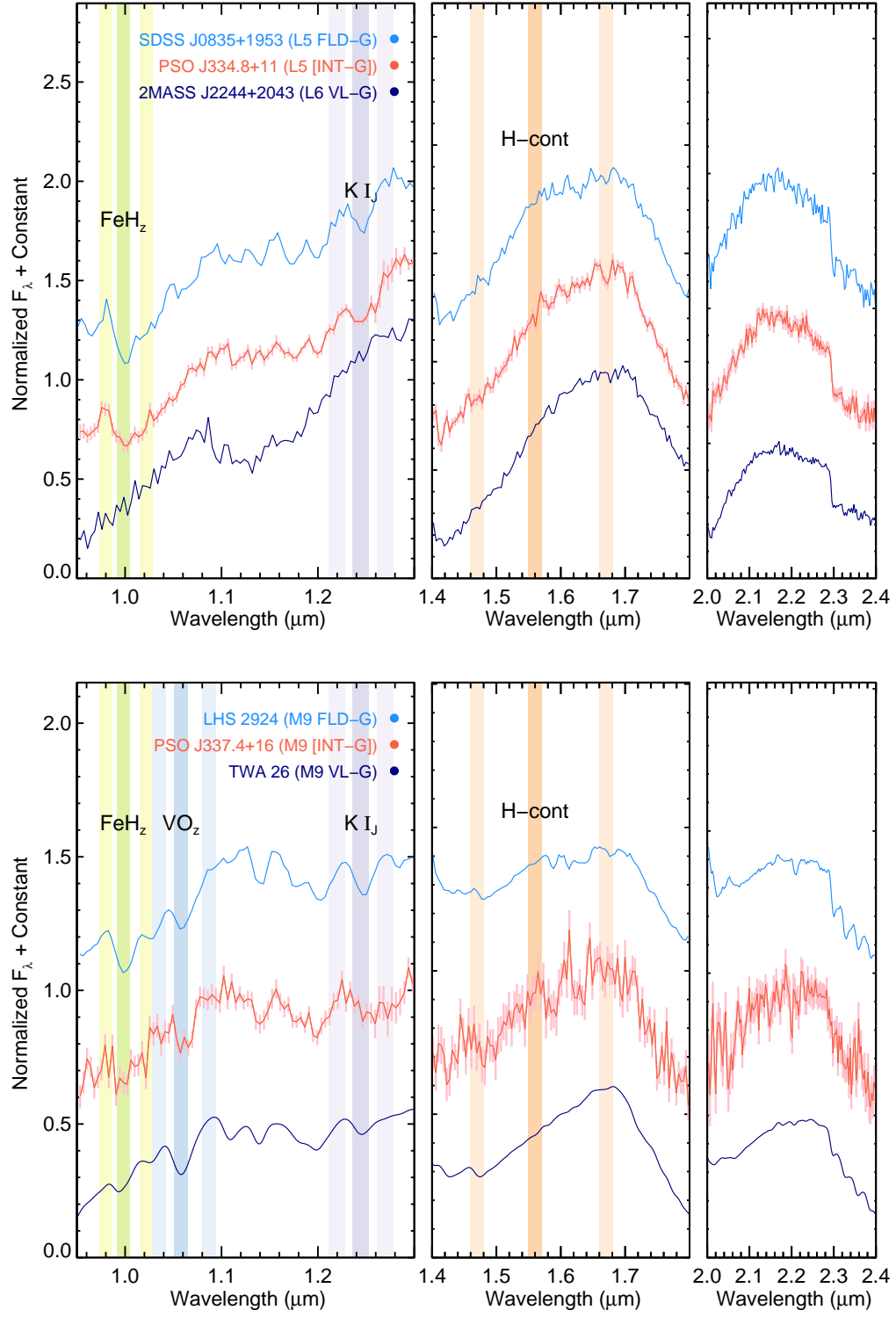


Fig. 15.— continued.

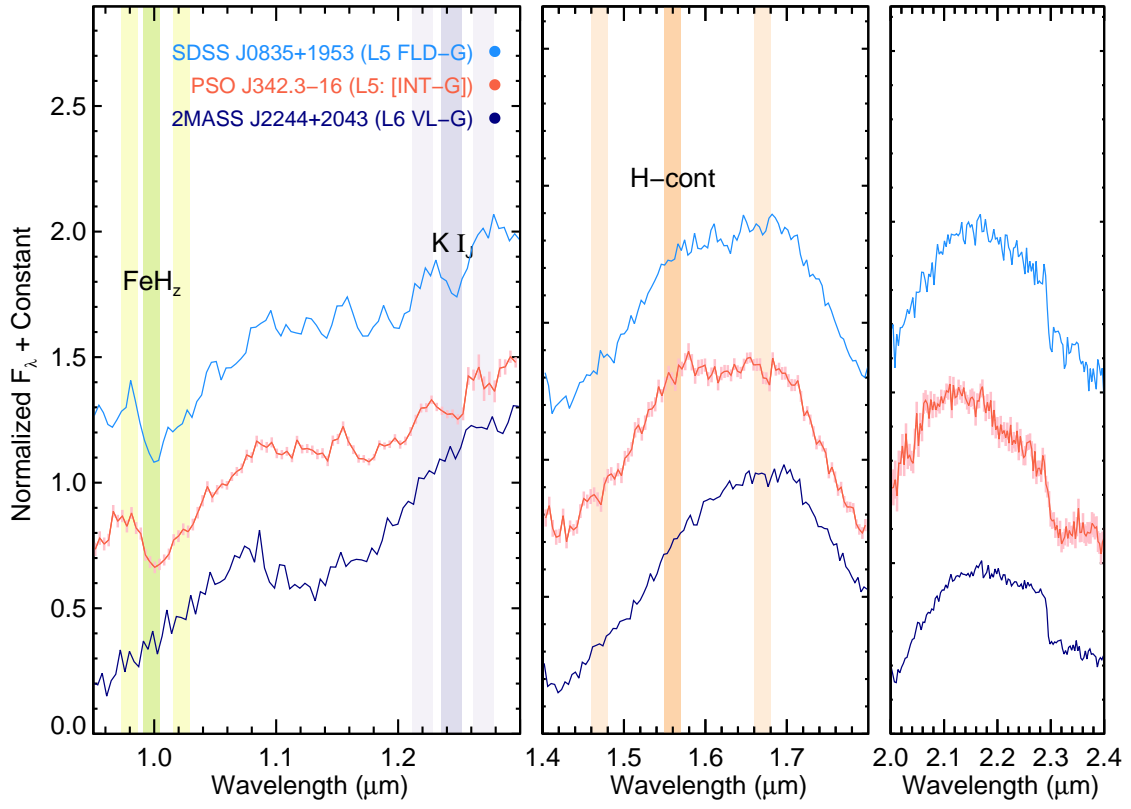


Fig. 15.— continued.

limit satisfied many index criteria but revealed no signs of spectral blends on visual inspection. We used the following scheme to identify strong, medium, and weak binary candidates. We ranked objects meeting at least 8 BG14 criteria or 4 B10 criteria as strong candidates. We ranked objects meeting at least 4 BG14 criteria or 3 B10 criteria, as well as objects having clear visual indications of blends plus at least 2 BG14 criteria or 1 B10 criterion, as medium candidates. We labeled other objects showing clear visual indications as weak candidates. This scheme is similar to those of BG14 and B10, but here we use three categories instead of two and we incorporate the results of visual inspection.

Overall, we identify 31 binary candidates (Table 12). We compare the spectra of our strong, medium, and weak binary candidates with those of field standards in Figures 16, 17, and 18, respectively. About 2/3 of these have spectral types L9–T2.5, broadly consistent with previous studies that suggested a higher observed frequency of binaries in the L/T transition (e.g., Liu et al. 2006; Burgasser 2007). Allers & Liu (2013b) demonstrated that the AL13 indices’ ability to identify low-gravity features is not affected by spectral blends. We find only one binary candidate (PSO J146.0+05) with mild hints of low gravity.

Below we briefly discuss individual binary candidates with notable spectral features.

4.5.1. *Strong Binary Candidates*

PSO J003.4–18 (2MASS J0013–1816) (L5 pec) — This object was independently discovered and typed by Baron et al. (2015) as an L1 dwarf and a common proper motion companion to the M3 dwarf NLTT 687. It satisfies 10 of the 12 BG14 criteria. The J band morphology of PSO J003.4–18 is closest to that of an L5 dwarf, but the deeply notched H band peak and a more subtle notch at $\approx 2.2 \mu\text{m}$ are both clear indications of methane. The peak in the J band at $1.3 \mu\text{m}$ and the overall blue color are further evidence of the presence of a T dwarf. Baron et al. (2015) used optical spectral indices to determine a spectral type, and their optical spectrum would be dominated by the primary and have very little flux from a T-type companion. PSO J003.4–18 is therefore very likely to be an early-L + early-T binary. As a companion to NLTT 687, it would also be a rare benchmark ultracool binary (Section 4.7).

PSO J049.1+26 (T2.5) — This object is a near-perfect spectral match to the T2+T7.5 binary 2MASS J12095613–1004008 (Burgasser et al. 2004; Liu et al. 2010). The J band shape fits the T2 standard best, but the H and K bands have the morphology of later-T dwarfs. This object satisfies 4 of the 6 B10 criteria.

PSO J071.6–24 (WISE J0446–2429) (L6 blue) — The J band morphology matches an L6 dwarf, but the peak in the J band at $\approx 1.3 \mu\text{m}$ suggests a later T dwarf, and the overall color and H and K band shapes match a T0 dwarf. Thompson et al. (2013) independently discovered this object and typed it L5 pec (blue), ascribing the unusual spectral features to thin large-grained clouds rather than a L+T blend. This object satisfies 8 of the 12 BG14 criteria.

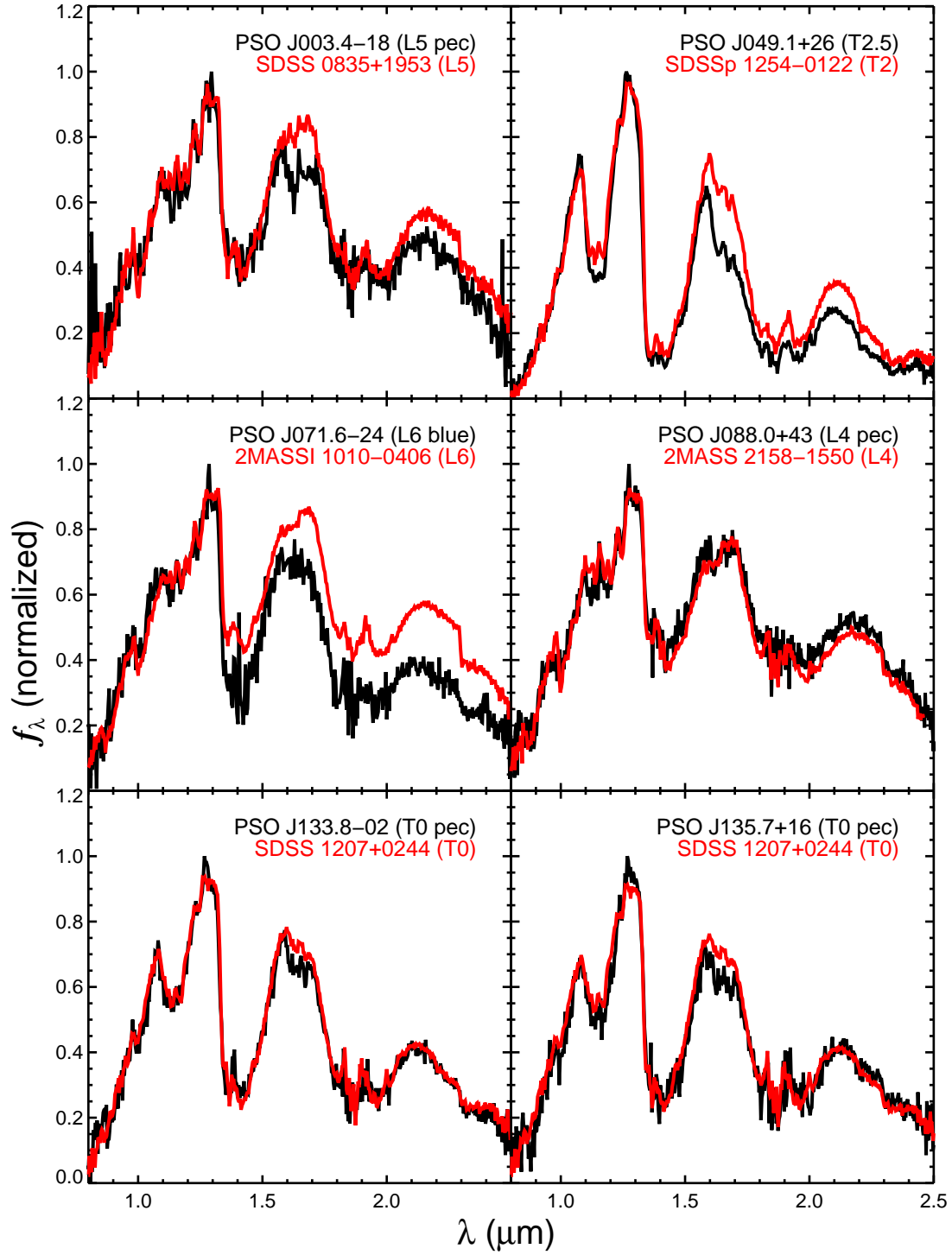


Fig. 16.— Plots comparing the spectra of our strong binary candidates (black) to the field standards of Kirkpatrick et al. (2010) and Burgasser et al. (2006) (red). Distinctive features of these spectra are discussed in Section 4.5.1.

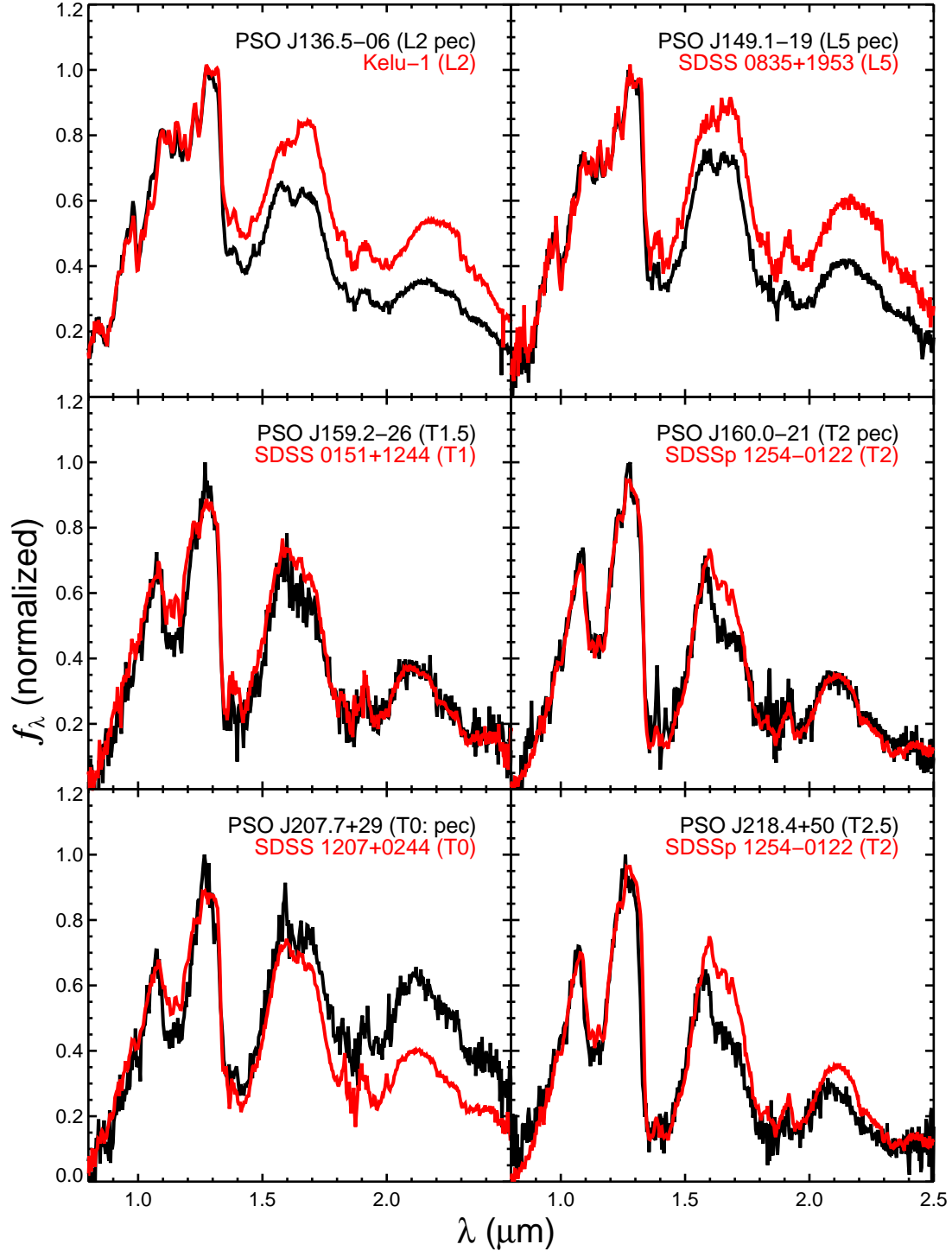


Fig. 16.— continued.

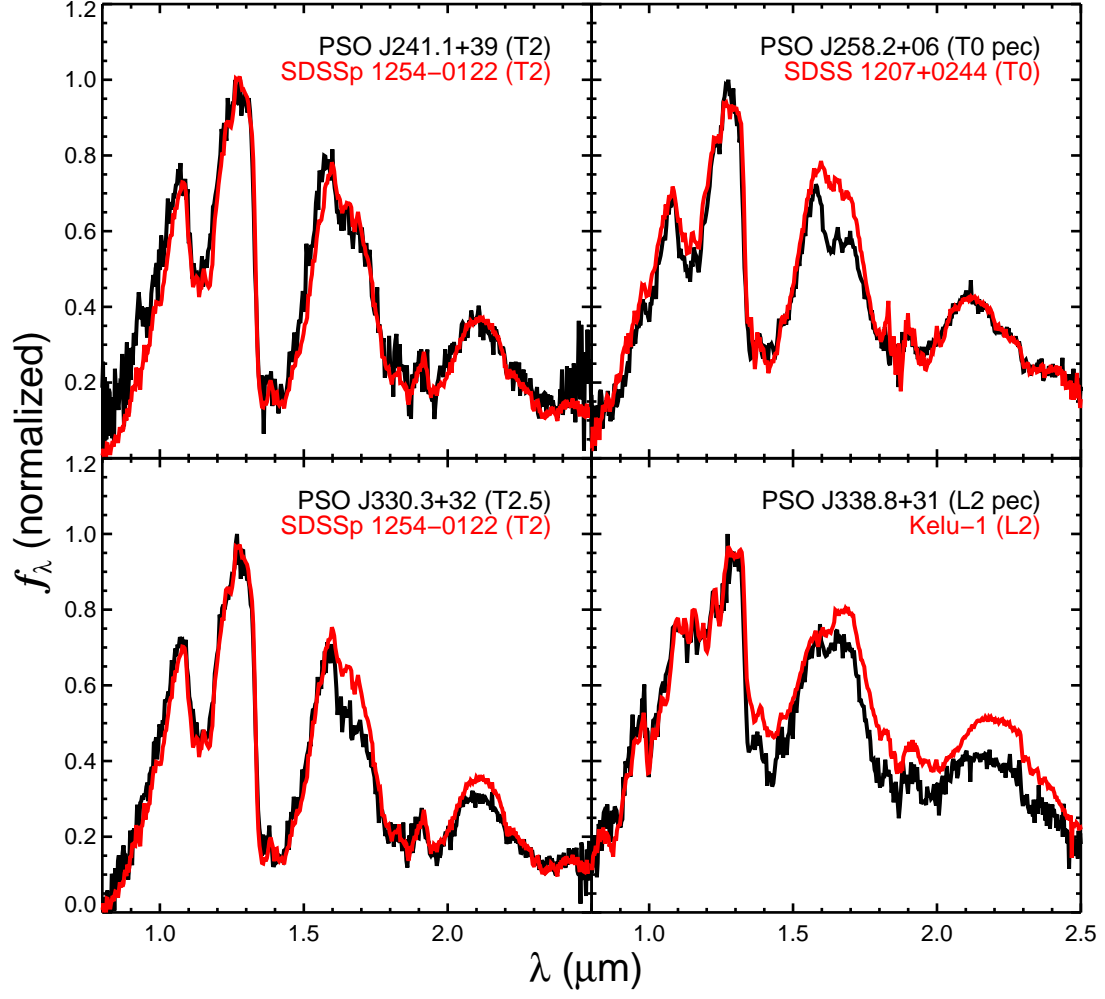


Fig. 16.— continued.

PSO J088.0+43 (L4 pec) — The J band peak at $\approx 1.28 \mu\text{m}$ and the notched H band suggest a mid-T dwarf blended with a normal L4 dwarf. This object satisfies 9 of the 12 BG14 criteria.

PSO J133.8–02 (T0 pec) — The spectrum fits the overall shape of the T0 standard quite well, but the J and H band peaks ($\approx 1.28 \mu\text{m}$ and $\approx 1.58 \mu\text{m}$, respectively) suggest the additional presence of a later-T dwarf. This object satisfies 5 of the 6 B10 criteria.

PSO J135.7+16 (T0 pec) — The overall morphology is closest to that of a T0 dwarf, but the J and H bands have the shapes of a T2 dwarf. This object satisfies all 6 of the B10 criteria.

PSO J136.5–06 (L2 pec) — The J band shape matches the L2 spectral standard fairly well, but the deeper water absorption band at $\approx 1.4 \mu\text{m}$ and the blue color suggest a later-type object, and the notched H band peak and depression at $\approx 2.2 \mu\text{m}$ both indicate the presence of methane. This object satisfies 9 of the 12 BG14 criteria.

PSO J149.1–19 (L5 pec) — The J band morphology is a clear match to L5, but the deeper water absorption band at $\approx 1.4 \mu\text{m}$ and the blue color indicate a later-type object. The notched H band peak and depression at $\approx 2.2 \mu\text{m}$ both point to methane and a T-dwarf companion. This object satisfies 10 of the 12 BG14 criteria.

PSO J159.2–26 (T1.5) — The K band shape is an excellent match to the T1 standard, but the J and H bands fit a T2 better. This object satisfies 4 of the 6 B10 criteria.

PSO J160.0–21 (T2 pec) — The overall slope of this spectrum matches that of the T2 standard, but the J band peak at $\approx 1.28 \mu\text{m}$ and the blue H band peak strongly suggest the presence of a late-T companion. This object satisfies all 6 of the B10 criteria.

PSO J207.7+29 (T0: pec) — This object has no good spectral matches among the L- and T-dwarf standards. The overall color is similar to an L9 dwarf, but the lower flux at $\approx 1.65 \mu\text{m}$ and $\approx 2.2 \mu\text{m}$ reveal the presence of methane, and the J band peak resembles a mid-T dwarf. This object satisfies all 6 of the B10 criteria.

PSO J218.4+50 (T2.5) — Similar to PSO J049.1+26, this object is a good spectral match to the known T2+T7.5 binary 2MASS J12095613–1004008 (Burgasser et al. 2004; Liu et al. 2010). The J band shape fits the T2 standard best but not well, and the H and K bands have the morphology of later-T dwarfs. This object satisfies 5 of the 6 B10 criteria.

PSO J241.1+39 (T2) — Overall and in the J band, this is a good match to the T2 standard, but the Y and H band peaks are bluer. This object satisfies 5 of the 6 B10 criteria.

PSO J258.2+06 (T0 pec) — The spectrum fits the overall color and K band shape of the T0 standard quite well, but the J and H band peaks resemble a later-T dwarf. This object satisfies all 6 of the B10 criteria.

PSO J330.3+32 (T2.5) — This object has unusually deep water absorption bands at $\approx 1.15 \mu\text{m}$ and $\approx 1.4 \mu\text{m}$ for a T2.5 dwarf, and satisfies 5 of the 6 B10 criteria. It is a common proper motion

companion to the star Wolf 1154 (Section 4.7), and therefore would be a rare ultracool benchmark if confirmed as a binary binary.

PSO J338.8+31 (L2 pec) — The spectrum is a good match to the L2 standard in the J band, but the overall slope and K band shape are more like those of a T0, and H band notch indicates methane. This object satisfies 8 of the 12 BG14 criteria.

4.5.2. Medium Binary Candidates

PSO J004.1+23 (T0) — The overall morphology closely resembles a T0 dwarf, but the H band shows no clear sign of methane while the J band peak resembles that of a T2 dwarf. The spectrum is a good match to the L6+T2 binary SDSSp J042348.57-041403.5 (Geballe et al. 2002; Burgasser et al. 2005). It meets 2 of the 6 B10 criteria.

PSO J100.5+41 (*WISE J0642+4101*) (L9 red) — This unusual object was independently identified by Mace et al. (2013), who classify it as “extremely red” without assigning a spectral type. We type it as L9 based on its $1.2 - 1.3 \mu\text{m}$ J band profile and the depth of its $\approx 1.4 \mu\text{m}$ water absorption band, and we concur with the very red color. The redness is most easily explained by large amounts of dusty condensates in the photosphere, but the object also satisfies 3 of the 6 B10 criteria.

PSO J103.0+41 (T0) — This object was identified by us as a candidate binary in Paper I, where it is discussed in detail. It is also a good match to the known L6+T2 binary SDSSp J042348.57-041403.5, and satisfies 2 of the 6 B10 criteria.

PSO J180.1–28 (T0) — This object matches the overall shape of the T0 standard fairly well but shows subtle signs of a companion later-T dwarf: the peak in the J band at $1.28 \mu\text{m}$ and the brighter peak in the K band. The J and H bands are also good matches to the L6+T2 binary SDSSp J042348.57-041403.5. PSO J180.1–28 meets 1 of the 6 B10 criteria.

PSO J272.0–04 (T1.5 pec) — The slope of this spectrum and the K band shape fall in between the T1 and T2 standards, but the depth of the $\approx 1.15 \mu\text{m}$ and $\approx 1.4 \mu\text{m}$ water absorption bands and the pointy J band peak suggest a later-type companion. This object satisfies 3 of the 6 B10 criteria.

PSO J277.7+45 (*WISE J1830+4542*) (L9) — This object, first identified by Kirkpatrick et al. (2011), fits the L9 standard in terms of overall color and morphology and J band shape, but there are signs of methane absorption at $\approx 1.65 \mu\text{m}$ and $\approx 2.2 \mu\text{m}$. It meets 3 of the 6 B10 criteria.

PSO J284.7+39 (T4) — This spectrum is a good match to the T4 standard, except for the narrow profile of the J band, which suggests the additional presence of a later T-dwarf. (The spike at $\approx 1.29 \mu\text{m}$ is likely a noise artifact.) This object satisfies 2 of the 6 B10 criteria.

PSO J319.3–29 (T0:) — Clear indications of methane absorption at $\approx 1.65 \mu\text{m}$ and $\approx 2.2 \mu\text{m}$ point to a T dwarf, while the J band shape and $\approx 1.15 \mu\text{m}$ and $\approx 1.4 \mu\text{m}$ water absorption band

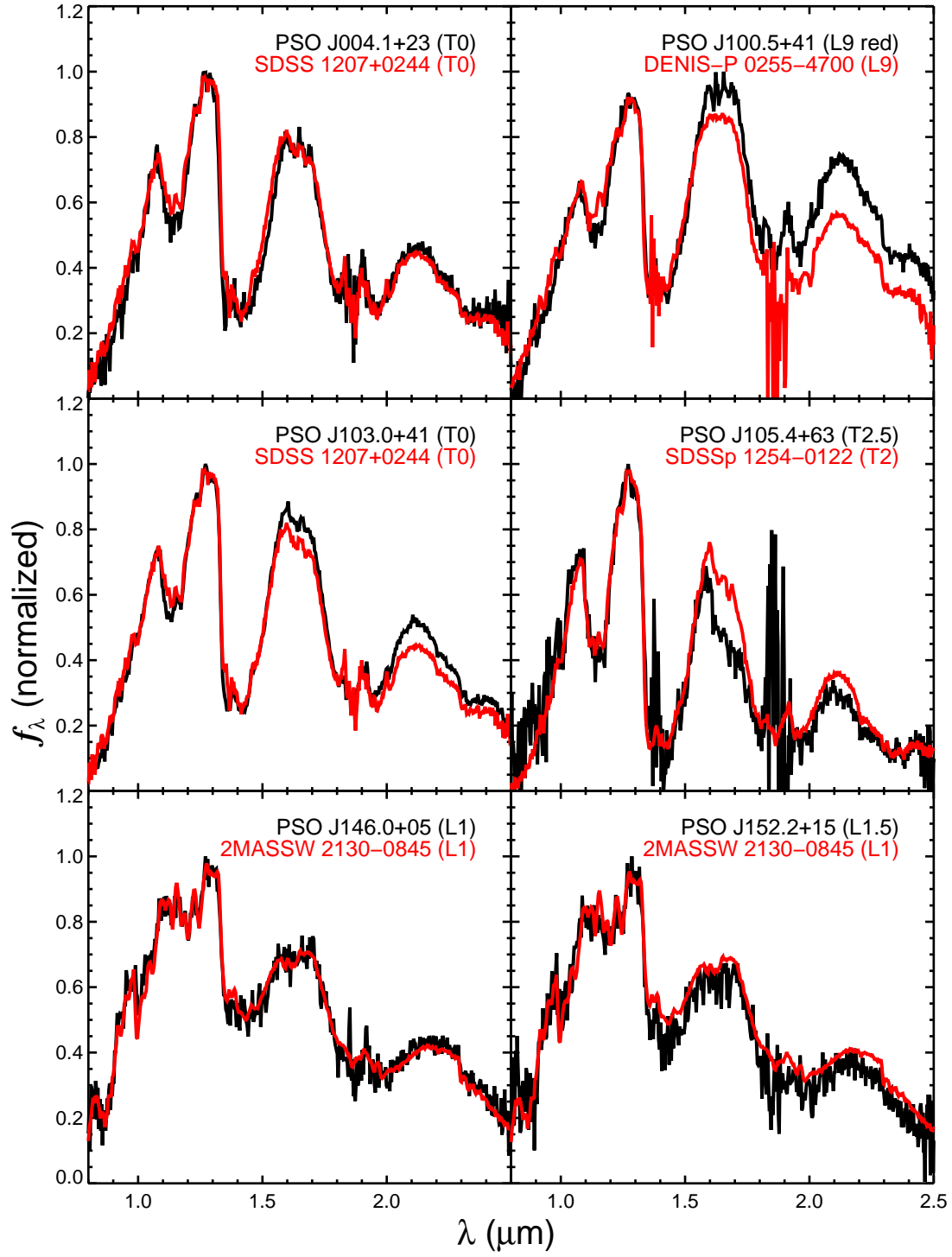


Fig. 17.— Same as Figure 16, but for our medium-ranked binary candidates. Distinctive features of these spectra are discussed in Section 4.5.2.

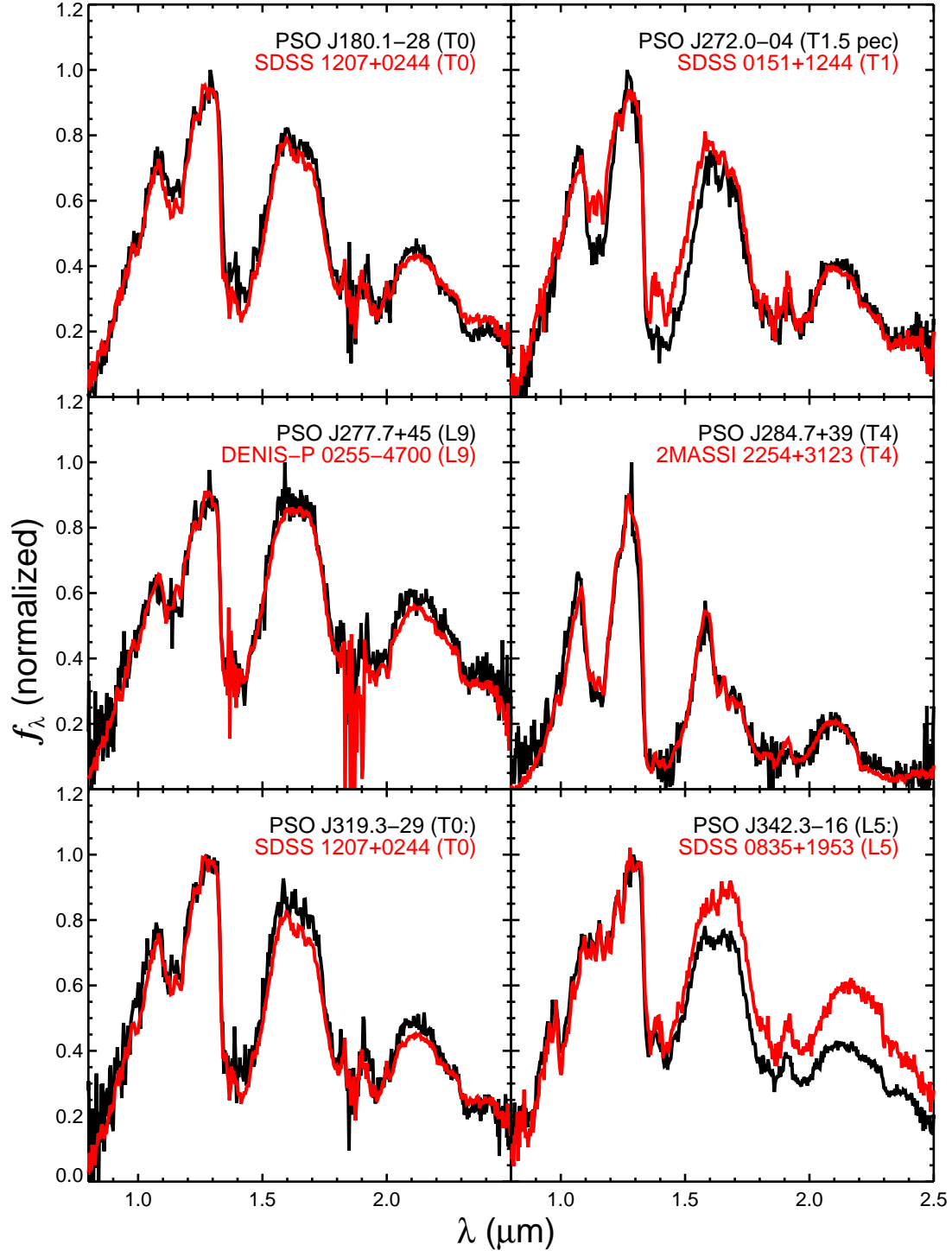


Fig. 17.— continued.

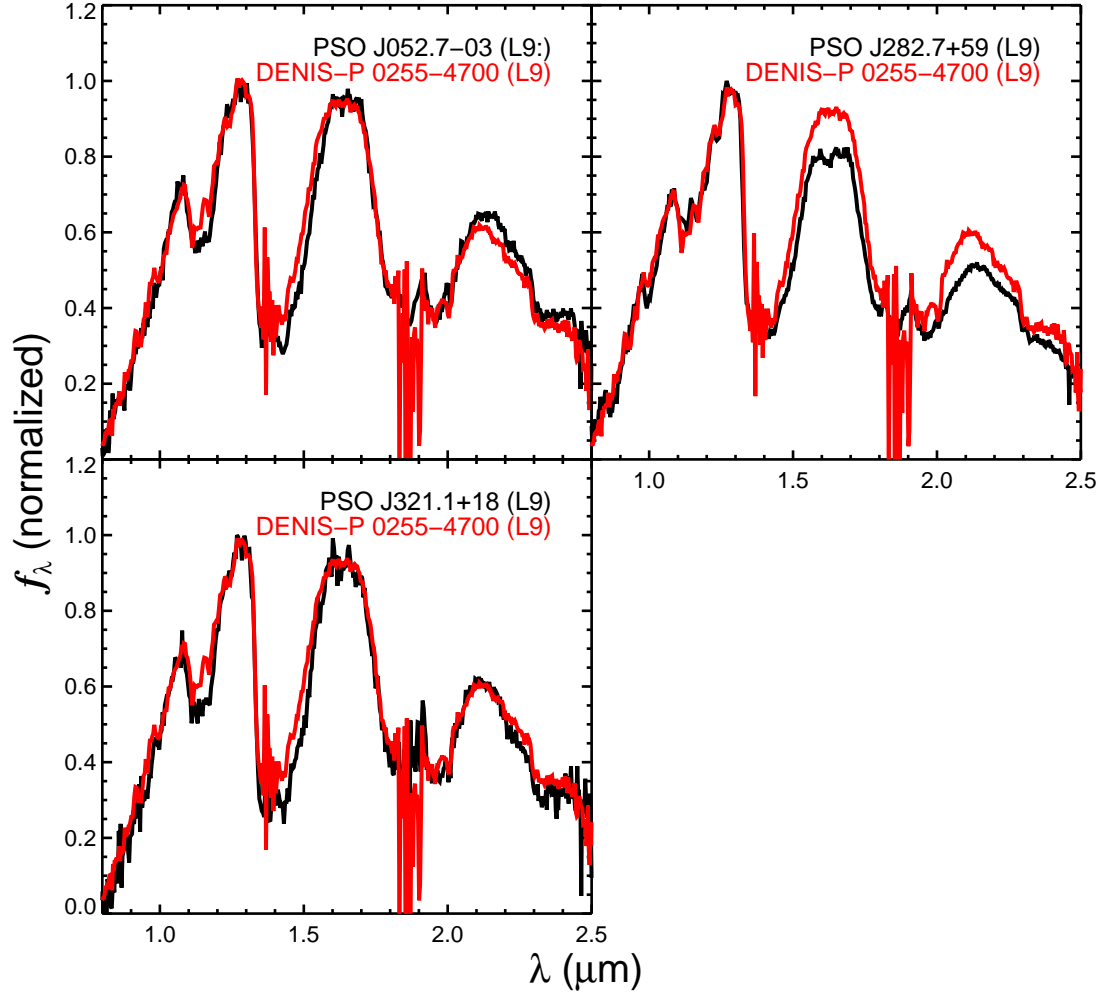


Fig. 18.— Same as Figure 16, but for our weak binary candidates. Distinctive features of these spectra are discussed in Section 4.5.3.

depths are more like the L9 standard. This object meets 2 of the 6 B10 criteria.

PSO J342.3–16 (L5:) — The J band morphology matches L5, but the H and K band shapes and the bluer color indicate the additional presence of a T dwarf. This object satisfies 5 of the 12 BG14 criteria.

4.5.3. Weak Binary Candidates

PSO J052.7–035 (L9:) — The best match for the J band profile and adjacent water absorption bands is the T0 standard, but the H band shows no sign of methane absorption and the overall slope fits the L9 standard.

PSO J282.7+59 (*WISE J1851+5935*) (L9) — This object was identified as a candidate binary in Paper I, where it is discussed in detail. Thompson et al. (2013) type the object as L9 pec, and also describe it as a candidate late-L + early-T binary. Surprisingly, our spectrum meets none of the B06 criteria.

PSO J321.1+18 (L9) — The overall slope clearly fits L9, but there is methane absorption at $\approx 2.2 \mu\text{m}$ and the water absorption bands at $\approx 1.15 \mu\text{m}$ and $\approx 1.4 \mu\text{m}$ have early-T dwarf depth.

4.6. Proper Motions and Kinematics

The motion through space of (sub)stellar objects represents their kinematic histories, as younger objects tend to have smaller tangential velocities (e.g., Wielen 1977). We calculated the proper motions for our discoveries using the individual PS1 epochs (≈ 25 – 30 epochs per object, mostly in z_{P1} and y_{P1}), along with their AllWISE reported positions. For the $\approx 70\%$ of our sample also detected in the 2MASS Point Source Catalog, we included those positions as well (these objects have 2MASS photometry listed in Table 2). The inclusion of the 2MASS astrometry improved the precision of our proper motions in many cases despite the fact that the per-epoch precision for the 2MASS positions is larger (≈ 70 mas) than for the PS1 positions (≈ 25 mas), as 2MASS increased the time baseline for our calculations from $2 - 4$ years to $\gtrsim 10$ years.

Our proper motions are presented in Table 4. Proper motions for 17 of our discoveries were previously published by other authors (Table 5), in addition to 7 by us in Paper I. Figure 19 demonstrates the consistency of our proper motions with those in the literature as well as our improved precision (typically by a factor of $2 - 3$).

We calculated photometric distances for our discoveries, using $W2$ magnitudes and the spectral type polynomial from Dupuy & Liu (2012). We used these photometric distances along with our proper motions to determine tangential velocities (v_{tan}) for our discoveries. These are also presented in Table 4, and we show the distribution of v_{tan} in Figure 20. The v_{tan} of our discoveries are overall

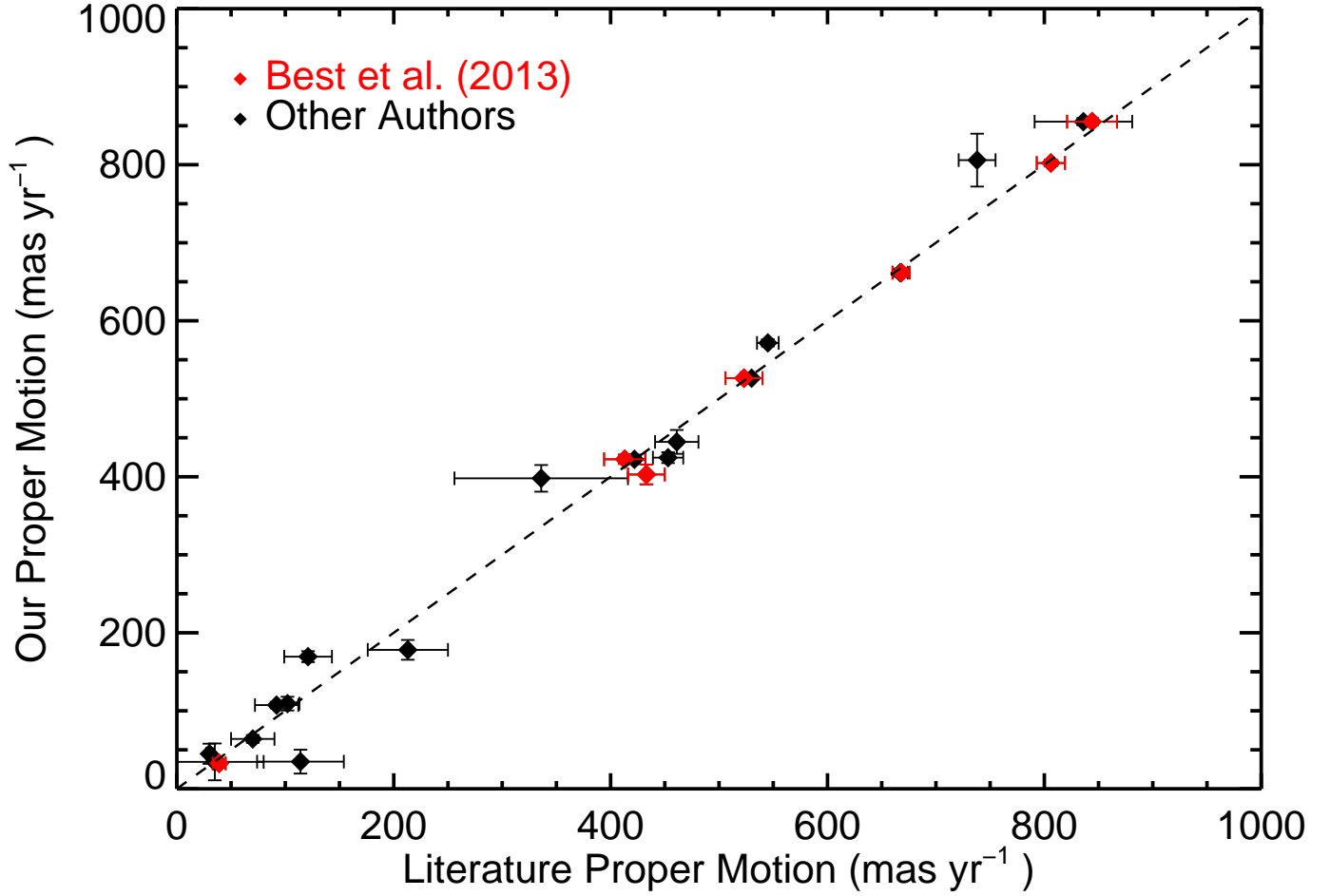


Fig. 19.— Comparison of our proper motions with previously published values from the literature. Objects plotted in red have proper motions in our Paper I, which we refine in this paper. Four objects have proper motions from Paper I as well as elsewhere in the literature, and we plot these as separate points. Our new proper motions are consistent with previous values and improve on the precision by a typical factor of 2 – 3.

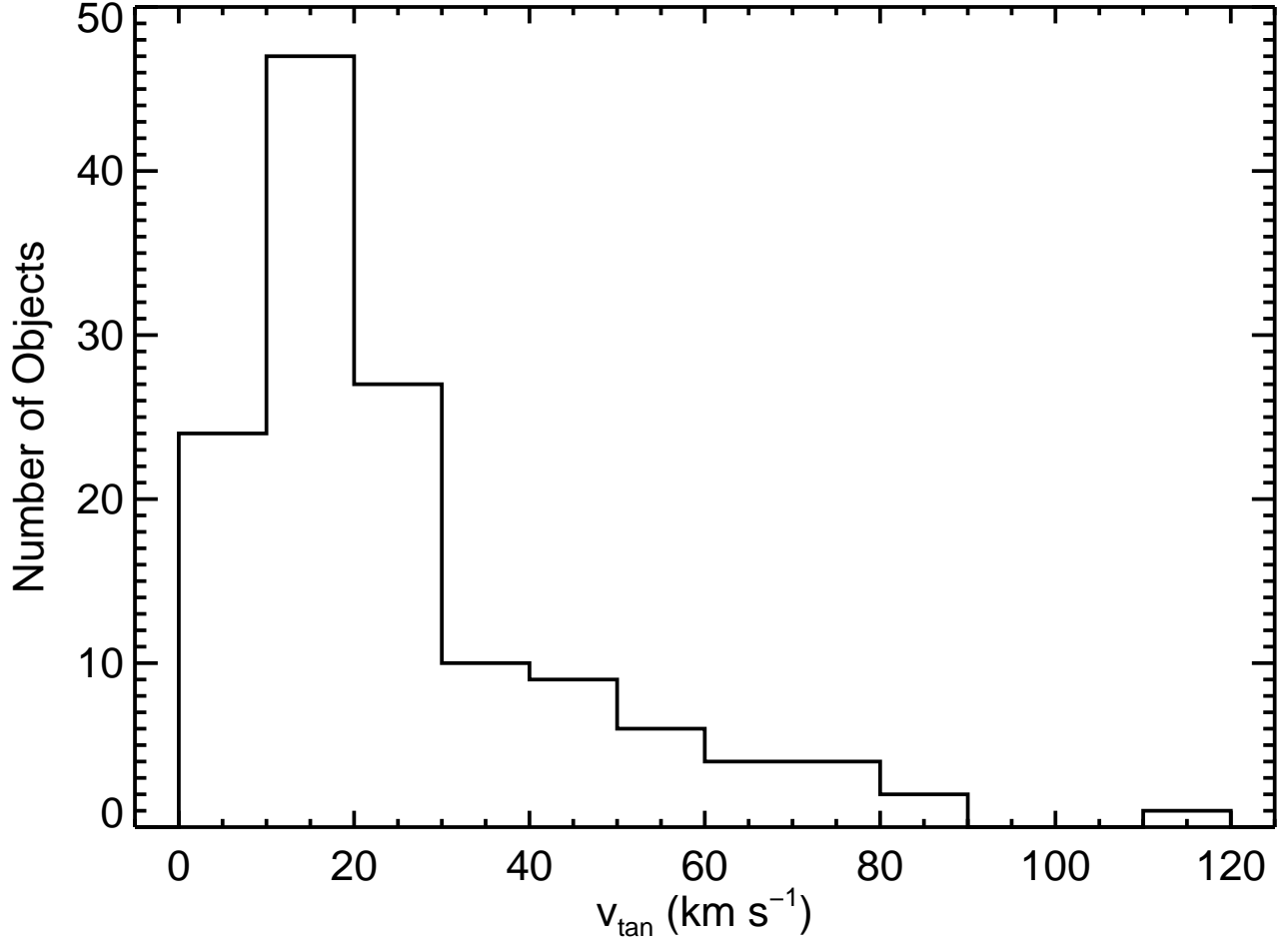


Fig. 20.— The distribution of tangential velocities for our discoveries. These v_{tan} indicate that our discoveries are all very likely to be members of the younger thin disk population.

$\approx 25\%$ lower than those of the 20 pc volume-limited sample presented in Faherty et al. (2009), making them fully consistent with the younger thin disk population. One object in our sample, PSO J329.8+03, has a notably larger velocity ($v_{\text{tan}} = 111 \pm 12 \text{ km s}^{-1}$). We applied the analysis of Dupuy & Liu (2012, see their Figure 31) and found this v_{tan} gives PSO J329.8+03 a $\approx 10\%$ chance of being a member of the thick disk. Older L dwarfs typically have bluer near-IR colors (Faherty et al. 2009), and while this age–color relationship has not been clearly established for early-T dwarfs, we note that PSO J329.8+03 has $(J - K)_{\text{MKO}} = 1.26 \pm 0.03 \text{ mag}$ which is in fact redder than the mean $(J - K)_{\text{MKO}} = 0.75 \pm 0.17 \text{ mag}$ for T1 dwarfs (Dupuy & Liu 2012). We consider PSO J329.8+03 to be a thin disk object along with the rest of our discoveries.

4.7. Comoving Companions

To identify if any of our discoveries were members of common proper motion systems, we cross-matched our discoveries with a large list of nearby stars from Lépine & Shara (2005), Salim & Gould (2003), Lépine & Gaidos (2011), Limoges et al. (2013), and Deacon & Hambly (2007). We searched for matches within 5 arcmin and identified eight possible pairs with proper motions differing by less than 5σ (where σ is the quadrature sum of the proper motion differences in each axis divided by the combined uncertainties in that axis). To test how many of these pairs were chance alignments of unrelated stars, we used the method of Lépine & Bongiorno (2007, see also Deacon et al. 2014). We offset the positions in our input catalog by 2° and repeated our matching criteria, generating entirely coincident pairings. The results are shown in Figure 21. Three of our prospective pairs lie outside the area dominated by coincident pairs.

Our three pairings are described in Table 13. One of the pairings, NLTT 687 and PSO J003.4–18, was previously discovered by Baron et al. (2015). Two of our secondaries, PSO J003.4–18 and PSO J334.1+19, are identified as candidate binaries (Section 4.5.1). If these are indeed binaries then these systems will be hierarchical triples. Such systems are useful benchmarks as the primaries can be used to constrain their ages and metallicities, allowing evolutionary models to estimate the masses, radii, and effective temperatures of the binary components. If the secondary can be resolved with high-resolution imaging into two components, their masses can be measured dynamically, providing a rigorous test of the evolutionary models. We also identify PSO J334.1+19 as a possible β Pictoris Moving Group member ($p = 77.8\%$, Section 6.2.1). Using the BANYAN II online tool (Gagné et al. 2014) we found that its primary LSPM J2216+1952 is also a possible ($p = 58.2\%$) member of this moving group.

5. The Atmospheres of L/T Transition Dwarfs

The significant changes in the spectra and blueward shift in near-IR colors of brown dwarfs cooling through the L/T transition arise from the formation of methane and the depletion of pho-

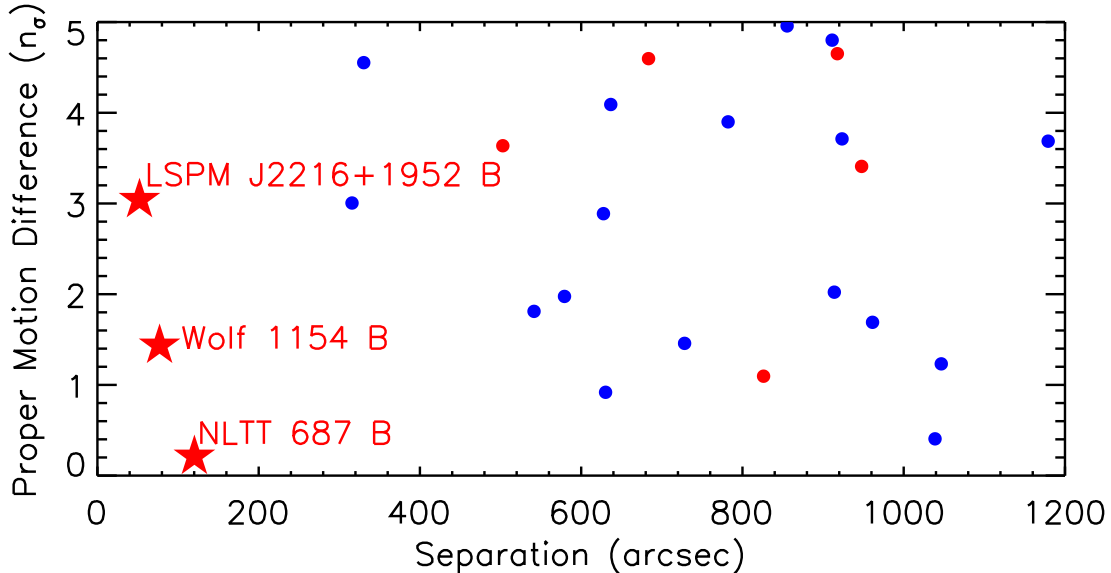


Fig. 21.— Our common proper motion systems (marked as red stars). The offset coincident pairings generated using the method of Lépine & Bongiorno (2007) are shown as blue dots. The remaining pairings (which are likely to be coincident) are shown as red dots.

atmospheric condensate clouds. (e.g., Allard et al. 2001; Burrows et al. 2006; Saumon & Marley 2008). The process by which the clouds deplete is not well understood, and proposed scenarios involve the clouds gradually thinning, raining out suddenly, or breaking up (e.g., Ackerman & Marley 2001; Knapp et al. 2004; Tsuji 2005; Burrows et al. 2006; Marley et al. 2010). The manner in which clouds disappear from the photosphere may impact the cooling rate, and therefore the luminosities, of the brown dwarfs (Saumon & Marley 2008; Dupuy et al. 2015a). The colors of L/T transition objects can therefore shed light on the cloud dispersal process(es).

An accumulation of objects at a given color on the cooling sequence would indicate a long-live phase of evolution, with objects spending a longer time at the temperature corresponding to that color. The “hybrid” evolutionary models of Saumon & Marley (2008) predict a pile-up of objects in the L/T transition at $(J - K)_{\text{MKO}} \approx 0.9 - 1.0$, as cloud clearing removes opacity from the photospheres of brown dwarfs and the cooling slows as entropy is released from deeper atmospheric layers. Dupuy & Liu (2012) found evidence of this type of pile-up and a subsequent gap (i.e., a short-lived evolutionary phase) in the distribution of near-IR colors of 36 L/T transition dwarfs (selected by absolute H_{MKO} magnitudes).

By combining our new discoveries with objects from the literature, we have built a larger sample of L/T transition dwarfs. We used parallaxes when available and photometric distances otherwise to construct a sample of 70 objects with spectral types L7–T5.5, volume-limited at 25 pc. In Figure 22, we show the distribution of $(J - K)_{\text{MKO}}$ colors for this sample, computed in a Monte Carlo fashion

accounting for errors in the photometry. This color distribution suggests pile-ups and gaps across the L/T transition. The most prominent gap is at $(J - K)_{\text{MKO}} \approx -0.1 - 0.5$ mag, somewhat broader and shallower than the gap at $(J - K)_{\text{MKO}} \approx 0.0 - 0.4$ mag detected by Dupuy & Liu (2012). We also find a less prominent pileup just redward of the gap than Dupuy & Liu (2012), but there may also be larger pileups at $(J - K)_{\text{MKO}} \approx 1.2$ and 1.6 mag.

Our larger sample supports the existence of the “L/T gap”, but also makes clear that a larger sample, ideally volume-limited and defined entirely by trigonometric distances, is needed to fully delineate the color evolution in the L/T transition.

6. Young Discoveries

6.1. Field Objects

Stars with ages $\lesssim 200$ Myr are expected to be rare within 100 pc of the Sun, at most a few percent of the population for a uniform star-forming history. Our search was designed to identify field L/T transition dwarfs and generally avoided known star-forming regions, so we were surprised to find 23 of our 59 M7–L7 discoveries showing confirmed or possible spectral signatures of low gravity, i.e., youth (Section 4.4), and we explored why this happened.

Typically, young ultracool dwarfs are redder than older objects with the same spectral types in the photometric bands we used to select candidates (e.g., Gizis et al. 2012). They are also expected to be more luminous at longer wavelengths (i.e., in the mid-infrared WISE bands) due to both enhanced clouds and larger radii at younger ages. It is therefore natural to assume that our selection criteria, which screened out bluer and fainter objects, biased our candidates toward young brown dwarfs. To test this assumption, we assembled a set of FLD-G objects from our discoveries, AL13, and objects in the SpeX Prism Library³. We also gathered published objects with optical (β or γ ; Cruz et al. 2009) or near-infrared (INT-G or VL-G; Allers & Liu 2013a) classifications of low gravity. Figure 23 compares the $W1$ magnitudes vs. $W1 - W2$ colors for these sets of older and young objects. The two sets are drawn from multiple searches and sources, and we do not attempt to untangle the biases and selection effects. Nevertheless, Figure 23 suggests that our search criteria are indeed prone to selecting a disproportionately large number of young M and L dwarfs compared to the field population.

6.2. Young Moving Groups

Young moving groups (YMG) are associations of young stars (≈ 10 –100 Myr) and brown dwarfs whose similar trajectories through space imply that the members originated in a common star-

³<http://pono.ucsd.edu/~adam/browndwarfs/spexprism>

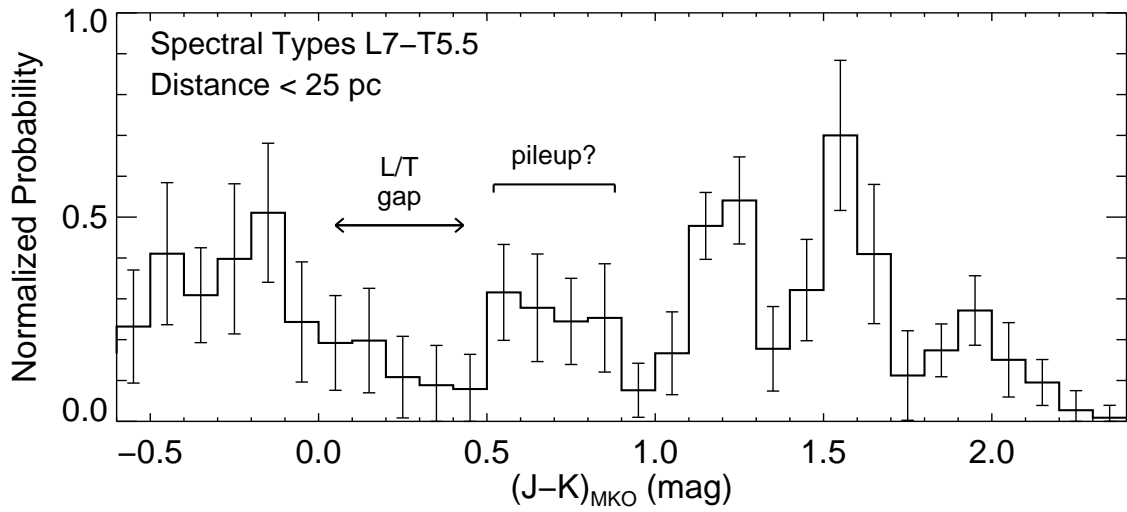


Fig. 22.— Distribution of $(J - K)_{\text{MKO}}$ colors for 70 objects with spectral types L7–T5.5 and distances within 25 pc, including our discoveries and objects from the literature. The histogram was computed in a Monte Carlo fashion, accounting for errors in the photometry. The plotted uncertainties are the standard deviations for each color bin derived from the Monte Carlo simulations. The color distribution reveals signs of structure in the L/T transition, in particular the gap at $(J - K)_{\text{MKO}} = 0.0 - 0.5$ mag first detected by Dupuy & Liu (2012), although the shape seen here is somewhat broader and shallower. We also detect a less prominent pileup just redward of the gap than Dupuy & Liu (2012), but see larger pileups at redder colors.

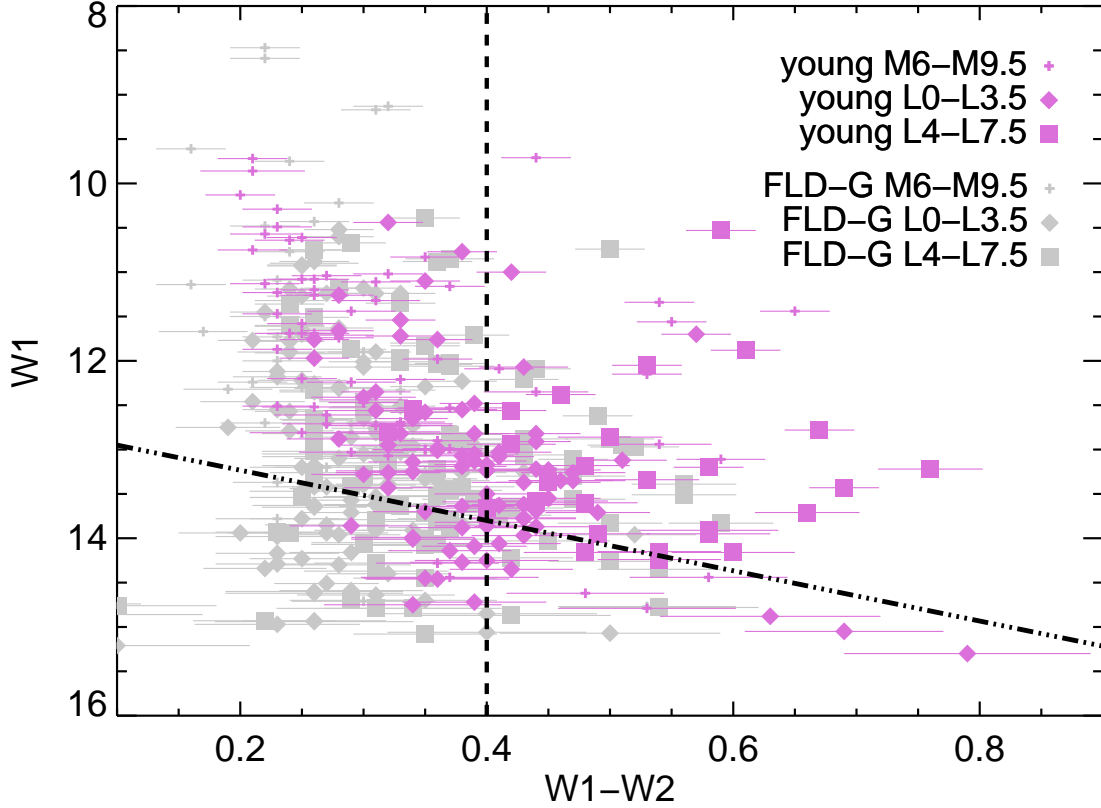


Fig. 23.— $W1$ vs. $W1 - W2$ photometry for confirmed young objects (magenta, with symbols according to spectral type — see legend at upper right) and FLD-G objects (light gray, same symbols) from AL13, this paper, and the SpeX Prism Library. The vertical dashed line marks the $W1 - W2 \geq 0.4$ mag selection criterion for our sample, while the diagonal dash-dot line shows the $W1$ vs. $W1 - W2$ line from Figure 1 that we used to identify candidates likely to be within 25 pc. The samples here are drawn from different searches and likely influenced by multiple biases, but there is clear indication that the two criteria select (above and to the right of the lines) a disproportionately large number of young M and L dwarfs compared to the field population.

forming region (e.g., Zuckerman & Song 2004). YMG members are coeval, and therefore serve as both benchmarks for stellar and substellar atmospheres and as empirical laboratories for testing models of star formation. In addition, these young stars are prime targets for direct imaging searches for nearby exoplanets. Our search targeted field brown dwarfs without regard to age or space motion, but we investigated the possibility that we had serendipitously stumbled upon members of YMGs.

6.2.1. Candidates Selected With BANYAN II

We used the BANYAN II online tool (Malo et al. 2013; Gagné et al. 2014) to calculate probabilities of membership in nearby YMGs for our discoveries. BANYAN II determines membership probabilities in a Bayesian fashion using sky position and proper motion, as well as radial velocity and distance when available. We computed photometric distances using K_{MKO} magnitudes (and the appropriate polynomial from Dupuy & Liu 2012) because the absolute magnitudes of young objects and field objects are most similar in this bandpass (Gagné et al. 2015c, M. C. Liu et al., in preparation). (We caution that photometric distances will not be accurate for objects that are unresolved equal-luminosity binaries.) Based on our sky positions, proper motions, and K_{MKO} photometric parallaxes, BANYAN II found that 10 of our discoveries have a $\gtrsim 70\%$ probability of membership in a YMG (Table 14) and a corresponding false alarm rate of $\lesssim 10\%$ (Gagné et al. 2014).

Interestingly, our 10 candidates all have spectral types L7–T4.5, which would place any of them among the lowest-mass and coolest YMG members discovered to date. We estimated their masses assuming membership in their respective candidate YMGs, which have ages 149^{+51}_{-19} Myr for AB Doradus and 24 ± 3 Myr for β Pictoris (Bell et al. 2015), and 40 ± 10 Myr for Argus (Makarov & Urban 2000; Torres et al. 2008). We note that the Argus association lacks consensus in the literature about whether it is a real YMG, and if real its membership list is not yet well-defined (e.g., Bell et al. 2015). To estimate masses for our YMG candidates, we first calculated the L_{bol} for each object using our spectral types, the K_{MKO} bolometric corrections of Liu et al. (2010, their Table 6), and the K_{MKO} -band photometric distance for each object. We then used the “hybrid” evolutionary models of Saumon & Marley (2008) and our L_{bol} values to determine masses at the age of each candidate’s YMG. Our final mass estimates are included in Table 14. We propagated the uncertainties on our spectral types, K_{MKO} magnitudes, bolometric corrections (Liu et al. 2010), distances, and ages into our mass determinations using Monte Carlo simulations and normal distributions for each uncertainty, and we quote 68th percentile confidence limits. Mass estimates for these objects, assuming they are YMG members, are $\approx 6\text{--}15 M_{\text{Jup}}$, spanning the deuterium-burning limit and comparable to the lowest-mass free-floating objects ever discovered (Liu et al. 2013; Gagné et al. 2015a).

We also repeat the warning of Shkolnik et al. (2012) and others that the spatial and kinematic locations of YMGs can be contaminated by unrelated field objects, so other indications of youth in a candidate are helpful for confirming membership. Unfortunately for our candidates, the AL13 gravity indices apply only to objects with spectral types $\leq \text{L7}$, and the spectra for our two L7 YMG

candidates have $S/N < 30$ so we do not regard their indices as reliable. More generally, low-gravity spectral signatures in the L/T transition are not as well established as for earlier-type objects. The young (100 ± 30 Myr) T3.5 dwarf GU Psc b (Naud et al. 2014) has an unusually red $J - K_s$ color for its spectral type, but it is not known whether this is true for other young early-T dwarfs. We do not see unusually red near-IR colors in our T dwarf YMG candidates.

The most promising of our candidate YMG members is PSO J057.2+15.2 (L7), whose spectrum reveals the triangular H band profile typical of youth, and whose $(J - K)_{2\text{MASS}} = 2.28 \pm 0.25$ mag color is significantly redder than the average $(J - K)_{2\text{MASS}} = 1.77 \pm 0.22$ mag for L7 dwarfs (Schmidt et al. 2010). The BANYAN II online tool gives a 91.9% probability of membership in the β Pictoris Moving Group (β PMG; Zuckerman et al. 2001) based on proper motion and photometric distance. If confirmed, this object would provide a nearby (32 ± 4 pc) target for atmospheric studies with a well-constrained age. We estimate this object would have a mass of $8.1^{+1.8}_{-1.5} M_{\text{Jup}}$, firmly in the planetary regime, and comparable to the latest known β PMG member PSO J318.5338–22.8603 (spectral type L7 Liu et al. 2013).

Two other L dwarf candidates have unusually red near-IR colors for their spectral type, consistent with being low-gravity and thus young:

PSO J004.7+51 — The BANYAN II online tool gives this L7 dwarf a 79.9% probability of membership in the Argus Moving Group (ARG; Zuckerman et al. 2001). We estimate it would have a mass of $10.3^{+1.4}_{-1.2} M_{\text{Jup}}$.

PSO J100.5+41 (WISE 0642+4101) — The BANYAN II online tool gives this red L9 dwarf a 78.6% probability of membership in the AB Doradus Moving Group (ABDMG; Zuckerman et al. 2004). We estimate it would have a mass of $15^{+4}_{-3} M_{\text{Jup}}$.

6.2.2. BASS Catalog

We cross-matched our discoveries with the BASS catalog presented in Gagné et al. (2015b). The BASS catalog contains 252 ultracool candidate YMG members with spectral types $\geq M5$ selected in a Bayesian fashion by the full BANYAN II methodology (Malo et al. 2013; Gagné et al. 2014), which incorporates 2MASS and *WISE* photometry in addition to the sky position, proper motion, radial velocity, and parallax used by the online tool. We found only one of our discoveries in BASS: the unusually red L dwarf PSO J100.5+41 (first identified as WISE 0642+4101 by Mace et al. 2013). Gagné et al. (2015b) give this object a 38.4% probability of membership in ABDMG, more pessimistic than the 78.6% probability based on our data and the online tool. Gagné et al. (2015b) also present an LP-BASS catalog with 249 “low-priority” candidates; none of these are among our discoveries. We note that our search for L/T transition dwarfs targeted a somewhat different parameter space. The majority of our discoveries are near the Galactic plane ($|b| < 15^\circ$), too faint (poor-quality or non-existent 2MASS photometry), or too blue (L/T transition objects have bluer $J - H$ colors than earlier-L dwarfs) to satisfy the criteria used to construct the BASS

sample.

7. Summary

We have conducted a successful search for nearby L/T transition dwarfs using a merged Pan-STARRS1 3π + *WISE* database as our primary resource, supplemented by near-infrared photometry from 2MASS, UKIDSS, and our own observations. Our search has yielded 130 ultracool dwarfs over $\approx 28,000$ deg² of sky. Of these, 79 objects have spectral types L6–T4.5, the largest number of L/T transition dwarfs discovered in any single search to date. Thirty of the L/T transition dwarfs have photometric distances less than 25 pc, and for spectral types L9–T1.5 we have increased the number of known objects within 25 pc by over 50%. We have analyzed the near-infrared colors of our L/T transition discoveries, and we find further evidence for the pile-up in the L/T transition first predicted by the “hybrid” evolutionary models of Saumon & Marley (2008) as well as a subsequent L/T gap first seen by Dupuy & Liu (2012).

We assigned spectral types to our discoveries by visual comparison with field spectral standards, and we compare these to types assigned using the index-based methods of Allers & Liu (2013a, M4–L7 dwarfs) and Burgasser et al. (2006, L0–T8 dwarfs). We find that the Allers & Liu (2013a) method assigns spectral types generally in agreement with visually assigned types for most objects, but earlier (by ≈ 0.5 –1 subtypes) for unusually red M and L dwarfs. The spectral types assigned by the indices of Burgasser et al. (2006) are in good agreement with visual types for T dwarfs but may be different by ≈ 0.5 –1.0 subtypes for L dwarfs.

Among the late-M to mid-L dwarfs in our sample, we found a total of 23 objects with spectral signatures of low gravity, indicating youth. Using the gravity-sensitive indices of Allers & Liu (2013a), we classify nine of these discoveries as VL-G and one as INT-G. We assign provisional VL-G and INT-G classifications to seven more objects based on spectra with modest S/N; higher S/N spectra are needed to clarify their gravity classes. These include the red L dwarf PSO J068.3126+52.4546 (Hya12), identified by Lodieu et al. (2014) as a candidate member of the Hyades. We identify a further 6 objects whose spectra have clear visual suggestions of young age but no index classification due to low S/N or spectral types outside the applicable range of the indices. We conclude that our candidate selection criteria, designed to identify field L/T transition dwarfs, also favored the discovery of young M and L dwarfs because of their redder $y_{P1} - W1$ and $W1 - W2$ colors.

Thirty-one of our discoveries are candidate binaries based on their low-resolution spectral features, making them prime targets for high-resolution imaging. Two of the candidate binaries are common proper motion companions to main sequence stars: PSO J003.4950–18.2802 (previously identified by Baron et al. 2015) and PSO J330.3214+32.3686. If confirmed as binaries, these objects would be ultracool binaries with ages and metallicities determined from their primaries, making them rare empirical test cases for evolutionary models.

We also identify 11 kinematic candidates for nearby young moving groups with spectral types

L7–T4.5 using the BANYAN II online tool, including three that show possible spectral indications of youth. Eight of these have spectral types L9 or later, and if confirmed as YMG members they would provide an unprecedented opportunity to determine the effective temperatures and test evolutionary models of young L/T transition objects.

In conclusion, our discoveries include a large new set of L/T transition dwarfs that contribute significantly to the nearby census and shed light on the evolution of brown dwarf atmospheres in the L/T transition. They also include young late-M and L dwarfs, several of which are candidate very low mass brown dwarfs in nearby star-forming regions and young moving groups. If confirmed, these would be exceptional age-constrained benchmarks for understanding the properties of young cool atmospheres.

We thank the anonymous referee for a prompt and positive report. We thank Katelyn Allers, Michael Kotson, Brian Cabreira, Bill Golisch, Dave Griep, and Eric Volqardsen for assisting with IRTF observations. The Pan-STARRS1 Surveys (PS1) have been made possible through contributions of the Institute for Astronomy, the University of Hawaii, the Pan-STARRS Project Office, the Max-Planck Society and its participating institutes, the Max Planck Institute for Astronomy, Heidelberg and the Max Planck Institute for Extraterrestrial Physics, Garching, The Johns Hopkins University, Durham University, the University of Edinburgh, Queen’s University Belfast, the Harvard-Smithsonian Center for Astrophysics, the Las Cumbres Observatory Global Telescope Network Incorporated, the National Central University of Taiwan, the Space Telescope Science Institute, the National Aeronautics and Space Administration under Grant No. NNX08AR22G issued through the Planetary Science Division of the NASA Science Mission Directorate, the National Science Foundation under Grant No. AST-1238877, the University of Maryland, Eotvos Lorand University (ELTE), and the Los Alamos National Laboratory. The United Kingdom Infrared Telescope (UKIRT) is supported by NASA and operated under an agreement among the University of Hawaii, the University of Arizona, and Lockheed Martin Advanced Technology Center; operations are enabled through the cooperation of the East Asian Observatory. When the data reported here were acquired, UKIRT was operated by the Joint Astronomy Centre on behalf of the Science and Technology Facilities Council of the U.K. This paper makes use of observations processed by the Cambridge Astronomy Survey Unit (CASU) at the Institute of Astronomy, University of Cambridge. This project makes use of data products from the Wide-field Infrared Survey Explorer, which is a joint project of the University of California, Los Angeles, and the Jet Propulsion Laboratory/California Institute of Technology, funded by the National Aeronautics and Space Administration. This research has made use of the 2MASS data products; the UKIDSS data products; the VISTA data products; NASA’s Astrophysical Data System; the SIMBAD database operated at CDS, Strasbourg, France, the SpeX Prism Spectral Libraries, maintained by Adam Burgasser at <http://pono.ucsd.edu/~adam/browndwarfs/spexprism>, and the Database of Ultracool Parallaxes, maintained by Trent Dupuy at <https://www.cfa.harvard.edu/~tdupuy/plx>. WMJB received support from NSF grant AST09-09222. WMBJ, MCL, and EAM received support from NSF grant AST-1313455. Finally, the authors wish to recognize and acknowledge the very significant cultural

role and reverence that the summit of Mauna Kea has always held within the indigenous Hawaiian community. We are most fortunate to have the opportunity to conduct observations from this mountain.

Facilities: IRTF (SpeX), PS1, UKIRT (WFCAM)

REFERENCES

- Aberasturi, M., Solano, E., & Martin, E. L. 2011, *A&A*, 534, L7
- Ackerman, A. S., & Marley, M. S. 2001, *ApJ*, 556, 872
- Allard, F., Hauschildt, P. H., Alexander, D. R., Tamanai, A., & Schweitzer, A. 2001, *ApJ*, 556, 357
- Aller, K. M., Liu, M. C., Magnier, E. A., et al. 2015, *ApJ*, submitted
- Allers, K. N., & Liu, M. C. 2013a, *ApJ*, 772, 79
- . 2013b, *Memorie della Società Astronomica Italiana*, 84, 1089
- Bardalez Gagliuffi, D. C., Burgasser, A. J., Gelino, C. R., et al. 2014, *ApJ*, 794, 143
- Baron, F., Lafreniere, D., Artigau, E., et al. 2015, *ApJ*, 802, 37
- Basri, G., & Reiners, A. 2006, *AJ*, 132, 663
- Bell, C. P. M., Mamajek, E. E., & Naylor, T. 2015, *MNRAS*, 454, 593
- Best, W. M. J., Liu, M. C., Magnier, E. A., et al. 2013, *ApJ*, 777, 84
- Bihain, G., Scholz, R. D., Storm, J., & Schnurr, O. 2013, *A&A*, 557, 43
- Burgasser, A. J. 2007, *ApJ*, 659, 655
- Burgasser, A. J., Cruz, K. L., Cushing, M., et al. 2010, *ApJ*, 710, 1142
- Burgasser, A. J., Geballe, T. R., Leggett, S. K., Kirkpatrick, J. D., & Golimowski, D. A. 2006, *ApJ*, 637, 1067
- Burgasser, A. J., McElwain, M. W., Kirkpatrick, J. D., et al. 2004, *AJ*, 127, 2856
- Burgasser, A. J., Reid, I. N., Leggett, S. K., et al. 2005, *ApJ*, 634, L177
- Burrows, A., Hubbard, W. B., Lunine, J. I., & Liebert, J. 2001, *Rev Mod Phys*, 73, 719
- Burrows, A., Sudarsky, D., & Hubeny, I. 2006, *ApJ*, 640, 1063
- Cardoso, C. V., Burningham, B., Smart, R. L., et al. 2015, *MNRAS*, 450, 2486

- Casali, M., Adamson, A., Alves de Oliveira, C., et al. 2007, *A&A*, 467, 777
- Chiu, K., Fan, X., Leggett, S. K., et al. 2006, *AJ*, 131, 2722
- Cross, N. J. G., Collins, R. S., Mann, R. G., et al. 2012, *A&A*, 548, 119
- Cruz, K. L., Kirkpatrick, J. D., & Burgasser, A. J. 2009, *AJ*, 137, 3345
- Cruz, K. L., Reid, I. N., Liebert, J., Kirkpatrick, J. D., & Lowrance, P. J. 2003, *AJ*, 126, 2421
- Cushing, M. C., Vacca, W. D., & Rayner, J. T. 2004, *PASP*, 116, 362
- Cutri, R. M., Skrutskie, M. F., Van Dyk, S., et al. 2003, *VizieR On-line Data Catalog*, 2246, 0
- Cutri, R. M., Wright, E. L., Conrow, T., et al. 2012, *VizieR On-line Data Catalog*, 2311, 0
- Deacon, N. R., & Hambly, N. C. 2007, *A&A*, 468, 163
- Deacon, N. R., Liu, M. C., Magnier, E. A., et al. 2014, *ApJ*, 792, 119
- Dupuy, T. J., & Liu, M. C. 2012, *ApJS*, 201, 19
- Dupuy, T. J., Liu, M. C., Bowler, B. P., et al. 2010, *ApJ*, 721, 1725
- Dupuy, T. J., Liu, M. C., & Ireland, M. J. 2009, *ApJ*, 699, 168
- . 2014, *ApJ*, 790, 133
- Dupuy, T. J., Liu, M. C., & Leggett, S. K. 2015a, *ApJ*, 803, 102
- Dupuy, T. J., Liu, M. C., Leggett, S. K., et al. 2015b, *ApJ*, 805, 56
- Faherty, J. K., Burgasser, A. J., Cruz, K. L., et al. 2009, *AJ*, 137, 1
- Gagné, J., Burgasser, A. J., Faherty, J. K., et al. 2015a, *ApJL*, 808, L20
- Gagné, J., Lafreniere, D., Doyon, R., Malo, L., & Artigau, E. 2014, *ApJ*, 783, 121
- . 2015b, *ApJ*, 798, 73
- Gagné, J., Faherty, J. K., Cruz, K. L., et al. 2015c, *ApJS*, 219, 33
- Geballe, T. R., Knapp, G. R., Leggett, S. K., et al. 2002, *ApJ*, 564, 466
- Gizis, J. E., Faherty, J. K., Liu, M. C., et al. 2012, *AJ*, 144, 94
- Golimowski, D. A., Leggett, S. K., Marley, M. S., et al. 2004, *AJ*, 127, 3516
- Hodgkin, S. T., Irwin, M. J., Hewett, P. C., & Warren, S. J. 2009, *MNRAS*, 394, 675
- Høg, E., Fabricius, C., Makarov, V. V., et al. 2000, *A&A*, 355, L27

- Hogan, E., Jameson, R. F., Casewell, S. L., Osbourne, S. L., & Hambly, N. C. 2008, *MNRAS*, 388, 495
- Irwin, M. J., Lewis, J., Hodgkin, S., et al. 2004, *Proc. SPIE*, 5493, 411
- Kaiser, N., Burgett, W., Chambers, K., et al. 2010, *Proc. SPIE*, 7733, 12
- Kirkpatrick, J. D., Reid, I. N., Liebert, J., et al. 1999, *ApJ*, 519, 802
- . 2000, *AJ*, 120, 447
- Kirkpatrick, J. D., Looper, D. L., Burgasser, A. J., et al. 2010, *ApJS*, 190, 100
- Kirkpatrick, J. D., Cushing, M. C., Gelino, C. R., et al. 2011, *ApJS*, 197, 19
- Knapp, G. R., Leggett, S. K., Fan, X., et al. 2004, *AJ*, 127, 3553
- Konopacky, Q. M., Ghez, A. M., Barman, T. S., et al. 2010, *ApJ*, 711, 1087
- Lawrence, A., Warren, S. J., Almaini, O., et al. 2007, *MNRAS*, 379, 1599
- . 2013, *VizieR On-line Data Catalog*, 2319, 0
- Lépine, S. 2005, *AJ*, 130, 1680
- Lépine, S., & Bongiorno, B. 2007, *AJ*, 133, 889
- Lépine, S., & Gaidos, E. 2011, *AJ*, 142, 138
- Lépine, S., & Shara, M. M. 2005, *AJ*, 129, 1483
- Limoges, M. M., Lépine, S., & Bergeron, P. 2013, *AJ*, 145, 136
- Liu, M. C., Dupuy, T. J., & Ireland, M. J. 2008, *ApJ*, 689, 436
- Liu, M. C., Dupuy, T. J., & Leggett, S. K. 2010, *ApJ*, 722, 311
- Liu, M. C., Leggett, S. K., Golimowski, D. A., et al. 2006, *ApJ*, 647, 1393
- Liu, M. C., Magnier, E. A., Deacon, N. R., et al. 2013, *ApJL*, 777, L20
- Lodieu, N., Boudreault, S., & Béjar, V. J. S. 2014, *MNRAS*, 445, 3908
- Luhman, K. L., & Sheppard, S. S. 2014, *ApJ*, 787, 126
- Mace, G. N., Kirkpatrick, J. D., Cushing, M. C., et al. 2013, *ApJS*, 205, 6
- Magnier, E. 2006, in *The Advanced Maui Optical and Space Surveillance Technologies Conference*, ed. S. Ryan, Red Hook, NY: Curran Associates, 455

- Magnier, E. 2007, in ASP Conf. Ser., 364, The Future of Photometric, Spectrophotometric and Polarimetric Standardization, ed. C. Sterken, San Francisco, CA, 153
- Magnier, E. A., Liu, M., Monet, D. G., & Chambers, K. C. 2008, in IAU Symp. 248, A Giant Step: From Milli- to Micro-arcsecond Astrometry, ed. W. J. Jin, I. Platais, & M. A. C. Perryman, Cambridge: Cambridge Univ. Press, 553–559
- Makarov, V. V., & Urban, S. 2000, MNRAS, 317, 289
- Malo, L., Doyon, R., Lafreniere, D., et al. 2013, ApJ, 762, 88
- Marley, M. S., Saumon, D., & Goldblatt, C. 2010, ApJL, 723, L117
- Marocco, F., Jones, H. R. A., Day-Jones, A. C., et al. 2015, MNRAS, 449, 3651
- Naud, M.-E., Artigau, E., Malo, L., et al. 2014, ApJ, 787, 5
- Radigan, J., Lafreniere, D., Jayawardhana, R., & Artigau, E. 2014, ApJ, 793, 75
- Rayner, J. T., Cushing, M. C., & Vacca, W. D. 2009, ApJS, 185, 289
- Rayner, J. T., Toomey, D. W., Onaka, P. M., et al. 2003, PASP, 115, 362
- Reid, I. N., Cruz, K. L., Kirkpatrick, J. D., et al. 2008, AJ, 136, 1290
- Reid, I. N., Lewitus, E., Allen, P. R., Cruz, K. L., & Burgasser, A. J. 2006, AJ, 132, 891
- Salim, S., & Gould, A. 2003, ApJ, 582, 1011
- Saumon, D., & Marley, M. S. 2008, ApJ, 689, 1327
- Schmidt, S. J., West, A. A., Hawley, S. L., & Pineda, J. S. 2010, AJ, 139, 1808
- Scholz, R. D., Bihain, G., Schnurr, O., & Storm, J. 2011, A&A, 532, L5
- Shkolnik, E. L., Anglada-Escudé, G., Liu, M. C., et al. 2012, ApJ, 758, 56
- Simons, D. A., & Tokunaga, A. T. 2002, PASP, 114, 169
- Skrutskie, M. F., Cutri, R. M., Stiening, R., et al. 2006, AJ, 131, 1163
- Stephens, D. C., Leggett, S. K., Cushing, M. C., et al. 2009, ApJ, 702, 154
- Thompson, M. A., Kirkpatrick, J. D., Mace, G. N., et al. 2013, PASP, 125, 809
- Tokunaga, A. T., Simons, D. A., & Vacca, W. D. 2002, PASP, 114, 180
- Tonry, J. L., Stubbs, C. W., Lykke, K. R., et al. 2012, ApJ, 750, 99

- Torres, C. A. O., Quast, G. R., Melo, C. H. F., & Sterzik, M. F. 2008, in *Handbook of Star Forming Regions, Volume II, The Southern Sky*, ed. B. Reipurth (San Francisco: ASP), 757
- Tsuji, T. 2005, *ApJ*, 621, 1033
- Vacca, W. D., Cushing, M. C., & Rayner, J. T. 2003, *PASP*, 115, 389
- Wielen, R. 1977, *A&A*, 60, 263
- Wright, E. L., Eisenhardt, P. R. M., Mainzer, A. K., et al. 2010, *AJ*, 140, 1868
- York, D. G., Adelman, J., Anderson, J. E. J., et al. 2000, *AJ*, 120, 1579
- Zhang, Z. H., Pokorny, R. S., Jones, H. R. A., et al. 2009, *A&A*, 497, 619
- Zhang, Z. H., Pinfield, D. J., Day-Jones, A. C., et al. 2010, *MNRAS*, 404, 1817
- Zuckerman, B., & Song, I. 2004, *ARAA*, 42, 685
- Zuckerman, B., Song, I., & Bessell, M. S. 2004, *ApJ*, 613, L65
- Zuckerman, B., Song, I., Bessell, M. S., & Webb, R. A. 2001, *ApJ*, 562, L87

Table 1. Pan-STARRS1 and *WISE* All-sky Photometry

Pan-STARRS1 Name	z_{P1} (mag)	y_{P1} (mag)	<i>WISE</i> Name	W1 (mag)	W2 (mag)	W3 (mag)
PSO J003.4950–18.2802	20.08 ± 0.04	18.94 ± 0.07	J001358.81–181648.1	14.60 ± 0.04	14.17 ± 0.05	12.20 ± 0.35
PSO J004.1834+23.0741	20.27 ± 0.06	18.90 ± 0.03	J001643.96+230426.7	14.29 ± 0.03	13.65 ± 0.04	12.20 ± 0.35
PSO J004.7148+51.8918	20.06 ± 0.06	19.08 ± 0.07	J001851.51+515330.6	13.58 ± 0.04	13.04 ± 0.04	12.55 ± 0.34
PSO J007.7921+57.8267	18.18 ± 0.01	17.02 ± 0.01	J003110.04+574936.3	12.41 ± 0.02	11.84 ± 0.02	11.30 ± 0.10
PSO J007.9194+33.5961	19.62 ± 0.03	18.60 ± 0.02	J003140.64+333545.9	13.69 ± 0.03	13.18 ± 0.03	12.03 ± 0.23
PSO J010.2132+41.6091	19.99 ± 0.06	19.37 ± 0.04	J004051.14+413631.4	16.11 ± 0.07	15.31 ± 0.09	>12.97
PSO J023.8557+02.0884	19.62 ± 0.02	18.76 ± 0.02	J013525.37+020518.4	14.31 ± 0.03	13.90 ± 0.05	>12.04
PSO J024.1519+37.6443	20.46 ± 0.11	19.84 ± 0.08	J013636.31+373840.6	16.80 ± 0.09	14.76 ± 0.06	>12.72
PSO J031.5651+20.9097	20.99 ± 0.23	19.61 ± 0.05	J020615.62+205435.3	16.60 ± 0.09	14.70 ± 0.06	12.28 ± 0.34
PSO J041.5426+01.9456	20.10 ± 0.02	19.06 ± 0.03	J024610.23+015644.4	14.28 ± 0.03	13.65 ± 0.04	11.75 ± 0.25
PSO J048.9806+07.5414	20.11 ± 0.04	19.03 ± 0.05	J031555.29+073229.6	14.63 ± 0.04	14.14 ± 0.05	12.47 ± 0.50
PSO J049.1124+17.0885	20.24 ± 0.03	19.17 ± 0.04	J031626.95+170518.5	15.23 ± 0.05	14.63 ± 0.08	12.14 ± 0.35
PSO J049.1159+26.8409	20.09 ± 0.03	18.65 ± 0.02	J031627.78+265027.6	15.08 ± 0.05	13.97 ± 0.05	>12.47
PSO J052.7214–03.8409	19.78 ± 0.04	18.58 ± 0.02	J033053.14–035027.3	13.65 ± 0.03	12.93 ± 0.03	12.07 ± 0.30
PSO J053.3683+30.9663	18.64 ± 0.02	17.67 ± 0.02	J033328.27+305759.4	11.98 ± 0.03	11.48 ± 0.03	12.22 ± 0.42
PSO J054.8149–11.7792	19.98 ± 0.03	18.99 ± 0.06	J033915.57–114645.0	14.44 ± 0.03	13.98 ± 0.04	>12.81
PSO J055.0493–21.1704	20.59 ± 0.06	19.20 ± 0.04	J034011.81–211013.2	15.53 ± 0.05	14.50 ± 0.06	>12.50
PSO J057.2893+15.2433	20.76 ± 0.06	19.75 ± 0.11	J034909.44+151436.0	13.85 ± 0.03	13.21 ± 0.03	>12.07
PSO J060.3200+25.9645	20.05 ± 0.02	19.09 ± 0.03	J040116.80+255752.2	15.05 ± 0.04	14.36 ± 0.07	>12.39
PSO J068.3126+52.4546	20.50 ± 0.04	19.20 ± 0.04	J043315.02+522716.7	13.98 ± 0.03	13.01 ± 0.04	>11.71
PSO J068.9292+13.3958	20.22 ± 0.06	19.12 ± 0.03	J043542.99+132344.9	14.25 ± 0.03	13.74 ± 0.06	>11.88
PSO J070.3773+04.7333	20.69 ± 0.10	19.04 ± 0.04	J044130.52+044359.9	15.74 ± 0.07	14.40 ± 0.09	>12.35
PSO J071.4708+36.4930	19.94 ± 0.03	18.99 ± 0.03	J044552.98+362935.0	14.24 ± 0.03	13.83 ± 0.05	>12.51
PSO J071.6394–24.4991	19.51 ± 0.02	18.48 ± 0.03	J044633.45–242956.8	14.27 ± 0.03	13.77 ± 0.04	12.42 ± 0.33
PSO J071.8769–12.2713	20.37 ± 0.04	18.85 ± 0.04	J044730.40–121616.4	14.96 ± 0.03	14.24 ± 0.04	12.61 ± 0.42
PSO J076.1314+25.1940	20.72 ± 0.05	19.62 ± 0.08	J050431.53+251138.5	13.86 ± 0.03	13.42 ± 0.04	11.69 ± 0.24
PSO J076.7092+52.6087	20.00 ± 0.03	18.25 ± 0.02	J050650.20+523631.2	14.94 ± 0.04	13.73 ± 0.05	12.27 ± 0.36
PSO J077.1034+24.3810	20.21 ± 0.04	19.19 ± 0.06	J050824.82+242251.1	15.30 ± 0.06	14.51 ± 0.08	12.37 ± 0.47
PSO J078.9904+31.0171	19.76 ± 0.02	18.74 ± 0.03	J051557.68+310101.8	14.88 ± 0.04	14.25 ± 0.08	>12.26
PSO J085.3474+36.3037	19.99 ± 0.07	18.75 ± 0.03	J054123.39+361813.1	12.77 ± 0.03	12.17 ± 0.03	9.94 ± 0.06
PSO J087.7749–12.6537	19.71 ± 0.02	18.76 ± 0.03	J055105.96–123913.5	13.87 ± 0.03	13.40 ± 0.04	>11.98
PSO J088.0452+43.2123	19.69 ± 0.03	18.67 ± 0.02	J055210.83+431244.2	14.26 ± 0.03	13.82 ± 0.04	>12.07
PSO J088.3324–24.4439	19.83 ± 0.03	18.86 ± 0.03	J055319.77–242638.0	15.61 ± 0.05	15.06 ± 0.09	>12.96
PSO J100.5233+41.0320	19.74 ± 0.03	18.63 ± 0.02	J064205.58+410155.5	13.36 ± 0.03	12.55 ± 0.03	11.70 ± 0.31
PSO J101.8428+39.7462	19.71 ± 0.02	18.71 ± 0.03	J064722.28+394446.3	15.30 ± 0.05	14.65 ± 0.08	>12.23
PSO J103.0927+41.4601	18.88 ± 0.02	17.64 ± 0.01	J065222.24+412736.1	13.13 ± 0.02	12.44 ± 0.03	11.80 ± 0.25
PSO J105.4992+63.3581	19.47 ± 0.03	17.99 ± 0.01	J070159.79+632129.2	14.20 ± 0.03	13.22 ± 0.03	12.48 ± 0.42
PSO J108.4590+38.2086	20.15 ± 0.03	19.08 ± 0.04	J071350.14+381230.6	13.98 ± 0.03	13.51 ± 0.04	>12.69
PSO J109.4864+46.5278	20.65 ± 0.06	19.20 ± 0.06	J071756.71+463140.3	15.40 ± 0.05	14.77 ± 0.08	>12.54
PSO J115.0659+59.0473	19.62 ± 0.02	18.67 ± 0.02	J074015.81+590250.2	15.31 ± 0.04	14.90 ± 0.09	>12.78
PSO J117.1608+17.7259	19.38 ± 0.03	18.43 ± 0.02	J074838.58+174333.0	13.74 ± 0.03	13.32 ± 0.03	>12.55
PSO J127.4696+10.5777	20.23 ± 0.04	19.42 ± 0.04	J082952.73+103440.4	14.35 ± 0.03	13.70 ± 0.05	11.27 ± 0.24
PSO J133.8016–02.5658	19.53 ± 0.03	18.34 ± 0.01	J085512.39–023356.8	14.17 ± 0.03	13.57 ± 0.04	>12.69
PSO J133.8302+06.0160	19.11 ± 0.02	18.34 ± 0.02	J085519.22+060057.6	14.77 ± 0.04	14.24 ± 0.06	>11.87
PSO J135.0395+32.0845	18.78 ± 0.02	17.76 ± 0.02	J090009.49+320504.2	13.96 ± 0.03	13.44 ± 0.04	>11.97
PSO J135.7840+16.9932	19.87 ± 0.02	18.73 ± 0.04	J090308.17+165935.4	14.53 ± 0.04	13.99 ± 0.05	>12.35
PSO J136.3401+10.1151	20.53 ± 0.06	19.30 ± 0.04	J090521.62+100654.7	15.19 ± 0.05	14.32 ± 0.07	>12.40
PSO J136.5494–06.1944	17.89 ± 0.00	16.82 ± 0.01	J090611.85–061139.9	13.25 ± 0.03	12.82 ± 0.03	12.21 ± 0.37
PSO J140.2308+45.6487	18.49 ± 0.02	17.24 ± 0.01	J092055.40+453856.3	13.06 ± 0.02	12.39 ± 0.03	11.28 ± 0.17
PSO J143.6774–29.8356	19.33 ± 0.03	18.38 ± 0.02	J093442.54–295007.7	14.95 ± 0.04	14.47 ± 0.05	12.57 ± 0.39
PSO J146.0144+05.1319	19.67 ± 0.02	18.75 ± 0.03	J094403.46+050755.2	15.07 ± 0.04	14.57 ± 0.08	>12.63
PSO J147.5092–27.6337	19.98 ± 0.04	18.91 ± 0.03	J095002.19–273801.3	15.48 ± 0.05	15.03 ± 0.09	>12.63
PSO J149.0341–14.7857	19.51 ± 0.02	18.36 ± 0.02	J095608.17–144708.2	13.52 ± 0.03	12.77 ± 0.03	11.14 ± 0.19
PSO J149.1907–19.1730	18.48 ± 0.01	17.37 ± 0.01	J095645.75–191022.3	13.31 ± 0.03	12.91 ± 0.03	11.87 ± 0.26
PSO J152.2977+15.9912	19.59 ± 0.03	18.61 ± 0.04	J100911.47+155928.4	15.05 ± 0.04	14.60 ± 0.08	>12.10
PSO J158.1597+05.2231	19.61 ± 0.05	18.75 ± 0.04	J103238.32+051323.2	14.85 ± 0.04	14.45 ± 0.08	>12.32
PSO J159.0433–27.6357	18.99 ± 0.03	18.04 ± 0.02	J103610.38–273808.3	14.46 ± 0.03	14.02 ± 0.04	12.52 ± 0.38
PSO J159.2399–26.3885	20.44 ± 0.10	19.04 ± 0.05	J103657.59–262319.0	14.69 ± 0.03	13.98 ± 0.05	>12.88
PSO J160.0416–21.3281	20.35 ± 0.04	19.03 ± 0.03	J104010.00–211940.9	15.05 ± 0.04	14.18 ± 0.05	>12.63
PSO J167.1132+08.6331	19.74 ± 0.02	18.74 ± 0.03	J110827.18+083759.5	14.13 ± 0.03	13.66 ± 0.04	>12.62
PSO J168.1800–27.2264	...	19.16 ± 0.14	J111243.25–271336.1	15.76 ± 0.06	14.92 ± 0.09	12.57 ± 0.42
PSO J174.6630–18.6530	19.04 ± 0.02	18.20 ± 0.02	J113839.14–183910.8	14.86 ± 0.04	14.40 ± 0.07	>12.48
PSO J175.2003+16.1403	20.41 ± 0.07	18.94 ± 0.03	J114048.05+160825.1	14.63 ± 0.03	14.22 ± 0.05	>12.29
PSO J175.8169–20.4072	20.52 ± 0.07	19.23 ± 0.04	J114316.04–202425.7	15.67 ± 0.06	14.42 ± 0.07	12.20 ± 0.43
PSO J180.1475–28.6160	19.73 ± 0.06	18.21 ± 0.02	J120035.41–283657.6	14.24 ± 0.03	13.56 ± 0.04	>12.40
PSO J182.6569–26.6197	19.62 ± 0.03	18.66 ± 0.03	J121037.66–263710.6	14.93 ± 0.04	14.44 ± 0.06	>12.30

Table 1—Continued

Pan-STARRS1 Name	z_{P1} (mag)	y_{P1} (mag)	WISE Name	W1 (mag)	W2 (mag)	W3 (mag)
PSO J183.4547+40.7901	21.17 ± 0.18	19.79 ± 0.07	J121349.14+404724.6	16.72 ± 0.12	15.02 ± 0.09	12.56 ± 0.39
PSO J183.9318−09.7914	19.45 ± 0.02	18.51 ± 0.02	J121543.62−094729.1	14.45 ± 0.03	14.04 ± 0.05	>12.60
PSO J186.5342+21.8364	19.71 ± 0.04	18.94 ± 0.09	J122608.20+215010.8	15.57 ± 0.05	15.05 ± 0.09	12.76 ± 0.52
PSO J192.5647+26.4796	...	19.60 ± 0.12	J125015.56+262846.9	16.36 ± 0.09	14.58 ± 0.06	>12.84
PSO J192.6717−21.8250	20.68 ± 0.09	19.09 ± 0.05	J125041.21−214930.1	15.75 ± 0.05	14.76 ± 0.06	>12.66
PSO J202.1635−03.7660	21.43 ± 0.15	19.58 ± 0.04	J132839.25−034558.2	15.74 ± 0.05	14.45 ± 0.05	>12.82
PSO J202.5764−26.1469	...	18.70 ± 0.12	J133018.38−260848.4	15.65 ± 0.05	15.21 ± 0.10	>12.89
PSO J207.7496+29.4240	20.81 ± 0.06	19.79 ± 0.13	J135059.90+292526.7	14.43 ± 0.03	13.76 ± 0.04	12.96 ± 0.48
PSO J218.4532+50.7231	20.68 ± 0.13	19.40 ± 0.04	J143348.76+504322.8	15.88 ± 0.05	14.70 ± 0.05	>13.05
PSO J218.5616−27.8952	19.75 ± 0.03	18.76 ± 0.04	J143414.79−275342.6	14.07 ± 0.03	13.56 ± 0.04	>12.05
PSO J224.3820+47.4057	...	19.72 ± 0.13	J145731.67+472420.1	16.72 ± 0.08	14.62 ± 0.05	12.66 ± 0.28
PSO J228.6775−29.7088	19.85 ± 0.05	18.77 ± 0.03	J151442.58−294231.9	14.95 ± 0.04	14.29 ± 0.06	>12.53
PSO J229.2354−26.6738	20.30 ± 0.09	19.01 ± 0.03	J151656.50−264025.3	14.80 ± 0.04	14.39 ± 0.07	>12.59
PSO J231.2588+08.5622	20.96 ± 0.05	19.49 ± 0.05	J152502.10+083343.8	15.29 ± 0.04	14.55 ± 0.05	>12.70
PSO J231.7900−26.4494	19.18 ± 0.03	18.09 ± 0.02	J152709.58−262657.7	14.25 ± 0.03	13.85 ± 0.05	>12.48
PSO J231.8943−29.0599	18.75 ± 0.02	17.81 ± 0.01	J152734.62−290335.7	13.87 ± 0.03	13.43 ± 0.04	11.32 ± 0.15
PSO J237.1471−23.1489	17.39 ± 0.01	16.62 ± 0.01	J154835.30−230855.4	12.94 ± 0.03	12.40 ± 0.03	10.66 ± 0.11
PSO J239.7016−23.2664	19.28 ± 0.02	18.28 ± 0.03	J155848.37−231559.1	14.44 ± 0.04	13.86 ± 0.05	>12.38
PSO J241.1376+39.0369	20.91 ± 0.09	19.74 ± 0.15	J160432.99+390212.9	16.11 ± 0.05	15.15 ± 0.06	>12.99
PSO J242.9129+02.4856	20.61 ± 0.04	19.52 ± 0.08	J161139.11+022908.1	15.48 ± 0.05	14.57 ± 0.07	>12.12
PSO J244.1180+06.3598	20.93 ± 0.07	19.77 ± 0.07	J161628.34+062135.2	14.78 ± 0.04	14.09 ± 0.05	>12.36
PSO J244.6801+08.7185	21.14 ± 0.20	19.56 ± 0.05	J161843.22+084306.9	16.53 ± 0.10	14.90 ± 0.08	>12.53
PSO J249.4774−10.8754	18.64 ± 0.02	18.25 ± 0.02	J163754.58−105231.6	13.81 ± 0.04	13.39 ± 0.08	10.91 ± 0.16
PSO J255.6623+10.7542	20.57 ± 0.07	19.96 ± 0.10	J170238.96+104515.2	14.64 ± 0.03	13.57 ± 0.04	11.13 ± 0.12
PSO J258.2413+06.7612	19.73 ± 0.02	18.50 ± 0.02	J171257.92+064540.3	13.88 ± 0.03	13.39 ± 0.03	>12.04
PSO J260.1623+61.7636	21.10 ± 0.09	19.66 ± 0.11	J172038.99+614548.9	16.23 ± 0.04	15.31 ± 0.05	>14.07
PSO J260.3363+46.6739	19.99 ± 0.03	18.79 ± 0.09	J172120.70+464026.1	14.45 ± 0.03	13.94 ± 0.04	12.72 ± 0.32
PSO J261.2881+22.9269	21.42 ± 0.20	19.64 ± 0.08	J172509.16+225536.8	16.57 ± 0.10	15.11 ± 0.09	>12.64
PSO J263.5879+50.3975	20.59 ± 0.08	18.89 ± 0.03	J173421.02+502349.9	15.41 ± 0.03	14.34 ± 0.04	>13.48
PSO J265.0759+11.4855	20.82 ± 0.09	19.73 ± 0.18	J174018.21+112907.5	15.57 ± 0.05	14.96 ± 0.08	>12.84
PSO J268.7928+18.0557	19.68 ± 0.06	18.15 ± 0.02	J175510.28+180320.2	14.60 ± 0.03	13.73 ± 0.04	12.36 ± 0.31
PSO J272.0887−04.9943	20.87 ± 0.10	19.51 ± 0.07	J180821.29−045940.1	14.99 ± 0.05	14.15 ± 0.07	12.37 ± 0.43
PSO J272.4689−04.8036	18.79 ± 0.03	17.46 ± 0.01	J180952.53−044812.5	13.29 ± 0.03	12.73 ± 0.03	12.38 ± 0.47
PSO J274.0908+30.5470	21.12 ± 0.18	19.79 ± 0.07	J181621.86+303248.9	16.55 ± 0.09	15.01 ± 0.08	>13.04
PSO J276.0671−01.9863	20.50 ± 0.04	19.77 ± 0.08	J182416.10−015910.8	14.20 ± 0.04	13.37 ± 0.05	>11.85
PSO J276.8234+22.4380	19.91 ± 0.04	18.86 ± 0.02	J182717.60+222616.9	14.01 ± 0.04	13.43 ± 0.04	>12.09
PSO J277.7441+45.7160	20.55 ± 0.06	19.34 ± 0.10	J183058.56+454257.4	14.81 ± 0.03	14.17 ± 0.04	>13.17
PSO J280.2973+63.2600	19.66 ± 0.02	18.56 ± 0.04	J184111.36+631535.6	14.13 ± 0.03	13.49 ± 0.03	12.39 ± 0.15
PSO J282.5878+34.7691	20.14 ± 0.08	19.32 ± 0.07	J185021.04+344609.7	15.13 ± 0.04	14.73 ± 0.06	>13.12
PSO J282.7576+59.5858	18.35 ± 0.01	17.15 ± 0.01	J185101.83+593508.6	12.65 ± 0.02	12.18 ± 0.02	11.23 ± 0.07
PSO J284.7214+39.3189	21.45 ± 0.21	19.90 ± 0.06	J185853.08+391908.0	16.59 ± 0.08	15.40 ± 0.09	>13.24
PSO J289.8149+30.7664	19.10 ± 0.04	17.74 ± 0.02	J191915.54+304558.4	13.39 ± 0.03	12.94 ± 0.03	11.72 ± 0.19
PSO J291.2688+68.5310	20.16 ± 0.05	18.65 ± 0.05	J192504.54+683151.7	15.10 ± 0.03	14.45 ± 0.04	13.65 ± 0.53
PSO J296.0820+35.7035	19.74 ± 0.11	19.07 ± 0.04	J194419.69+354212.5	14.67 ± 0.04	14.24 ± 0.06	12.01 ± 0.20
PSO J303.7105+31.9331	20.12 ± 0.08	19.68 ± 0.12	J201450.36+315600.2	13.49 ± 0.03	11.41 ± 0.02	10.46 ± 0.24
PSO J304.7573−07.2350	19.59 ± 0.03	18.70 ± 0.04	J201901.74−071405.3	15.40 ± 0.05	14.81 ± 0.09	>12.54
PSO J307.6784+07.8263	17.99 ± 0.01	16.46 ± 0.01	J203042.79+074934.7	12.96 ± 0.03	12.12 ± 0.03	10.96 ± 0.11
PSO J308.9834−09.7312	20.94 ± 0.10	19.76 ± 0.13	J203556.02−094352.3	15.94 ± 0.08	14.82 ± 0.09	>12.35
PSO J310.9853+62.3470	19.29 ± 0.04	17.92 ± 0.02	J204356.42+622048.9	13.90 ± 0.03	13.02 ± 0.03	12.12 ± 0.22
PSO J313.1577−26.0050	20.36 ± 0.05	19.18 ± 0.05	J205237.87−260018.0	15.61 ± 0.06	14.98 ± 0.11	12.60 ± 0.53
PSO J316.5156+04.1173	20.13 ± 0.06	19.14 ± 0.05	J210603.72+040702.4	14.87 ± 0.04	14.45 ± 0.07	>12.01
PSO J319.3102−29.6682	18.90 ± 0.02	17.66 ± 0.02	J211714.44−294005.2	13.56 ± 0.03	12.82 ± 0.03	11.94 ± 0.32
PSO J321.1619+18.8243	20.50 ± 0.05	19.41 ± 0.07	J212438.82+184927.5	14.73 ± 0.04	14.04 ± 0.05	12.45 ± 0.37
PSO J329.8288+03.0840	20.52 ± 0.20	19.25 ± 0.10	J215918.90+030502.8	14.89 ± 0.04	14.29 ± 0.06	>12.56
PSO J330.3214+32.3686	19.90 ± 0.03	18.63 ± 0.04	J220117.10+322206.9	14.71 ± 0.03	13.63 ± 0.04	12.29 ± 0.29
PSO J331.6058+33.0207	20.30 ± 0.06	18.93 ± 0.04	J220625.35+330114.6	15.37 ± 0.04	14.62 ± 0.07	12.82 ± 0.48
PSO J331.9397−07.0570	20.71 ± 0.09	19.77 ± 0.07	J220745.53−070325.1	14.51 ± 0.03	13.86 ± 0.05	>12.18
PSO J334.1193+19.8800	20.79 ± 0.06	19.18 ± 0.07	J221628.62+195248.1	15.70 ± 0.04	14.64 ± 0.06	12.93 ± 0.44
PSO J334.8034+11.2278	19.95 ± 0.03	18.92 ± 0.05	J221912.81+111340.1	14.11 ± 0.03	13.69 ± 0.04	12.68 ± 0.46
PSO J336.9036−18.9148	20.71 ± 0.07	19.81 ± 0.08	J222736.87−185453.1	14.15 ± 0.03	13.61 ± 0.04	>12.70
PSO J337.4314+16.4215	19.91 ± 0.03	18.91 ± 0.02	J222943.60+162516.5	15.72 ± 0.05	15.16 ± 0.10	>12.69
PSO J338.8587+31.4729	20.13 ± 0.04	19.14 ± 0.05	J223526.08+312822.3	15.06 ± 0.04	14.66 ± 0.07	>12.62
PSO J339.0734+51.0978	19.15 ± 0.06	17.27 ± 0.01	J223617.59+510551.9	13.84 ± 0.03	12.48 ± 0.03	11.02 ± 0.08
PSO J341.7509−15.1075	19.72 ± 0.03	18.73 ± 0.03	J224700.20−150626.8	14.22 ± 0.03	13.80 ± 0.04	>12.75
PSO J342.3797−16.4665	19.29 ± 0.04	18.27 ± 0.02	J224931.09−162759.4	14.09 ± 0.03	13.67 ± 0.04	>12.08
PSO J342.9795−09.6000	21.22 ± 0.17	20.04 ± 0.14	J225154.99−093600.5	15.98 ± 0.08	15.02 ± 0.11	>12.54

Table 1—Continued

Pan-STARRS1 Name	z_{P1} (mag)	y_{P1} (mag)	<i>WISE</i> Name	<i>W1</i> (mag)	<i>W2</i> (mag)	<i>W3</i> (mag)
PSO J344.8146+20.1917	20.31 ± 0.11	18.99 ± 0.04	J225915.51+201129.9	14.35 ± 0.03	13.93 ± 0.04	>12.33
PSO J346.3203–11.1654	20.37 ± 0.05	19.29 ± 0.05	J230516.86–110955.2	14.62 ± 0.04	14.09 ± 0.06	>12.24
PSO J346.5281–15.9406	20.15 ± 0.08	19.28 ± 0.09	J230606.72–155626.1	13.86 ± 0.03	13.36 ± 0.04	>12.09
PSO J348.8808+06.2873	19.09 ± 0.01	18.06 ± 0.02	J231531.39+061714.2	13.55 ± 0.03	13.10 ± 0.03	11.67 ± 0.23
PSO J350.4673–19.0783	20.02 ± 0.05	19.08 ± 0.05	J232152.15–190441.6	14.57 ± 0.03	14.13 ± 0.06	>12.61
PSO J353.0517–29.8947	20.33 ± 0.05	19.24 ± 0.08	J233212.40–295341.5	15.78 ± 0.06	15.15 ± 0.10	>12.84
PSO J353.6355+13.2209	19.79 ± 0.03	18.88 ± 0.02	J233432.53+131315.3	13.78 ± 0.03	13.26 ± 0.03	12.40 ± 0.39
PSO J353.8627+45.1946	20.13 ± 0.03	19.15 ± 0.07	J233527.07+451140.9	13.48 ± 0.03	12.93 ± 0.03	12.72 ± 0.54
PSO J357.8314+49.6330	20.04 ± 0.04	18.73 ± 0.03	J235119.56+493758.9	14.84 ± 0.03	14.32 ± 0.05	12.55 ± 0.30
PSO J359.8867–01.8651	20.31 ± 0.06	19.06 ± 0.03	J235932.81–015154.1	15.24 ± 0.05	14.54 ± 0.07	>12.64

Note. — Pan-STARRS1 photometry is quoted as of March 2015. The photometric selections described in this paper were done using Pan-STARRS1 photometry from January 2012. *WISE* photometry is from the *WISE* All-sky Release.

Table 2. Near-infrared Photometry

Name	2MASS Photometry			MKO Photometry			Ref. ^a
	$J_{2\text{MASS}}$ (mag)	$H_{2\text{MASS}}$ (mag)	$K_{2\text{MASS}}$ (mag)	J_{MKO} (mag)	H_{MKO} (mag)	K_{MKO} (mag)	
PSO J003.4–18	16.54 ± 0.14	15.89 ± 0.18	15.04 ± 0.13	16.68 ± 0.27	15.87 ± 0.30	$[15.18 \pm 0.28]$	1
PSO J004.1+23	>16.41	15.70 ± 0.14	>14.97	16.58 ± 0.03	15.72 ± 0.02	$[15.24 \pm 0.05]$	1
PSO J004.7+51	16.82 ± 0.15	15.29 ± 0.11	14.64 ± 0.07	16.70 ± 0.05	15.40 ± 0.11	$[14.51 \pm 0.07]$	1
PSO J007.7+57	14.95 ± 0.04	13.78 ± 0.04	13.22 ± 0.03	14.80 ± 0.01	13.86 ± 0.01	$[13.21 \pm 0.03]$	1
PSO J007.9+33	16.45 ± 0.13	15.43 ± 0.12	14.49 ± 0.08	16.40 ± 0.03	$[15.47 \pm 0.08]$	$[14.69 \pm 0.08]$	1
PSO J010.2+41	18.27 ± 0.14	$[17.34 \pm 0.20]$	$[16.78 \pm 0.22]$	1
PSO J023.8+02	16.62 ± 0.13	15.48 ± 0.10	15.12 ± 0.12	16.48 ± 0.15	15.66 ± 0.14	14.99 ± 0.12	2
PSO J024.1+37	18.23 ± 0.11	17.46 ± 0.10	$[17.14 \pm 0.16]$	1
PSO J031.5+20	16.73 ± 0.03	17.02 ± 0.07	$[16.79 \pm 0.31]$	1
PSO J041.5+01	>16.88	15.87 ± 0.16	15.01 ± 0.13	16.91 ± 0.04	15.85 ± 0.04	$[15.10 \pm 0.08]$	1
PSO J048.9+07	17.02 ± 0.21	15.83 ± 0.18	15.43 ± 0.20	16.95 ± 0.04	16.19 ± 0.04	$[15.65 \pm 0.10]$	1
PSO J049.1+17	16.96 ± 0.24	16.39 ± 0.21	15.75 ± 0.24	17.06 ± 0.04	16.43 ± 0.04	$[15.96 \pm 0.11]$	1
PSO J049.1+26	16.59 ± 0.15	15.59 ± 0.16	>15.16	16.11 ± 0.02	15.82 ± 0.02	$[15.50 \pm 0.05]$	1
PSO J052.7–03	16.47 ± 0.10	15.16 ± 0.08	14.72 ± 0.09	16.26 ± 0.02	15.24 ± 0.02	$[14.58 \pm 0.04]$	1
PSO J053.3+30	15.13 ± 0.04	13.70 ± 0.03	12.96 ± 0.03	15.09 ± 0.00	13.75 ± 0.00	12.94 ± 0.00	2
PSO J054.8–11	16.79 ± 0.15	15.83 ± 0.13	15.06 ± 0.14	16.71 ± 0.05	15.75 ± 0.03	$[14.97 \pm 0.10]$	1
PSO J055.0–21	16.95 ± 0.05	16.29 ± 0.05	$[16.12 \pm 0.16]$	1
PSO J057.2+15	17.29 ± 0.22	16.30 ± 0.19	15.01 ± 0.11	17.29 ± 0.06	16.04 ± 0.05	14.90 ± 0.02	1
PSO J060.3+25	16.81 ± 0.17	15.73 ± 0.14	15.36 ± 0.17	16.93 ± 0.04	16.10 ± 0.03	$[15.53 \pm 0.07]$	1
PSO J068.3+52	16.88 ± 0.15	15.41 ± 0.09	14.86 ± 0.11	16.63 ± 0.05	15.65 ± 0.06	14.70 ± 0.01	1
PSO J068.9+13	16.73 ± 0.16	15.77 ± 0.14	14.80 ± 0.12	16.89 ± 0.03	15.80 ± 0.02	14.99 ± 0.01	1
PSO J070.3+04	16.39 ± 0.03	16.46 ± 0.04	$[16.38 \pm 0.22]$	1
PSO J071.4+36	16.83 ± 0.19	15.78 ± 0.17	15.03 ± 0.15	16.72 ± 0.03	15.79 ± 0.02	$[14.94 \pm 0.09]$	1
PSO J071.6–24	16.43 ± 0.12	15.53 ± 0.13	15.14 ± 0.16	16.29 ± 0.02	15.58 ± 0.02	15.13 ± 0.02	1
PSO J071.8–12	16.48 ± 0.11	15.99 ± 0.17	15.55 ± 0.22	16.69 ± 0.04	16.07 ± 0.04	$[15.66 \pm 0.16]$	1
PSO J076.1+25	17.12 ± 0.20	15.27 ± 0.09	14.46 ± 0.08	17.02 ± 0.04	15.38 ± 0.02	14.41 ± 0.02	1
PSO J076.7+52	15.75 ± 0.07	15.35 ± 0.11	15.60 ± 0.20	15.44 ± 0.02	15.47 ± 0.02	15.60 ± 0.03	1
PSO J077.1+24	16.93 ± 0.14	16.47 ± 0.25	15.82 ± 0.22	17.06 ± 0.04	16.31 ± 0.04	15.59 ± 0.03	1
PSO J078.9+31	16.67 ± 0.03	15.96 ± 0.03	15.30 ± 0.03	1
PSO J085.3+36	>15.86	>14.55	14.34 ± 0.07	16.10 ± 0.01	14.70 ± 0.00	13.80 ± 0.00	2
PSO J087.7–12	16.63 ± 0.13	15.69 ± 0.15	14.71 ± 0.13	16.52 ± 0.04	15.52 ± 0.03	$[14.71 \pm 0.08]$	1
PSO J088.0+43	16.37 ± 0.09	15.48 ± 0.08	14.87 ± 0.08	16.29 ± 0.02	15.52 ± 0.02	14.80 ± 0.03	1
PSO J088.3–24	16.84 ± 0.09	16.48 ± 0.12	$[15.62 \pm 0.26]$	1
PSO J100.5+41	16.16 ± 0.10	15.09 ± 0.07	14.28 ± 0.06	16.15 ± 0.02	15.11 ± 0.01	14.31 ± 0.01	1
PSO J101.8+39	16.83 ± 0.03	16.20 ± 0.04	15.61 ± 0.02	1
PSO J103.0+41	15.48 ± 0.06	14.46 ± 0.05	13.89 ± 0.05	15.36 ± 0.01	14.51 ± 0.03	13.95 ± 0.03	1
PSO J105.4+63	15.79 ± 0.06	15.08 ± 0.07	14.88 ± 0.11	$[[15.66 \pm 0.10]]$	$[[15.16 \pm 0.14]]$	$[[14.89 \pm 0.19]]$	1
PSO J108.4+38	16.92 ± 0.15	15.72 ± 0.12	14.92 ± 0.10	16.68 ± 0.03	15.66 ± 0.02	14.84 ± 0.01	1
PSO J109.4+46	17.06 ± 0.04	16.45 ± 0.04	15.86 ± 0.03	1
PSO J115.0+59	16.51 ± 0.16	15.88 ± 0.19	>16.32	16.76 ± 0.04	16.13 ± 0.04	15.56 ± 0.03	1
PSO J117.1+17	16.27 ± 0.11	15.18 ± 0.09	14.42 ± 0.09	16.16 ± 0.02	15.26 ± 0.02	14.50 ± 0.01	1
PSO J127.4+10	17.07 ± 0.03	16.11 ± 0.02	15.25 ± 0.02	1
PSO J133.8–02	16.10 ± 0.07	15.31 ± 0.07	14.96 ± 0.13	16.00 ± 0.02	15.29 ± 0.02	$[14.77 \pm 0.06]$	1
PSO J133.8+06	16.31 ± 0.12	15.43 ± 0.13	15.03 ± 0.12	16.34 ± 0.01	$[15.68 \pm 0.04]$	$[15.19 \pm 0.05]$	2
PSO J135.0+32	15.84 ± 0.07	15.10 ± 0.08	14.50 ± 0.09	15.76 ± 0.02	15.03 ± 0.01	14.41 ± 0.03	1
PSO J135.7+16	16.49 ± 0.11	15.78 ± 0.16	15.49 ± 0.19	16.40 ± 0.02	15.80 ± 0.02	15.26 ± 0.02	1
PSO J136.3+10	17.08 ± 0.02	16.39 ± 0.02	16.07 ± 0.02	2
PSO J136.5–06	14.83 ± 0.04	14.13 ± 0.05	13.66 ± 0.04	14.75 ± 0.02	14.19 ± 0.03	13.70 ± 0.02	1
PSO J140.2+45	15.22 ± 0.05	14.16 ± 0.05	13.73 ± 0.05	15.04 ± 0.01	14.19 ± 0.02	13.77 ± 0.01	1
PSO J143.6–29	16.41 ± 0.11	16.05 ± 0.16	15.21 ± 0.16	16.47 ± 0.03	15.87 ± 0.02	15.33 ± 0.02	1
PSO J146.0+05	16.81 ± 0.16	15.98 ± 0.17	15.63 ± 0.23	16.74 ± 0.02	16.11 ± 0.02	15.55 ± 0.02	2
PSO J147.5–27	16.89 ± 0.18	16.22 ± 0.21	15.46 ± 0.19	$[[16.84 \pm 0.20]]$	$[[16.29 \pm 0.24]]$	$[[15.43 \pm 0.23]]$	1
PSO J149.0–14	16.28 ± 0.10	15.06 ± 0.09	14.22 ± 0.06	15.99 ± 0.02	15.07 ± 0.01	14.46 ± 0.02	1
PSO J149.1–19	15.21 ± 0.04	14.32 ± 0.04	13.85 ± 0.05	15.13 ± 0.01	14.43 ± 0.02	13.90 ± 0.01	1
PSO J152.2+15	16.89 ± 0.20	15.58 ± 0.15	15.45 ± 0.17	16.68 ± 0.04	16.14 ± 0.04	$[15.53 \pm 0.11]$	1
PSO J158.1+05	16.62 ± 0.01	15.95 ± 0.02	15.35 ± 0.01	2
PSO J159.0–27	15.92 ± 0.10	15.31 ± 0.12	14.62 ± 0.10	16.02 ± 0.02	15.36 ± 0.01	$[14.72 \pm 0.07]$	1
PSO J159.2–26	16.81 ± 0.17	16.01 ± 0.13	15.30 ± 0.17	16.71 ± 0.03	16.03 ± 0.03	15.51 ± 0.03	1
PSO J160.0–21	16.58 ± 0.12	16.06 ± 0.15	15.47 ± 0.18	16.49 ± 0.02	16.01 ± 0.03	$[15.55 \pm 0.10]$	1
PSO J167.1+08	16.58 ± 0.16	15.50 ± 0.11	15.03 ± 0.16	16.56 ± 0.01	15.65 ± 0.01	14.99 ± 0.01	2
PSO J168.1–27	17.14 ± 0.02	16.75 ± 0.03	16.71 ± 0.07	3
PSO J174.6–18	16.35 ± 0.09	15.63 ± 0.10	15.18 ± 0.17	16.29 ± 0.05	15.67 ± 0.04	$[15.13 \pm 0.11]$	1
PSO J175.2+16	16.86 ± 0.15	16.14 ± 0.24	15.23 ± 0.13	16.82 ± 0.02	15.95 ± 0.01	15.24 ± 0.01	2
PSO J175.8–20	16.74 ± 0.17	16.30 ± 0.04	$[15.99 \pm 0.20]$	1

Table 2—Continued

Name	2MASS Photometry			MKO Photometry			Ref. ^a
	$J_{2\text{MASS}}$ (mag)	$H_{2\text{MASS}}$ (mag)	$K_{2\text{MASS}}$ (mag)	J_{MKO} (mag)	H_{MKO} (mag)	K_{MKO} (mag)	
PSO J180.1–28	15.98 ± 0.09	15.07 ± 0.07	14.68 ± 0.10	15.96 ± 0.02	15.15 ± 0.01	[14.75 ± 0.05]	1
PSO J182.6–26	16.48 ± 0.12	15.73 ± 0.12	15.20 ± 0.16	16.72 ± 0.05	16.11 ± 0.06	[15.28 ± 0.09]	1
PSO J183.4+40	17.05 ± 0.04	16.86 ± 0.05	[16.76 ± 0.27]	1
PSO J183.9–09	16.33 ± 0.13	15.45 ± 0.11	14.85 ± 0.14	16.31 ± 0.01	15.57 ± 0.01	[14.95 ± 0.10]	3
PSO J186.5+21	17.07 ± 0.20	16.41 ± 0.28	15.39 ± 0.18	16.92 ± 0.02	16.33 ± 0.02	15.79 ± 0.02	2
PSO J192.5+26	16.40 ± 0.01	16.74 ± 0.02	16.79 ± 0.05	2
PSO J192.6–21	16.84 ± 0.04	16.30 ± 0.04	[16.22 ± 0.17]	1
PSO J202.1–03	16.94 ± 0.03	16.69 ± 0.04	[16.70 ± 0.26]	1
PSO J202.5–26	16.67 ± 0.12	16.19 ± 0.14	15.45 ± 0.19	16.73 ± 0.08	16.24 ± 0.04	[16.28 ± 0.34]	1
PSO J207.7+29	16.97 ± 0.15	15.79 ± 0.15	15.41 ± 0.14	17.18 ± 0.02	16.41 ± 0.02	15.50 ± 0.02	2
PSO J218.4+50	16.91 ± 0.03	16.54 ± 0.04	[16.16 ± 0.15]	1
PSO J218.5–27	16.58 ± 0.12	15.60 ± 0.12	14.83 ± 0.11	16.32 ± 0.03	15.43 ± 0.02	[14.59 ± 0.08]	1
PSO J224.3+47	17.08 ± 0.03	17.43 ± 0.06	[17.09 ± 0.26]	1
PSO J228.6–29	16.79 ± 0.19	15.95 ± 0.15	15.31 ± 0.16	16.72 ± 0.05	16.18 ± 0.05	[15.37 ± 0.11]	1
PSO J229.2–26	16.46 ± 0.13	15.98 ± 0.18	15.18 ± 0.15	16.76 ± 0.03	15.85 ± 0.02	[15.14 ± 0.08]	1
PSO J231.2+08	17.19 ± 0.02	16.71 ± 0.02	16.31 ± 0.03	2
PSO J231.7–26	15.96 ± 0.08	15.21 ± 0.11	14.62 ± 0.10	15.98 ± 0.02	15.25 ± 0.03	[14.64 ± 0.05]	1
PSO J231.8–29	15.77 ± 0.09	14.83 ± 0.07	14.33 ± 0.08	[[15.72 ± 0.09]]	[[14.91 ± 0.08]]	[[14.29 ± 0.08]]	1
PSO J237.1–23	14.79 ± 0.05	14.13 ± 0.07	13.60 ± 0.05	[[14.73 ± 0.06]]	[[14.19 ± 0.07]]	[[13.57 ± 0.06]]	1
PSO J239.7–23	16.30 ± 0.11	15.35 ± 0.11	15.00 ± 0.13	16.25 ± 0.02	15.54 ± 0.02	[15.02 ± 0.07]	1
PSO J241.1+39	17.71 ± 0.13	[17.13 ± 0.15]	16.71 ± 0.07	1
PSO J242.9+02	17.11 ± 0.13	16.40 ± 0.09	[16.07 ± 0.16]	1
PSO J244.1+06	17.51 ± 0.06	16.35 ± 0.04	[15.54 ± 0.10]	1
PSO J244.6+08	16.84 ± 0.03	16.80 ± 0.03	[16.80 ± 0.18]	1
PSO J249.4–10	16.43 ± 0.15	>14.74	>14.16	16.53 ± 0.03	15.69 ± 0.02	[14.90 ± 0.07]	1
PSO J255.6+10	18.34 ± 0.09	17.27 ± 0.05	[16.20 ± 0.24]	1
PSO J258.2+06	16.16 ± 0.09	15.34 ± 0.10	14.78 ± 0.11	16.03 ± 0.02	15.42 ± 0.02	14.76 ± 0.02	1
PSO J260.1+61
PSO J260.3+46	16.86 ± 0.15	15.83 ± 0.15	15.23 ± 0.13	16.79 ± 0.02	15.84 ± 0.02	[15.24 ± 0.09]	1
PSO J261.2+22	16.83 ± 0.03	16.89 ± 0.04	[16.86 ± 0.20]	1
PSO J263.5+50	16.34 ± 0.11	15.85 ± 0.14	>15.37	[[16.15 ± 0.13]]	[[15.90 ± 0.21]]	[[15.82 ± 0.24]] ^c	1
PSO J265.0+11	17.48 ± 0.08	16.59 ± 0.06	[16.38 ± 0.15]	1
PSO J268.7+18	16.02 ± 0.09	15.22 ± 0.09	14.68 ± 0.13	15.82 ± 0.02	15.32 ± 0.02	15.24 ± 0.02	1
PSO J272.0–04	16.90 ± 0.03	[16.28 ± 0.05]	[15.74 ± 0.06]	1
PSO J272.4–04	15.14 ± 0.05	14.28 ± 0.05	13.96 ± 0.06	15.15 ± 0.01	[14.49 ± 0.04]	13.98 ± 0.01	1
PSO J274.0+30	17.53 ± 0.07	16.93 ± 0.06	[17.33 ± 0.31]	1
PSO J276.0–01	>16.39	>15.84	15.03 ± 0.16	17.60 ± 0.08	16.21 ± 0.04	[15.48 ± 0.10]	1
PSO J276.8+22	16.91 ± 0.17	15.58 ± 0.11	14.87 ± 0.08	16.48 ± 0.03	15.62 ± 0.02	[14.82 ± 0.07]	1
PSO J277.7+45	17.22 ± 0.04	16.23 ± 0.03	[15.55 ± 0.08]	1
PSO J280.2+63	16.13 ± 0.10	15.34 ± 0.10	14.83 ± 0.12	[[16.02 ± 0.12]]	[[15.43 ± 0.11]]	[[14.82 ± 0.13]]	1
PSO J282.5+34	17.25 ± 0.24	16.26 ± 0.20	15.40 ± 0.20	17.10 ± 0.03	16.28 ± 0.03	[15.68 ± 0.08]	1
PSO J282.7+59	14.94 ± 0.04	13.97 ± 0.03	13.46 ± 0.04	14.85 ± 0.01	14.03 ± 0.02	[13.40 ± 0.02]	1
PSO J284.7+39	17.41 ± 0.04	17.17 ± 0.06	[17.03 ± 0.19]	1
PSO J289.8+30	15.57 ± 0.05	14.60 ± 0.05	13.95 ± 0.05	15.52 ± 0.02	14.56 ± 0.01	[13.95 ± 0.03]	1
PSO J291.2+68	16.61 ± 0.15	16.11 ± 0.21	15.49 ± 0.23	[[16.52 ± 0.17]]	[[16.19 ± 0.23]]	[[15.52 ± 0.25]]	1
PSO J296.0+35	16.42 ± 0.11	15.88 ± 0.15	15.20 ± 0.15	16.47 ± 0.03	15.94 ± 0.03	[15.76 ± 0.13]	1
PSO J303.7+31	16.07 ± 0.09	15.22 ± 0.09	15.24 ± 0.16	[[16.06 ± 0.15]]	[[15.28 ± 0.19]]	[[15.24 ± 0.32]]	1
PSO J304.7–07	16.81 ± 0.17	15.97 ± 0.16	15.37 ± 0.19	16.77 ± 0.03	16.24 ± 0.03	[15.70 ± 0.10]	1
PSO J307.6+07	14.23 ± 0.03	13.44 ± 0.03	13.32 ± 0.04	14.05 ± 0.01	13.48 ± 0.01	[13.37 ± 0.04]	1
PSO J308.9–09	17.67 ± 0.08	16.86 ± 0.06	[16.33 ± 0.12]	1
PSO J310.9+62	15.60 ± 0.07	14.70 ± 0.07	14.42 ± 0.07	[[15.46 ± 0.07]]	[[14.78 ± 0.08]]	[[14.44 ± 0.09]]	1
PSO J313.1–26	17.24 ± 0.06	16.49 ± 0.04	[15.92 ± 0.11]	1
PSO J316.5+04	16.81 ± 0.20	16.02 ± 0.22	15.59 ± 0.24	17.01 ± 0.04	16.09 ± 0.03	[15.49 ± 0.07]	1
PSO J319.3–29	15.60 ± 0.06	14.53 ± 0.04	14.15 ± 0.07	15.45 ± 0.02	14.65 ± 0.01	[14.17 ± 0.08]	1
PSO J321.1+18	17.03 ± 0.22	15.89 ± 0.15	15.36 ± 0.17	16.99 ± 0.03	16.10 ± 0.03	[15.42 ± 0.05]	1
PSO J329.8+03	16.98 ± 0.02	16.29 ± 0.02	15.72 ± 0.02	2
PSO J330.3+32	16.35 ± 0.09	15.44 ± 0.09	>15.23	16.13 ± 0.04	15.63 ± 0.04	[15.34 ± 0.09]	1
PSO J331.6+33	16.58 ± 0.11	15.89 ± 0.10	>17.23	16.66 ± 0.03	16.08 ± 0.03	[15.75 ± 0.15]	1
PSO J331.9–07	17.41 ± 0.25	15.96 ± 0.18	15.66 ± 0.25	17.54 ± 0.05	16.45 ± 0.03	[15.50 ± 0.07]	1
PSO J334.1+19	16.59 ± 0.06	16.41 ± 0.07	[16.28 ± 0.14]	1
PSO J334.8+11	16.74 ± 0.12	15.28 ± 0.11	14.82 ± 0.10	16.58 ± 0.02	15.61 ± 0.02	[14.90 ± 0.05]	1
PSO J336.9–18	17.00 ± 0.16	15.76 ± 0.12	15.24 ± 0.14	17.37 ± 0.05	16.10 ± 0.02	[15.14 ± 0.07]	1
PSO J337.4+16	17.02 ± 0.03	16.46 ± 0.05	[15.85 ± 0.08]	1
PSO J338.8+31	17.05 ± 0.03	16.19 ± 0.03	[15.75 ± 0.07]	1

Table 2—Continued

Name	2MASS Photometry			MKO Photometry			Ref. ^a
	$J_{2\text{MASS}}$ (mag)	$H_{2\text{MASS}}$ (mag)	$K_{2\text{MASS}}$ (mag)	J_{MKO} (mag)	H_{MKO} (mag)	K_{MKO} (mag)	
PSO J339.0+51	14.58 ± 0.03	14.49 ± 0.05	14.45 ± 0.09	14.46 ± 0.01	14.62 ± 0.02	$[14.57 \pm 0.03]$	1
PSO J341.7–15	16.41 ± 0.09	15.40 ± 0.09	14.83 ± 0.11	16.43 ± 0.02	15.55 ± 0.02	$[14.78 \pm 0.05]$	1
PSO J342.3–16	16.12 ± 0.08	15.26 ± 0.09	14.83 ± 0.11	16.09 ± 0.02	15.37 ± 0.02	$[14.83 \pm 0.04]$	1
PSO J342.9–09	18.85 ± 0.14	17.98 ± 0.10	$[17.31 \pm 0.39]$	1
PSO J344.8+20	16.58 ± 0.19	15.66 ± 0.15	14.85 ± 0.12	16.76 ± 0.03	15.76 ± 0.03	$[15.00 \pm 0.05]$	1
PSO J346.3–11	17.71 ± 0.37	15.92 ± 0.21	15.40 ± 0.19	17.13 ± 0.03	16.24 ± 0.03	$[15.51 \pm 0.07]$	1
PSO J346.5–15	16.69 ± 0.15	15.25 ± 0.10	14.78 ± 0.12	16.56 ± 0.02	15.50 ± 0.02	$[14.63 \pm 0.06]$	1
PSO J348.8+06	15.86 ± 0.08	14.76 ± 0.07	14.07 ± 0.06	15.75 ± 0.01	14.89 ± 0.01	14.11 ± 0.01	2
PSO J350.4–19	17.15 ± 0.18	15.85 ± 0.15	15.15 ± 0.13	16.86 ± 0.03	15.93 ± 0.02	$[15.31 \pm 0.07]$	1
PSO J353.0–29	17.03 ± 0.18	16.84 ± 0.30	15.69 ± 0.23	17.42 ± 0.04	16.68 ± 0.06	$[16.20 \pm 0.15]$	1
PSO J353.6+13	>16.65	15.78 ± 0.15	14.76 ± 0.10	16.60 ± 0.01	15.58 ± 0.01	14.66 ± 0.01	2
PSO J353.8+45 ^b	16.70 ± 0.19	>15.26	>14.46	16.83 ± 0.03	15.63 ± 0.02	$[14.65 \pm 0.05]$	1
PSO J357.8+49	16.54 ± 0.13	15.77 ± 0.15	15.15 ± 0.13	16.48 ± 0.02	15.91 ± 0.04	15.50 ± 0.04	1
PSO J359.8–01	17.24 ± 0.20	16.03 ± 0.17	16.09 ± 0.27	17.05 ± 0.03	16.36 ± 0.04	$[15.97 \pm 0.11]$	1

Note. — All 2MASS photometry is from the 2MASS Point Source Catalog (Cutri et al. 2003) except where noted. For MKO photometry, H and K band magnitudes enclosed in single brackets were synthesized using observed J band magnitudes and our low-resolution spectra. MKO magnitudes enclosed in double brackets were synthesized using the 2MASS magnitudes for the corresponding filters and our low-resolution spectra.

^aReferences for MKO photometry: (1) this work, (2) UKIDSS DR9 (Lawrence et al. 2013), (3) VISTA Hemisphere Survey (Cross et al. 2012).

^b2MASS photometry from 2MASS Point Source Reject Table (Skrutskie et al. 2006).

^cCalibrated using the 2MASS H magnitude because the 2MASS K magnitude is an upper limit.

Table 3. IRTF/SpeX Observations

Object	Date (UT)	Slit (")	t_{int} (s)	A0 V Standard
PSO J003.4–18	2012 Dec 1	0.8	720	HD 3604
PSO J004.1+23	2012 Dec 1	0.8	720	HD 9711
PSO J004.7+51	2013 Sep 22	0.8	540	HD 19844
PSO J007.7+57	2012 Sep 24	0.8	200	HD 240290
PSO J007.9+33	2013 Sep 22	0.8	540	HD 15240
PSO J010.2+41	2012 Oct 28	0.8	2880	HD 219290
PSO J023.8+02	2012 Nov 8	0.8	720	HD 18571
PSO J024.1+37	2012 Oct 25	0.8	2880	HD 12381
PSO J031.5+20	2013 Jul 12	0.8	960	HD 6313
PSO J041.5+01	2013 Jan 26	0.8	960	HD 18571
PSO J048.9+07	2013 Jan 26	0.8	720	HD 18571
PSO J049.1+17	2013 Jan 26	0.8	960	HD 18571
PSO J049.1+26	2012 Nov 8	0.8	720	HD 18571
PSO J052.7–03	2012 Nov 8	0.8	720	HD 18571
PSO J053.3+30	2012 Sep 26	0.5	720	HD 22859
PSO J054.8–11	2013 Jan 26	0.8	840	HD 27700
PSO J055.0–21	2013 Jan 26	0.8	1080	HD 27166
PSO J057.2+15	2014 Jan 18	0.8	1440	HD 25175
PSO J068.3+52	2013 Jan 26	0.8	960	HD 31064
PSO J068.9+13	2012 Nov 7	0.8	720	HD 27761
PSO J070.3+04	2013 Jan 25	0.8	1200	HD 31411
PSO J071.4+36	2013 Apr 4	0.8	600	HD 35656
PSO J071.6–24	2013 Jan 26	0.8	600	HD 46996
PSO J071.8–12	2013 Jan 26	0.8	840	HD 27700
PSO J076.1+25	2014 Jan 17	0.8	720	HD 35036
PSO J076.7+52	2013 Jan 25	0.8	720	HD 33654
PSO J078.9+31	2013 Jan 26	0.8	540	HD 38245
	2015 Jan 28	0.5	1080	HD 31411
PSO J078.9+31	2013 Jan 26	0.8	540	HD 38245
PSO J085.3+36	2013 Jan 26	0.8	360	HD 38245
PSO J087.7–12	2013 Jan 25	0.8	960	HD 44442
PSO J088.0+43	2013 Apr 4	0.8	480	HD 39250
PSO J088.3–24	2013 Apr 17	0.8	720	HD 43070
PSO J100.5+41	2013 Jan 25	0.8	720	HD 50931
PSO J101.8+39	2013 Jan 25	0.8	960	HD 63586
PSO J103.0+41	2012 Sep 26	0.5	960	HD 39250
PSO J105.4+63	2012 Oct 25	0.8	180	HD 33654
PSO J108.4+38	2013 Apr 4	0.8	480	HD 56248
PSO J109.4+46	2013 Apr 4	0.8	960	HD 63586
PSO J115.0+59	2013 Apr 4	0.8	840	HD 56385
PSO J117.1+17	2013 Jan 25	0.8	360	HD 79752
PSO J127.4+10	2014 Jan 17	0.8	960	HD 79108
PSO J133.8–02	2013 Apr 4	0.8	480	HD 89911
PSO J133.8+06	2013 Apr 14	0.8	1440	HD 74721
	2015 Jan 20	0.5	1440	HD 74721
PSO J135.0+32	2013 Jan 25	0.8	360	HD 79108
	2015 May 29	0.5	2760	HD 79108
PSO J135.7+16	2013 Apr 17	0.8	840	GSC 1407-00828
PSO J136.3+10	2013 May 15	0.8	960	HD 79108
PSO J136.5–06	2012 Nov 8	0.8	720	HD 58056
PSO J140.2+45	2012 Nov 8	0.8	720	HD 33654
PSO J143.6–29	2013 Apr 5	0.8	600	HD 87727
PSO J146.0+05	2013 Apr 17	0.8	2160	HD 93346, HD 97516
PSO J147.5–27	2013 Apr 17	0.8	1920	HD 87727
PSO J149.0–14	2013 Apr 5	0.8	960	HD 87727
PSO J149.1–19	2013 Nov 23	0.8	360	HD 90723
PSO J152.2+15	2013 Apr 18	0.8	720	HD 97516
PSO J158.1+05	2013 Apr 18	0.8	720	HD 89239
	2015 Jan 20	0.5	2160	HD 89239
PSO J159.0–27	2013 Apr 17	0.5	1200	HD 81694
PSO J159.2–26	2013 Apr 5	0.8	1440	HD 98949
PSO J160.0–21	2013 Apr 4	0.8	960	HD 98201
PSO J167.1+08	2013 Apr 4	0.8	960	HD 108140
PSO J168.1–27	2014 Jan 17	0.8	960	HD 93185
PSO J174.6–18	2013 Apr 5	0.8	960	HD 101122
PSO J175.2+16	2013 Apr 5	0.8	1320	HD 112304

Table 3—Continued

Object	Date (UT)	Slit (")	t_{int} (s)	A0 V Standard
PSO J175.8–20	2014 Jan 17	0.8	720	HD 105764
PSO J180.1–28	2013 Apr 3	0.8	720	HD 89911
PSO J182.6–26	2013 Apr 17	0.8	2160	HD 125509
PSO J183.4+40	2013 Jul 13	0.8	1320	HD 109055
PSO J183.9–09	2013 Apr 5	0.8	720	HD 112304
PSO J186.5+21	2013 Apr 4	0.8	1200	HD 109691
PSO J192.5+26	2013 Jul 12	0.8	960	HD 111744
PSO J192.6–21	2013 Apr 4	0.8	960	HD 110902
PSO J202.1–03	2013 Jul 12	0.8	1200	HD 122749
PSO J202.5–26	2013 Apr 19	0.8	960	HD 126458
PSO J207.7+29	2013 Jul 12	0.8	1680	HD 122945
PSO J218.4+50	2013 Jul 12	0.8	1680	HD 179933
PSO J218.5–27	2013 Jul 14	0.8	720	HD 125438
PSO J224.3+47	2013 Jul 13	0.8	1200	HD 128039
PSO J231.2+08	2012 Jul 7	0.8	960	7 Ser
PSO J241.1+39	2012 Aug 10	0.8	1920	26 Ser
PSO J242.9+02	2012 Jul 8	0.8	1200	q Her
PSO J244.1+06	2012 Jul 8	0.8	1500	q Her
PSO J244.6+08	2012 Jul 7	0.8	1200	q Her
PSO J249.4–10	2013 Apr 16	0.8	960	HD 157170
PSO J255.6+10	2012 Oct 6	0.8	3720	HD 160512
PSO J258.2+06	2013 Apr 5	0.8	720	HD 161289
PSO J260.1+61	2012 Oct 15	0.8	2640	BD+60 2651
PSO J260.3+46	2012 Oct 7	0.8	1920	HD 179933
PSO J261.2+22	2013 Jul 12	0.8	960	HD 165029
PSO J263.5+50	2012 Sep 26	0.8	600	HD 199217
PSO J265.0+11	2012 Jul 6	0.8	2160	HD 171149
PSO J268.7+18	2012 Oct 15	0.8	720	HD 165029
PSO J272.0–04	2013 Jul 13	0.8	1440	HD 173591
PSO J272.4–04	2012 Oct 14	0.8	720	HD 173591
PSO J274.0+30	2012 Jul 7	0.8	1440	HD 165029
PSO J276.0–01	2013 Jul 13	0.8	2160	HD 165029
PSO J276.8+22	2012 Oct 17	0.8	960	HD 332937
PSO J277.7+45	2012 Sep 20	0.5	1200	HD 199217
PSO J280.2+63	2012 Oct 19	0.8	960	HD 179933
PSO J282.5+34	2012 Oct 17	0.8	1440	HD 332937
PSO J282.7+59	2012 Sep 26	0.8	240	HD 240290
PSO J284.7+39	2012 Sep 20	0.8	960	HD 197291
PSO J289.8+30	2012 Oct 6	0.8	720	HD 199217
PSO J291.2+68	2012 Oct 19	0.8	720	HD 179933
PSO J296.0+35	2012 Oct 25	0.8	720	HD 191225
PSO J303.7+31	2012 Aug 10	0.8	3600	HD 192243
PSO J304.7–07	2012 Nov 8	0.8	1200	HD 196442
PSO J307.6+07	2012 Sep 20	0.8	80	HD 189920
PSO J308.9–09	2012 Sep 20	0.8	1200	HD 189920
PSO J310.9+62	2012 Oct 6	0.8	720	HD 222749
PSO J313.1–26	2012 Oct 6	0.8	1920	HD 202941
PSO J316.5+04	2012 Oct 28	0.8	1920	HD 210501
PSO J319.3–29	2012 Sep 20	0.8	150	HD 195062
PSO J321.1+18	2012 Oct 6	0.8	1920	HD 209932
PSO J329.8+03	2012 Oct 17	0.8	960	HD 210501
PSO J330.3+32	2012 Aug 10	0.8	480	HD 210501
PSO J331.6+33	2012 Sep 20	0.8	960	BD+39 4890
PSO J331.9–07	2012 Oct 6	0.8	2160	HD 219833
PSO J334.1+19	2012 Aug 10	0.8	600	HD 210501
PSO J334.8+11	2012 Nov 7	0.8	720	HD 210501
PSO J336.9–18	2013 Jul 13	0.8	960	HD 202025
PSO J337.4+16	2012 Nov 8	0.8	1200	HD 210501
PSO J338.8+31	2012 Nov 7	0.8	720	HD 210501
PSO J339.0+51	2012 Oct 7	0.8	1200	HD 222749
PSO J341.7–15	2012 Oct 19	0.8	960	HD 213030
PSO J342.3–16	2012 Nov 7	0.8	720	HD 219833
PSO J342.9–09	2012 Sep 20	0.8	960	HD 216807
PSO J344.8+20	2012 Nov 8	0.5	720	HD 210501
PSO J346.3–11	2012 Nov 8	0.5	960	HD 215833
PSO J346.5–15	2012 Nov 8	0.5	720	HD 219545

Table 3—Continued

Object	Date (UT)	Slit (")	t_{int} (s)	A0 V Standard
PSO J348.8+06	2012 Sep 20	0.8	360	HD 216807
	2015 Jun 28	0.5	70	HD 210501
PSO J350.4–19	2012 Nov 8	0.5	960	HD 219545
PSO J353.0–29	2012 Sep 20	0.8	2160	HD 215298
PSO J353.6+13	2012 Nov 8	0.5	720	HD 7215
PSO J353.8+45	2012 Nov 8	0.5	960	HD 222749
PSO J357.8+49	2012 Nov 8	0.5	720	HD 222749
PSO J359.8–01	2012 Dec 1	0.8	840	HD 222749

Note. — All observations performed in prism mode with the 0.8×15 arcsec ($R \approx 75$) or 0.5×15 arcsec ($R \approx 120$) slit. Observations for PSO J007.7+57, PSO J103.0+41, PSO J140.2+45, PSO J272.4–04, PSO J282.7+59, PSO J307.6+07, and PSO J339.0+51 were originally presented in Best et al. (2013).

Table 4. Visual Spectral Types and Kinematics

Name	SpT (visual)	$d_{\text{phot}}^{\text{a}}$ (pc)	$\mu_{\alpha} \cos \delta^{\text{b}}$ (mas yr $^{-1}$)	μ_{δ}^{b} (mas yr $^{-1}$)	v_{tan} (km s $^{-1}$)	Discovery References
PSO J003.4–18	L5 pec	46.1 ± 5.6	-31 ± 12	-175 ± 13	39 ± 6	1
PSO J004.1+23	T0	24.7 ± 2.5	398 ± 13	36 ± 15	47 ± 5	2
PSO J004.7+51	L7	23.4 ± 2.8	293 ± 4	-12 ± 7	33 ± 4	2
PSO J007.7+57	L9	11.6 ± 1.4	526 ± 2	-12 ± 4	29 ± 3	3,4
PSO J007.9+33	L9	21.4 ± 2.6	-19 ± 5	-10 ± 6	2 ± 1	2
PSO J023.8+02	L9.5	28.8 ± 3.0	87 ± 11	-470 ± 12	65 ± 7	2
PSO J024.1+37	M7	134.8 ± 22.6	-6 ± 10	-7 ± 15	6 ± 8	2
PSO J031.5+20	T5.5	24.7 ± 2.3	286 ± 34	88 ± 28	35 ± 5	2
PSO J041.5+01	L8.5	27.7 ± 3.4	28 ± 13	-50 ± 12	8 ± 2	2
PSO J048.9+07	L6: (blue)	41.9 ± 5.1	52 ± 21	53 ± 22	15 ± 5	2
PSO J049.1+17	L9.5	40.3 ± 4.3	221 ± 22	-68 ± 24	44 ± 6	2
PSO J049.1+26	T2.5	23.5 ± 2.4	204 ± 15	-25 ± 19	23 ± 3	2
PSO J052.7–03	L9:	19.1 ± 2.3	-140 ± 7	60 ± 7	14 ± 2	2
PSO J054.8–11	L3:	50.3 ± 6.1	16 ± 11	-73 ± 11	18 ± 3	2
PSO J055.0–21	T2	31.3 ± 3.3	230 ± 11	-155 ± 16	41 ± 5	2
PSO J057.2+15	L7 (red)	25.2 ± 3.0	68 ± 11	-127 ± 12	17 ± 3	2
PSO J068.9+13	L6 (red)	34.9 ± 4.3	108 ± 9	-14 ± 10	18 ± 3	5 ^c ,6
PSO J070.3+04	T4.5	23.9 ± 2.3	186 ± 7	-68 ± 8	22 ± 2	2
PSO J071.4+36	L6:	36.3 ± 4.4	-16 ± 13	-154 ± 18	27 ± 4	2
PSO J071.6–24	L6 (blue)	35.3 ± 4.3	-199 ± 13	398 ± 16	74 ± 9	3
PSO J071.8–12	T2:	27.7 ± 2.9	20 ± 19	-89 ± 19	12 ± 3	2
PSO J076.7+52	T4.5	17.6 ± 1.6	57 ± 4	-196 ± 7	17 ± 2	2
PSO J078.9+31	L1.5	65.7 ± 11.2	25 ± 4	-58 ± 4	20 ± 4	2
PSO J087.7–12	L8	25.5 ± 3.1	-144 ± 11	-39 ± 9	18 ± 3	2
PSO J088.0+43	L4 pec	42.8 ± 5.2	2 ± 4	-80 ± 6	16 ± 2	2
PSO J088.3–24	L1:	100.5 ± 17.1	16 ± 7	-21 ± 6	13 ± 4	2
PSO J100.5+41	L9 (red)	16.1 ± 1.9	12 ± 4	-372 ± 6	28 ± 3	7
PSO J101.8+39	M9.5	97.2 ± 16.5	1 ± 7	-23 ± 9	11 ± 5	2
PSO J103.0+41	T0	14.2 ± 1.4	3 ± 3	-32 ± 5	2 ± 0	4
PSO J105.4+63	T2.5	16.7 ± 1.7	-14 ± 2	-264 ± 5	21 ± 2	7
PSO J108.4+38	L7	29.1 ± 3.5	-36 ± 9	-60 ± 11	10 ± 2	2
PSO J109.4+46	T0	41.5 ± 4.5	39 ± 8	-29 ± 12	10 ± 2	2
PSO J115.0+59	M9.5	108.8 ± 18.6	-17 ± 36	-34 ± 16	20 ± 12	2
PSO J117.1+17	L5	31.3 ± 3.8	-63 ± 5	8 ± 6	9 ± 1	8 ^c ,9
PSO J127.4+10	L4	40.4 ± 4.9	0 ± 7	-45 ± 8	9 ± 2	2
PSO J133.8–02	T0 pec	23.8 ± 2.4	-157 ± 6	101 ± 7	21 ± 2	2
PSO J133.8+06	M9	84.9 ± 14.3	-12 ± 11	-37 ± 11	16 ± 5	2
PSO J135.0+32	L1.5	45.2 ± 7.5	-91 ± 5	-11 ± 5	20 ± 3	2
PSO J135.7+16	T0 pec	29.0 ± 3.0	25 ± 14	-24 ± 17	5 ± 2	8 ^c ,2
PSO J136.3+10	T1	31.2 ± 3.3	-8 ± 11	-118 ± 8	18 ± 2	10
PSO J136.5–06	L2 pec	32.4 ± 5.4	34 ± 5	-17 ± 4	6 ± 1	2
PSO J140.2+45	L9.5	14.3 ± 1.5	-77 ± 4	-852 ± 5	58 ± 6	11 ^c ,7,4
PSO J143.6–29	L1	76.4 ± 12.8	-11 ± 12	-65 ± 14	24 ± 6	2
PSO J146.0+05	L1	80.2 ± 13.6	19 ± 18	-35 ± 22	15 ± 8	2

Table 4—Continued

Name	SpT (visual)	$d_{\text{phot}}^{\text{a}}$ (pc)	$\mu_{\alpha} \cos \delta^{\text{b}}$ (mas yr $^{-1}$)	μ_{δ}^{b} (mas yr $^{-1}$)	v_{tan} (km s $^{-1}$)	Discovery References
PSO J147.5–27	L0.5	104.4 ± 17.8	-8 ± 15	-17 ± 19	9 ± 9	2
PSO J149.0–14	L9	17.7 ± 2.1	96 ± 5	-148 ± 6	15 ± 2	2
PSO J149.1–19	L5 pec	25.8 ± 3.1	-100 ± 4	27 ± 5	13 ± 2	2
PSO J152.2+15	L1.5	77.3 ± 13.1	-200 ± 17	-51 ± 34	76 ± 15	2
PSO J158.1+05	L2 (blue)	68.6 ± 11.6	-186 ± 5	-120 ± 6	72 ± 12	2
PSO J159.0–27	L2 (blue)	56.4 ± 9.4	-55 ± 5	-244 ± 5	67 ± 11	2
PSO J159.2–26	T1.5	25.7 ± 2.7	-12 ± 14	12 ± 15	2 ± 2	2
PSO J160.0–21	T2 pec	27.0 ± 2.8	-231 ± 16	-49 ± 14	30 ± 4	2
PSO J167.1+08	L8	28.8 ± 3.5	-246 ± 17	-313 ± 17	54 ± 7	8 ^c ,2
PSO J168.1–27	T2.5	36.5 ± 4.0	-273 ± 121	104 ± 39	51 ± 20	2
PSO J174.6–18	M9	91.3 ± 15.4	-77 ± 11	102 ± 12	56 ± 11	2
PSO J175.2+16	L5	47.2 ± 5.8	-13 ± 19	-35 ± 22	8 ± 5	2
PSO J175.8–20	T2	30.2 ± 3.2	-38 ± 9	-137 ± 8	20 ± 2	2
PSO J180.1–28	T0	23.8 ± 2.4	-545 ± 6	-39 ± 7	62 ± 6	2
PSO J182.6–26	L2	68.3 ± 11.5	-82 ± 12	-10 ± 14	27 ± 6	2
PSO J183.4+40	T4	33.4 ± 3.6	-118 ± 7	-82 ± 10	23 ± 3	2
PSO J183.9–09	L0	69.5 ± 11.6	-69 ± 11	-24 ± 13	24 ± 5	2
PSO J186.5+21	M9	123.3 ± 21.1	-23 ± 22	-26 ± 25	20 ± 14	12 ^c ,2
PSO J192.5+26	T6	22.1 ± 2.0	-514 ± 35	-621 ± 33	85 ± 9	7
PSO J192.6–21	T2.5	33.9 ± 3.6	-162 ± 10	-88 ± 11	30 ± 4	2
PSO J202.1–03	T4.5	24.6 ± 2.2	-168 ± 13	2 ± 15	20 ± 2	2
PSO J207.7+29	T0: pec	25.9 ± 2.7	-156 ± 12	-68 ± 16	21 ± 3	2
PSO J218.4+50	T2.5	32.9 ± 3.4	36 ± 8	-156 ± 15	25 ± 4	2
PSO J218.5–27	L6	32.2 ± 3.9	-75 ± 8	-9 ± 11	12 ± 2	2
PSO J224.3+47	T7	19.9 ± 1.8	100 ± 41	-67 ± 61	11 ± 5	2
PSO J231.2+08	T2:	32.0 ± 3.3	24 ± 8	-77 ± 9	12 ± 2	10
PSO J241.1+39	T2	42.2 ± 4.4	132 ± 9	11 ± 9	27 ± 3	2
PSO J242.9+02	T1	35.1 ± 3.7	65 ± 7	93 ± 7	19 ± 2	2
PSO J244.1+06	L9 (red)	32.6 ± 4.0	-88 ± 8	-46 ± 9	15 ± 2	2
PSO J244.6+08	T4.5	30.2 ± 2.9	37 ± 20	-31 ± 31	7 ± 4	2
PSO J258.2+06	T0 pec	21.9 ± 2.2	-186 ± 8	-113 ± 7	23 ± 2	2
PSO J260.1+61	T2	45.4 ± 4.7	-2 ± 68	192 ± 134	41 ± 29	2
PSO J260.3+46	L9	30.4 ± 3.7	54 ± 9	-265 ± 15	39 ± 5	2
PSO J261.2+22	T5	31.6 ± 3.1	-43 ± 12	0 ± 15	6 ± 2	2
PSO J263.5+50	T4	24.5 ± 2.5	-19 ± 8	293 ± 15	34 ± 4	7
PSO J265.0+11	T0.5	43.4 ± 4.7	13 ± 61	52 ± 45	11 ± 10	2
PSO J268.7+18	T2.5	21.1 ± 2.2	-424 ± 7	10 ± 9	43 ± 4	7
PSO J272.0–04	T1.5 pec	27.8 ± 3.0	11 ± 43	-37 ± 64	5 ± 8	2
PSO J272.4–04	T1	15.0 ± 1.5	-46 ± 4	-400 ± 13	29 ± 3	7,4
PSO J274.0+30	T3	36.4 ± 3.9	-33 ± 30	-127 ± 33	23 ± 6	2
PSO J276.8+22	L9	24.1 ± 2.9	58 ± 8	10 ± 9	7 ± 1	2
PSO J277.7+45	L9	33.8 ± 4.1	105 ± 6	133 ± 7	27 ± 3	13
PSO J280.2+63	L9.5	23.8 ± 2.4	-54 ± 3	125 ± 12	15 ± 2	2
PSO J282.5+34	L1	86.1 ± 14.5	44 ± 17	-10 ± 21	19 ± 8	2

Table 4—Continued

Name	SpT (visual)	$d_{\text{phot}}^{\text{a}}$ (pc)	$\mu_{\alpha} \cos \delta^{\text{b}}$ (mas yr $^{-1}$)	μ_{δ}^{b} (mas yr $^{-1}$)	v_{tan} (km s $^{-1}$)	Discovery References
PSO J282.7+59	L9	13.5 ± 1.6	32 ± 3	421 ± 6	27 ± 3	3,4
PSO J284.7+39	T4	39.9 ± 4.4	-5 ± 49	63 ± 32	12 ± 6	2
PSO J289.8+30	L9	19.2 ± 2.3	386 ± 4	421 ± 5	52 ± 6	3
PSO J291.2+68	T1	33.2 ± 3.4	-237 ± 10	-88 ± 22	40 ± 4	2
PSO J304.7-07	M9	110.4 ± 18.8	-49 ± 16	71 ± 18	45 ± 12	2
PSO J307.6+07	T1.5	10.9 ± 1.1	652 ± 5	-113 ± 6	34 ± 3	7,14,4
PSO J308.9-09	L4.5	65.0 ± 8.2	-15 ± 12	2 ± 12	5 ± 4	2
PSO J310.9+62	T1.5	16.5 ± 1.7	298 ± 2	515 ± 5	47 ± 5	7
PSO J313.1-26	L1	96.9 ± 16.8	182 ± 6	5 ± 5	84 ± 15	2
PSO J316.5+04	L6 (blue)	48.3 ± 6.0	34 ± 20	-60 ± 20	16 ± 5	2
PSO J319.3-29	T0:	16.9 ± 1.7	148 ± 4	-162 ± 4	18 ± 2	2
PSO J321.1+18	L9	31.8 ± 3.9	249 ± 18	100 ± 22	40 ± 6	2
PSO J329.8+03	T1:	30.7 ± 3.2	94 ± 22	-751 ± 20	110 ± 12	2
PSO J330.3+32	T2.5	20.1 ± 2.1	105 ± 8	64 ± 9	12 ± 1	2
PSO J331.6+33	T1.5	34.4 ± 3.7	176 ± 9	16 ± 11	29 ± 3	2
PSO J331.9-07	L7	34.1 ± 4.1	74 ± 19	-78 ± 22	17 ± 4	2
PSO J334.1+19	T3	30.7 ± 3.2	119 ± 11	-60 ± 9	19 ± 3	2
PSO J334.8+11	L5	37.0 ± 4.5	-25 ± 7	-72 ± 6	13 ± 2	2
PSO J336.9-18	L6:: (red)	32.9 ± 4.0	23 ± 13	-9 ± 13	4 ± 2	2
PSO J337.4+16	M9	129.4 ± 22.2	25 ± 6	-18 ± 5	19 ± 5	2
PSO J338.8+31	L2 pec	75.5 ± 12.7	42 ± 6	-6 ± 6	15 ± 3	2
PSO J339.0+51	T5	9.4 ± 0.8	732 ± 4	328 ± 5	36 ± 3	7,4
PSO J341.7-15	L5	39.0 ± 4.7	47 ± 5	58 ± 6	14 ± 2	2
PSO J342.3-16	L5:	36.7 ± 4.4	377 ± 6	143 ± 6	70 ± 9	2
PSO J344.8+20	L2.5	51.5 ± 6.2	54 ± 10	-29 ± 10	15 ± 3	2
PSO J346.3-11	L8.5	33.8 ± 4.2	131 ± 33	15 ± 33	21 ± 6	2
PSO J346.5-15	L7	27.1 ± 3.3	120 ± 6	14 ± 6	16 ± 2	2
PSO J348.8+06	L2	36.8 ± 6.1	59 ± 5	-30 ± 5	12 ± 2	2
PSO J350.4-19	L4.5	47.2 ± 5.8	72 ± 12	-37 ± 14	18 ± 4	2
PSO J353.0-29	L1:	104.8 ± 18.1	-97 ± 24	3 ± 25	48 ± 15	2
PSO J353.6+13	L8:	24.0 ± 2.9	46 ± 9	-2 ± 8	5 ± 1	2
PSO J353.8+45	L7.5	21.4 ± 2.6	-84 ± 4	-66 ± 5	11 ± 1	3
PSO J357.8+49	T0 (blue)	33.7 ± 3.5	-345 ± 7	-184 ± 12	62 ± 7	2
PSO J359.8-01	T1	34.5 ± 3.7	-2 ± 31	-149 ± 28	24 ± 5	2

Note. — Uncertainties for these visual spectral types are ± 0.5 subtypes, except for those listed with : (± 1.0 subtype) or :: ($\geq \pm 1.5$ subtypes).

^aPhotometric distances calculated using *W2* magnitudes and the polynomial from Dupuy & Liu (2012).

^bProper motions calculated using PS1 astrometry, as well as 2MASS astrometry when available.

^cPhotometric candidate.

References. — Discovery References: (1) Baron et al. (2015), (2) this paper, (3) Thompson et al. (2013), (4) Best et al. (2013) (Paper I), (5) Hogan et al. (2008), (6) Lodieu et al. (2014), (7) Mace

et al. (2013), (8) Zhang et al. (2009), (9) Bardalez Gagliuffi et al. (2014), (10) Marocco et al. (2015), (11) Aberasturi et al. (2011), (12) Zhang et al. (2010), (13) Kirkpatrick et al. (2011), (14) Bihain et al. (2013). Objects first published by other authors (and independently discovered by us) are detailed in Table 5.

Table 5. Spectral Types and Proper Motions of Previously Discovered Objects

Previous Observations					This Paper			
Name	References	SpT	$\mu_\alpha \cos \delta$ (mas yr ⁻¹)	μ_δ (mas yr ⁻¹)	Name	SpT (visual)	$\mu_\alpha \cos \delta$ (mas yr ⁻¹)	μ_δ (mas yr ⁻¹)
Spectroscopically Confirmed Objects								
2MASS J00135882−1816462	Baron et al. (2015)	L1	-20 ± 41	-212 ± 37	PSO J003.4−18	L5 pec	-31 ± 12	-175 ± 13
WISE J003110.04+574936.3	Thompson et al. (2013)	L8	530 ± 10	-10 ± 10	PSO J007.7+57	L9	526 ± 2	-12 ± 4
	Best et al. (2013) (Paper I)	L9	523 ± 17	-1 ± 16				
Hya12	Hogan et al. (2008)	L ^a	112.04 ± 7^b	-17.86 ± 7^b	PSO J068.9+13	L6 (red)	108 ± 9	-14 ± 10
	Lodieu et al. (2014)	L3.5	101 ± 11	-15 ± 11				
WISE J044633.45−242956.8	Thompson et al. (2013)	L5 pec (blue)	-210 ± 20	410 ± 20	PSO J071.6−24	L6 (blue)	-199 ± 13	398 ± 16
WISE J064205.58+410155.5	Mace et al. (2013)	extremely red	PSO J100.5+41	L9 (red)	12 ± 4	-372 ± 6
PSO J103.0927+41.4601	Best et al. (2013) (Paper I)	T0	-8 ± 6	-38 ± 6	PSO J103.0+41	T0	3 ± 3	-32 ± 6
WISE J070159.79+632129.2	Mace et al. (2013)	T3	PSO J105.4+63	T2.5	-14 ± 2	-264 ± 5
SDSS J074838.61+174332.9	Zhang et al. (2009)	L7 ^a	-70 ± 20	-10 ± 20	PSO J117.1+17	L5	-63 ± 5	8 ± 6
	Bardalez Gagliuffi et al. (2014)	L6				
ULAS J090521.61+100654.9	Marocco et al. (2015)	T0	PSO J136.3+10	T1	-8 ± 11	-118 ± 8
WISE J092055.40+453856.3	Aberasturi et al. (2011)	L4-5 ^a	-75 ± 10	-833 ± 45	PSO J140.2+45	L9.5	-77 ± 4	-852 ± 5
	Mace et al. (2013)	L9 sb?				
	Best et al. (2013) (Paper I)	L9.5	-42 ± 23	-843 ± 23				
WISE J125015.56+262846.9	Mace et al. (2013)	T6.5	PSO J192.5+26	T6	-514 ± 35	-621 ± 33
	Cardoso et al. (2015)	T6.5 ^c	-456 ± 18	-580 ± 26				
ULAS J152502.10+083344.0	Marocco et al. (2015)	T2	PSO J231.2+08	T2:	24 ± 8	-77 ± 9
WISE J173421.02+502349.9	Mace et al. (2013)	T4	PSO J263.5+50	T4	-19 ± 8	293 ± 15

Table 5—Continued

Previous Observations					This Paper			
Name	References	SpT	$\mu_\alpha \cos \delta$ (mas yr ⁻¹)	μ_δ (mas yr ⁻¹)	Name	SpT (visual)	$\mu_\alpha \cos \delta$ (mas yr ⁻¹)	μ_δ (mas yr ⁻¹)
WISE J175510.28+180320.2	Mace et al. (2013)	T2	PSO J268.7+18	T2.5	-424 ± 7	10 ± 9
	Luhman & Sheppard (2014)	T2	-453 ± 14	-8 ± 14				
WISE J180952.53-044812.5	Mace et al. (2013)	T0.5	PSO J272.4-04	T1	-46 ± 4	-400 ± 13
	Best et al. (2013) (Paper I)	T1	-62 ± 18	-429 ± 17				
WISEPA J183058.57+454257.9	Kirkpatrick et al. (2011)	L9	56 ± 22	107 ± 22	PSO J277.7+45	L9	105 ± 6	133 ± 7
WISE J185101.83+593508.6	Thompson et al. (2013)	L9 pec	40 ± 10	420 ± 10	PSO J282.7+59	L9	32 ± 3	421 ± 6
	Best et al. (2013) (Paper I)	L9	23 ± 19	412 ± 19				
WISE J191915.54+304558.4	Thompson et al. (2013)	L6	370 ± 10	400 ± 10	PSO J289.8+30	L9	386 ± 4	421 ± 5
WISE J203042.79+074934.7	Mace et al. (2013)	T1.5	PSO J307.6+07	T1.5	652 ± 5	-113 ± 6
	Bihain et al. (2013)	T1.5	653 ± 6	-138 ± 16				
	Best et al. (2013) (Paper I)	T1.5	659 ± 8	-113 ± 9				
WISE J204356.42+622048.9	Mace et al. (2013)	T1.5	PSO J310.9+62	T1.5	298 ± 2	515 ± 5
WISE J223617.59+510551.9	Mace et al. (2013)	T5.5	PSO J339.0+51	T5	732 ± 4	328 ± 5
	Best et al. (2013) (Paper I)	T5	736 ± 14	330 ± 8				
WISE J233527.07+451140.9	Thompson et al. (2013)	L9 pec (v. red)	-70 ± 20	-60 ± 20	PSO J353.8+45	L7.5	-84 ± 4	-66 ± 5
Photometric Candidates Confirmed By Our Spectroscopy								
SDSS J090308.17+165935.5	Zhang et al. (2009)	L6 ^a	90 ± 40	-70 ± 40	PSO J135.7+16	T0 pec	25 ± 14	-24 ± 17
SDSS J110827.31+083801.8	Zhang et al. (2009)	L8.5 ^a	-200 ± 80	-270 ± 80	PSO J167.1+08	L8	-246 ± 17	-313 ± 17
SDSS J122608.20+215010.9	Zhang et al. (2010)	L0 ^a	-21 ± 45	-28 ± 45	PSO J186.5+21	M9	-23 ± 22	-26 ± 25

Note. — Uncertainties for our visual spectral types are ± 0.5 subtypes, except for those listed with : (± 1.0 subtype) or :: ($\geq \pm 1.5$ subtypes).

^aBased on photometry only.

^bHogan et al. (2008) report typical proper motion errors of ± 7 mas yr⁻¹.

^cDerived from CH₄s-CH₄l photometry.

Table 6. Non-ultracool Interlopers

Name	Probable Type ^a	Description ^b
PSO J010.2+41	carbon star	Carbon star in the direction of NGC 205
PSO J249.4−10	RBO	Nondescript continuum broadly peaked in J band
PSO J255.6+10	galaxy	Flat continuum with strong emission features at $\approx 1.05 \mu\text{m}$, $\approx 1.75 \mu\text{m}$, and $\approx 2.05 \mu\text{m}$
PSO J342.9−09	unknown	Nondescript continuum, flux decreases with wavelength (low S/N)
PSO J276.0−01	RBO	Nondescript continuum broadly peaked in H band, wide absorption feature at $\approx 1.8 \mu\text{m}$. $b = 5.1^\circ$
PSO J202.5−26	K2 V	Good match to the SpeX Spectral Library K2 V standard HD 3765 (Rayner et al. 2009)
PSO J053.3+30	RBO	Nondescript continuum sharply peaked in H band
PSO J068.3+52	RBO	Sharp peaks in J, H, and K bands. $b = 3.1^\circ$
PSO J076.1+25	RBO	Nondescript continuum sharply peaked in H band. $b = -9.7^\circ$
PSO J085.3+36	RBO	Nondescript continuum sharply peaked in H band. $b = 3.1^\circ$
PSO J303.7+31	RBO	Nondescript continuum broadly peaked in J band. $b = -1.6^\circ$
PSO J296.0+35	K5 V	Good match to the SpeX Spectral Library K5 V standard HD 36003 (Rayner et al. 2009)

^aRBO = Reddened background object (likely a giant or supergiant star).

^bFive of these objects lie within 10° of the galactic plane. Their galactic latitudes (b) are indicated.

Table 7. New Near-infrared Spectral Types

Object Name	Opt SpT	Opt Ref	NIR SpT
2MASS J09153413+0422045	L6 ^a	Reid et al. (2008)	L5
2MASSW J1239272+551537	L5	Kirkpatrick et al. (2000)	L5

^aBinary brown dwarf (Reid et al. 2006); both components have spectral type L6.

Table 8. Index-based Spectral Types from Allers & Liu (2013a) for M7–L8 Objects

Name	Index-derived Spectral Types					Adopted
	H ₂ O	H ₂ OD	H ₂ O–1	H ₂ O–2	SpT ^a (avg.)	SpT (visual) ^b
M Dwarfs						
PSO J024.1+37 ^c	M7
PSO J101.8+39	M7.6 ^{+2.1} _{–1.9}	...	M6.6 ^{+1.5} _{–1.5}	M9.3 ^{+1.6} _{–1.6}	M8.2 ^{+1.4} _{–1.2}	M9.5
PSO J115.0+59	M9.0 ^{+2.2} _{–2.3}	...	M7.9 ^{+1.4} _{–1.4}	M7.3 ^{+1.9} _{–1.8}	M8.3 ^{+1.5} _{–1.5}	M9.5
PSO J133.8+06	M8.0 ^{+0.7} _{–0.7}	...	M6.5 ^{+1.2} _{–1.2}	M8.2 ^{+0.7} _{–0.7}	M8.0 ^{+0.5} _{–0.5}	M9
PSO J174.6–18	L0.1 ^{+1.4} _{–1.4}	...	M8.3 ^{+1.3} _{–1.4}	M9.5 ^{+1.6} _{–1.8}	M9.7 ^{+1.0} _{–1.0}	M9
PSO J186.5+21	L0.8 ^{+1.9} _{–2.0}	...	M6.9 ^{+1.5} _{–1.5}	M9.4 ^{+1.7} _{–1.7}	L0.0 ^{+1.3} _{–1.4}	M9
PSO J304.7–07	L0.4 ^{+1.3} _{–1.3}	M8.4 ^{+1.7} _{–1.7}	M8.8 ^{+1.4} _{–1.4}	M9
PSO J337.4+16	L1.1 ^{+1.7} _{–1.8}	...	M8.5 ^{+1.3} _{–1.3}	M8.1 ^{+1.5} _{–1.5}	M9.8 ^{+1.1} _{–1.2}	M9
L Dwarfs						
PSO J003.4–18	...	L4.7 ^{+0.9} _{–0.9}	L3.2 ^{+1.2} _{–1.2}	...	L4.2 ^{+0.7} _{–0.7}	L5 pec
PSO J004.7+51	...	L5.4 ^{+0.8} _{–0.8}	L5.4 ^{+0.8} _{–0.8}	L7
PSO J048.9+07	...	L7.6 ^{+1.3} _{–1.2}	L7.6 ^{+1.3} _{–1.2}	L6: (blue)
PSO J054.8–11	L0.9 ^{+1.6} _{–1.7}	L2.7 ^{+1.1} _{–1.2}	M8.1 ^{+1.4} _{–1.5}	...	L1.0 ^{+1.2} _{–1.3}	L3:
PSO J057.2+15	...	L2.0 ^{+0.9} _{–0.9}	L2.0 ^{+0.9} _{–0.9}	L7 (red)
PSO J068.9+13	...	L4.6 ^{+0.8} _{–0.8}	L4.6 ^{+0.8} _{–0.8}	L6 (red)
PSO J071.4+36	...	L6.4 ^{+0.9} _{–0.9}	L6.4 ^{+0.9} _{–0.9}	L6:
PSO J071.6–24	...	L6.4 ^{+1.3} _{–1.3}	L6.4 ^{+1.3} _{–1.3}	L6 (blue)
PSO J078.9+31	L1.6 ^{+1.0} _{–1.0}	...	L1.6 ^{+1.1} _{–1.1}	M9.0 ^{+1.0} _{–1.0}	L0.7 ^{+0.7} _{–0.7}	L1.5
PSO J087.7–12	...	L6.6 ^{+1.0} _{–0.9}	L6.6 ^{+1.0} _{–0.9}	L8
PSO J088.0+43	L3.3 ^{+0.9} _{–1.1}	L3.8 ^{+0.9} _{–1.0}	L1.5 ^{+1.2} _{–1.2}	...	L3.2 ^{+0.7} _{–0.8}	L4 pec
PSO J088.3–24 ^c	L1:
PSO J108.4+38	...	L6.0 ^{+0.9} _{–0.9}	L6.0 ^{+0.9} _{–0.9}	L7
PSO J117.1+17	...	L5.3 ^{+0.8} _{–0.8}	L3.2 ^{+1.2} _{–1.2}	...	L4.6 ^{+0.7} _{–0.7}	L5
PSO J127.4+10	L2.5 ^{+1.0} _{–1.1}	L3.6 ^{+0.9} _{–0.8}	L0.1 ^{+1.3} _{–1.3}	...	L2.5 ^{+0.8} _{–0.8}	L4
PSO J135.0+32	L1.5 ^{+0.6} _{–0.6}	L0.2 ^{+0.8} _{–0.8}	L0.7 ^{+1.1} _{–1.1}	L0.4 ^{+0.6} _{–0.6}	L0.9 ^{+0.4} _{–0.4}	L1.5
PSO J136.5–06	L3.5 ^{+0.5} _{–0.6}	L3.5 ^{+0.8} _{–0.8}	L2.3 ^{+1.1} _{–1.1}	L0.0 ^{+0.7} _{–0.7}	L2.4 ^{+0.4} _{–0.4}	L2 pec
PSO J143.6–29	...	L3.5 ^{+1.7} _{–1.8}	L2.4 ^{+1.4} _{–1.4}	...	L3.1 ^{+1.2} _{–1.3}	L1
PSO J146.0+05	L1.6 ^{+1.2} _{–1.3}	L2.8 ^{+1.1} _{–1.2}	L1.2 ^{+1.2} _{–1.2}	L0.7 ^{+1.1} _{–1.3}	L1.5 ^{+0.7} _{–0.8}	L1
PSO J147.5–27	L0.1 ^{+1.8} _{–1.9}	...	M9.7 ^{+1.3} _{–1.4}	...	L0.0 ^{+1.6} _{–1.7}	L0.5
PSO J149.1–19	...	L6.2 ^{+0.8} _{–0.8}	L4.6 ^{+1.1} _{–1.1}	...	L5.7 ^{+0.7} _{–0.7}	L5 pec
PSO J152.2+15	L3.2 ^{+0.9} _{–1.5}	L3.3 ^{+1.3} _{–1.4}	L1.8 ^{+1.3} _{–1.3}	L0.9 ^{+1.2} _{–1.6}	L2.2 ^{+1.0} _{–1.1}	L1.5
PSO J158.1+05	L2.3 ^{+0.7} _{–0.7}	L1.9 ^{+0.9} _{–0.9}	L2.8 ^{+1.1} _{–1.1}	L1.0 ^{+0.9} _{–0.9}	L1.9 ^{+0.5} _{–0.5}	L2
PSO J159.0–27	...	L4.7 ^{+1.1} _{–1.1}	L3.0 ^{+1.2} _{–1.2}	...	L4.2 ^{+0.8} _{–0.8}	L2 (blue)
PSO J167.1+08	...	L8.2 ^{+1.0} _{–0.9}	L8.2 ^{+1.0} _{–0.9}	L8
PSO J175.2+16	...	L6.3 ^{+1.1} _{–1.1}	L1.7 ^{+1.4} _{–1.4}	...	L4.8 ^{+0.9} _{–0.8}	L5
PSO J182.6–26	L2.9 ^{+1.1} _{–1.5}	L2.6 ^{+1.2} _{–1.3}	M9.7 ^{+1.3} _{–1.3}	...	L2.3 ^{+1.0} _{–1.2}	L3:
PSO J183.9–09	L0.8 ^{+1.5} _{–1.5}	L3.5 ^{+1.2} _{–1.3}	M7.7 ^{+1.4} _{–1.5}	M9.8 ^{+1.5} _{–1.7}	L0.6 ^{+0.9} _{–0.9}	L0
PSO J218.5–27	...	L4.7 ^{+0.9} _{–1.0}	L2.1 ^{+1.2} _{–1.2}	...	L3.9 ^{+0.8} _{–0.8}	L6

Table 8—Continued

Name	Index-derived Spectral Types					Adopted SpT (visual) ^b
	H ₂ O	H ₂ OD	H ₂ O–1	H ₂ O–2	SpT ^a (avg.)	
PSO J282.5+34	L2.1 ^{+1.3} _{–1.4}	L2.3 ^{+1.1} _{–1.2}	M8.8 ^{+1.3} _{–1.3}	L1.5 ^{+0.8} _{–1.1}	L1.7 ^{+0.8} _{–0.9}	L1
PSO J308.9–09	...	L6.9 ^{+1.1} _{–1.1}	L2.6 ^{+1.2} _{–1.2}	...	L5.5 ^{+0.9} _{–0.8}	L4.5
PSO J313.1–26	L0.6 ^{+1.7} _{–1.8}	L2.3 ^{+1.3} _{–1.4}	M9.7 ^{+1.4} _{–1.4}	L0.9 ^{+1.1} _{–1.5}	L0.8 ^{+1.0} _{–1.1}	L1
PSO J316.5+04	...	L5.5 ^{+0.9} _{–0.9}	L5.5 ^{+0.9} _{–0.9}	L6 (blue)
PSO J331.9–07	...	L5.0 ^{+0.8} _{–0.8}	L5.0 ^{+0.8} _{–0.8}	L7
PSO J334.8+11	...	L5.2 ^{+0.8} _{–0.8}	L3.4 ^{+1.1} _{–1.1}	...	L4.6 ^{+0.7} _{–0.7}	L5
PSO J336.9–18	...	L2.6 ^{+0.9} _{–0.9}	L1.0 ^{+1.2} _{–1.2}	...	L2.1 ^{+0.7} _{–0.7}	L6:: (red)
PSO J338.8+31	...	L5.2 ^{+0.9} _{–0.9}	L4.7 ^{+1.1} _{–1.1}	L0.1 ^{+1.1} _{–1.1}	L2.1 ^{+0.7} _{–0.7}	L2 pec
PSO J341.7–15	...	L6.0 ^{+0.8} _{–0.8}	L2.8 ^{+1.1} _{–1.1}	...	L5.0 ^{+0.7} _{–0.7}	L5
PSO J342.3–16	...	L6.3 ^{+0.8} _{–0.8}	L4.6 ^{+1.1} _{–1.1}	...	L5.7 ^{+0.7} _{–0.7}	L5: pec
PSO J344.8+20	L2.7 ^{+0.9} _{–1.0}	L2.8 ^{+0.9} _{–0.8}	L1.9 ^{+1.2} _{–1.2}	...	L2.6 ^{+0.7} _{–0.7}	L2.5
PSO J346.5–15	...	L5.0 ^{+0.9} _{–0.9}	L5.0 ^{+0.9} _{–0.9}	L7
PSO J348.8+06	L0.8 ^{+0.6} _{–0.7}	...	M9.7 ^{+1.2} _{–1.2}	M9.2 ^{+0.7} _{–0.6}	L0.2 ^{+0.4} _{–0.4}	L2
PSO J350.4–19	...	L5.7 ^{+0.9} _{–0.9}	L4.7 ^{+1.2} _{–1.2}	...	L5.4 ^{+0.7} _{–0.7}	L4.5
PSO J353.0–29	...	L1.9 ^{+1.7} _{–1.6}	M9.5 ^{+1.6} _{–1.6}	...	L0.8 ^{+1.4} _{–1.5}	L1:
PSO J353.6+13	...	L6.4 ^{+0.8} _{–0.8}	L6.4 ^{+0.8} _{–0.8}	L8:
PSO J353.8+45	...	L7.4 ^{+0.8} _{–0.8}	L7.4 ^{+0.8} _{–0.8}	L7.5

Note. — None of these indices are valid for spectral types later than L8, so objects with those spectral types are not listed here.

^aCalculated as the weighted average of the spectral types from Monte Carlo simulations for all indices, excluding those that fell outside the valid range for each index.

^bSpectral types determined by visual comparison with spectral standards, which we adopt as the final spectral types for our discoveries. Uncertainties for these visual spectral types are ± 0.5 subtypes, except for those listed with : (± 1.0 subtype) or :: ($\geq \pm 1.5$ subtypes).

^cNo indices yielded spectral types within the valid range of any index for this object, so no average spectral type was derived.

Table 9. Index-based Spectral Types from Burgasser et al. (2006) for L0–T7 Objects

Name	Index Values (Derived Spectral Types) ^a						Adopted
	H ₂ O- <i>J</i>	CH ₄ - <i>J</i>	H ₂ O- <i>H</i>	CH ₄ - <i>H</i>	CH ₄ - <i>K</i>	SpT (avg.)	SpT (visual) ^b
L Dwarfs							
PSO J003.4–18	0.693 (L7.5)	0.780 (<T0)	0.703 (L6.4)	0.934 (T1.3)	0.924 (L6.8)	L8.0±2.3	L5 pec
PSO J004.7+51	0.667 (L8.3)	0.783 (<T0)	0.721 (L5.7)	1.136 (<T1)	1.007 (L4.2)	L6.1±2.1	L7
PSO J007.7+57	0.659 (L8.5)	0.834 (<T0)	0.665 (L7.8)	1.047 (<T1)	0.844 (L8.7)	L8.4±0.5	L9
PSO J007.9+33	0.697 (L7.4)	0.747 (<T0)	0.658 (L8.1)	1.009 (<T1)	0.899 (L7.5)	L7.6±0.4	L9
PSO J023.8+02	0.662 (L8.4)	0.742 (<T0)	0.625 (L9.2)	1.069 (<T1)	0.870 (L8.2)	L8.6±0.5	L9.5
PSO J041.5+01	0.680 (L7.9)	0.866 (<T0)	0.646 (L8.5)	0.998 (T1.0)	0.875 (L8.0)	L8.1±0.3	L8.5
PSO J048.9+07	0.794 (L4.4)	0.905 (<T0)	0.674 (L7.5)	1.029 (<T1)	0.914 (L7.1)	L6.3±1.7	L6: (blue)
PSO J049.1+17	0.635 (L9.2)	0.751 (<T0)	0.611 (L9.6)	0.996 (T1.0)	0.869 (L8.2)	L9.0±0.7	L9.5
PSO J052.7–03	0.600 (T0.1)	0.747 (<T0)	0.590 (T0.2)	1.081 (<T1)	0.862 (L8.3)	L9.6±1.1	L9:
PSO J054.8–11	0.823 (L3.5)	0.963 (<T0)	0.798 (L2.7)	1.147 (<T1)	1.092 (L0.5)	L2.2±1.6	L3:
PSO J057.2+15	0.671 (L8.2)	1.015 (<T0)	0.729 (L5.4)	1.155 (<T1)	1.092 (L0.5)	L4.7±3.9	L7 (red)
PSO J068.9+13	0.760 (L5.5)	0.966 (<T1)	0.735 (L5.2)	1.110 (<T2)	1.063 (L1.9)	L4.2±2.0	L6 (red)
PSO J071.4+36	0.725 (L6.5)	0.861 (<T0)	0.674 (L7.5)	1.098 (<T1)	0.962 (L5.7)	L6.6±0.9	L6:
PSO J071.6–24	0.746 (L5.9)	0.792 (<T0)	0.742 (L4.9)	0.982 (T1.1)	0.864 (L8.3)	L6.4±1.7	L6 (blue)
PSO J078.9+31	0.894 (L1.6)	0.899 (<T0)	0.814 (L2.0)	1.132 (<T1)	1.112 (<L0)	L1.8±0.3	L1.5
PSO J087.7–12	0.719 (L6.7)	0.861 (<T0)	0.745 (L4.8)	1.064 (<T1)	0.935 (L6.5)	L6.0±1.1	L8
PSO J088.0+43	0.703 (L7.2)	0.827 (<T0)	0.731 (L5.4)	1.002 (<T1)	1.029 (L3.3)	L5.3±2.0	L4 pec
PSO J088.3–24	0.821 (L3.6)	0.935 (<T0)	0.730 (L5.4)	0.934 (T1.3)	1.182 (<L0)	L6.8±4.1	L1:
PSO J100.5+41	0.561 (T1.0)	0.754 (<T0)	0.598 (L10.0)	1.044 (<T1)	0.841 (L8.8)	L9.9±1.1	L9 (red)
PSO J108.4+38	0.722 (L6.6)	0.859 (<T0)	0.672 (L7.6)	1.107 (<T1)	1.002 (L4.3)	L6.2±1.7	L7
PSO J117.1+17	0.720 (L6.7)	0.838 (<T0)	0.700 (L6.5)	1.065 (<T1)	0.974 (L5.3)	L6.2±0.8	L5
PSO J127.4+10	0.830 (L3.3)	0.904 (<T0)	0.739 (L5.0)	1.136 (<T1)	1.053 (L2.3)	L3.6±1.4	L4
PSO J135.0+32	0.932 (L0.7)	0.908 (<T0)	0.825 (L1.6)	1.035 (<T1)	1.045 (L2.6)	L1.6±1.0	L1.5
PSO J136.5–06	0.792 (L4.5)	0.834 (<T0)	0.747 (L4.7)	0.961 (T1.2)	0.946 (L6.2)	L6.6±3.1	L2 pec
PSO J140.2+45	0.647 (L8.8)	0.874 (<T0)	0.608 (L9.7)	1.001 (<T1)	0.749 (T0.3)	L9.6±0.7	L9.5
PSO J143.6–29	0.849 (L2.8)	0.865 (<T0)	0.771 (L3.7)	1.076 (<T1)	1.047 (L2.5)	L3.0±0.6	L1
PSO J146.0+05	0.905 (L1.3)	0.851 (<T0)	0.800 (L2.6)	1.001 (<T1)	1.043 (L2.7)	L2.2±0.8	L1
PSO J147.5–27	0.919 (L1.0)	0.886 (<T0)	0.905 (<L0)	1.037 (<T1)	1.052 (L2.4)	L1.7±1.0	L0.5
PSO J149.0–14	0.581 (T0.6)	0.708 (<T0)	0.562 (T1.0)	1.014 (<T1)	0.770 (T0.0)	T0.5±0.5	L9
PSO J149.1–19	0.733 (L6.3)	0.766 (<T0)	0.679 (L7.3)	0.997 (T1.0)	0.907 (L7.3)	L7.0±0.6	L5 pec
PSO J152.2+15	0.872 (L2.1)	0.871 (<T0)	0.815 (L2.0)	1.025 (<T1)	0.971 (L5.4)	L3.2±1.9	L1.5
PSO J135.0+32	0.932 (L0.7)	0.908 (<T0)	0.825 (L1.6)	1.035 (<T1)	1.045 (L2.6)	L1.6±1.0	L1.5
PSO J159.0–27	0.850 (L2.7)	0.906 (<T0)	0.740 (L5.0)	1.127 (<T1)	1.087 (L0.7)	L2.8±2.1	L2 (blue)
PSO J167.1+08	0.707 (L7.1)	0.769 (<T0)	0.710 (L6.2)	1.046 (<T1)	0.882 (L7.9)	L7.1±0.9	L8
PSO J175.2+16	0.792 (L4.5)	0.840 (<T0)	0.726 (L5.6)	1.092 (<T1)	0.963 (L5.7)	L5.2±0.7	L5
PSO J182.6–26	0.862 (L2.4)	0.842 (<T0)	0.801 (L2.5)	1.074 (<T1)	1.001 (L4.4)	L3.1±1.1	L2
PSO J183.9–09	0.926 (L0.8)	0.907 (<T0)	0.828 (L1.4)	1.066 (<T1)	1.085 (L0.8)	L1.0±0.4	L0
PSO J218.5–27	0.754 (L5.7)	0.948 (<T0)	0.688 (L7.0)	1.119 (<T1)	1.021 (L3.6)	L5.4±1.7	L6
PSO J244.1+06	0.667 (L8.3)	0.796 (<T0)	0.662 (L7.9)	1.120 (<T1)	0.907 (L7.3)	L7.8±0.5	L9 (red)
PSO J260.3+46	0.709 (L7.0)	0.744 (<T0)	0.659 (L8.0)	1.011 (<T1)	0.825 (L9.1)	L8.0±1.0	L9

Table 9—Continued

Name	Index Values (Derived Spectral Types) ^a						Adopted SpT (visual) ^b
	H ₂ O- <i>J</i>	CH ₄ - <i>J</i>	H ₂ O- <i>H</i>	CH ₄ - <i>H</i>	CH ₄ - <i>K</i>	SpT (avg.)	
PSO J276.8+22	0.580 (T0.6)	0.738 (<T0)	0.618 (L9.4)	1.014 (<T1)	0.870 (L8.2)	L9.4±1.2	L9
PSO J277.7+45	0.659 (L8.5)	0.770 (<T0)	0.639 (L8.7)	0.979 (T1.1)	0.848 (L8.6)	L8.6±0.1	L9
PSO J280.2+63	0.667 (L8.3)	0.766 (<T0)	0.616 (L9.5)	0.996 (T1.0)	0.796 (L9.6)	L9.1±0.7	L9.5
PSO J282.5+34	0.931 (L0.7)	0.951 (<T0)	0.801 (L2.5)	1.114 (<T1)	1.070 (L1.5)	L1.6±0.9	L1
PSO J282.7+59	0.678 (L8.0)	0.653 (T0.0)	0.650 (L8.3)	1.016 (<T1)	0.897 (L7.5)	L7.9±0.4	L9
PSO J289.8+30	0.696 (L7.4)	0.809 (<T0)	0.744 (L4.8)	1.044 (<T1)	0.838 (L8.8)	L7.0±2.0	L9
PSO J308.9−09	0.852 (L2.7)	0.916 (<T0)	0.734 (L5.2)	1.089 (<T1)	0.998 (L4.5)	L4.1±1.3	L4.5
PSO J313.1−26	0.946 (L0.4)	0.909 (<T0)	0.806 (L2.3)	1.013 (<T1)	1.011 (L4.0)	L2.3±1.8	L1
PSO J316.5+04	0.748 (L5.9)	0.789 (<T0)	0.681 (L7.3)	1.057 (<T1)	0.957 (L5.9)	L6.3±0.8	L6 (blue)
PSO J321.1+18	0.567 (T0.9)	0.710 (<T0)	0.569 (T0.8)	1.048 (<T1)	0.761 (T0.1)	T0.6±0.4	L9
PSO J331.9−07	0.706 (L7.1)	0.872 (<T0)	0.700 (L6.5)	1.121 (<T1)	1.019 (L3.7)	L5.8±1.8	L7
PSO J334.8+11	0.733 (L6.3)	0.854 (<T0)	0.687 (L7.0)	1.102 (<T1)	1.021 (L3.6)	L5.6±1.8	L5
PSO J336.9−18	0.676 (L8.0)	0.957 (<T0)	0.705 (L6.3)	1.229 (<T1)	1.123 (<L0)	L7.2±1.2	L6:: (red)
PSO J338.8+31	0.827 (L3.4)	0.820 (<T0)	0.736 (L5.2)	1.005 (<T1)	0.957 (L5.9)	L4.8±1.3	L2 pec
PSO J341.7−15	0.742 (L6.0)	0.833 (<T0)	0.712 (L6.1)	1.074 (<T1)	1.035 (L3.0)	L5.0±1.7	L5
PSO J342.3−16	0.804 (L4.1)	0.834 (<T0)	0.720 (L5.8)	1.004 (<T1)	0.884 (L7.8)	L5.9±1.9	L5:
PSO J344.8+20	0.797 (L4.3)	0.912 (<T0)	0.752 (L4.5)	1.112 (<T1)	1.082 (L1.0)	L3.3±2.0	L2.5
PSO J346.3−11	0.690 (L7.6)	0.833 (<T0)	0.705 (L6.3)	1.035 (<T1)	0.912 (L7.1)	L7.0±0.6	L8.5
PSO J346.5−15	0.701 (L7.3)	0.857 (<T0)	0.693 (L6.8)	1.140 (<T1)	1.023 (L3.5)	L5.9±2.0	L7
PSO J348.8+06	0.879 (L2.0)	0.960 (<T0)	0.785 (L3.2)	1.138 (<T1)	1.083 (L0.9)	L2.0±1.2	L2
PSO J350.4−19	0.790 (L4.6)	0.823 (<T0)	0.729 (L5.4)	1.071 (<T1)	0.981 (L5.1)	L5.0±0.4	L4.5
PSO J353.0−29	0.981 (<L0)	0.987 (<T0)	0.701 (L6.5)	1.008 (<T1)	1.024 (L3.5)	L5.0±2.1	L1:
PSO J353.6+13	0.693 (L7.5)	0.836 (<T0)	0.693 (L6.8)	1.079 (<T1)	0.981 (L5.1)	L6.5±1.2	L8:
PSO J353.8+45	0.656 (L8.6)	0.831 (<T0)	0.663 (L7.9)	1.128 (<T1)	0.974 (L5.3)	L7.3±1.7	L7.5
T Dwarfs							
PSO J004.1+23	0.549 (T1.3)	0.628 (T0.7)	0.546 (T1.4)	1.011 (<T1)	0.796 (L9.6)	T0.7±0.8	T0
PSO J031.5+20	0.150 (T5.9)	0.320 (T6.2)	0.302 (T5.6)	0.363 (T5.5)	0.258 (T4.6)	T5.6±0.6	T5.5
PSO J049.1+26	0.387 (T3.8)	0.537 (T2.7)	0.468 (T3.1)	0.728 (T2.9)	0.537 (T2.3)	T3.0±0.6	T2.5
PSO J055.0−21	0.518 (T1.9)	0.733 (<T0)	0.501 (T2.5)	0.842 (T2.0)	0.572 (T2.1)	T2.1±0.2	T2
PSO J070.3+04	0.292 (T4.6)	0.574 (T2.0)	0.343 (T5.0)	0.449 (T4.9)	0.195 (T5.4)	T4.4±1.4	T4.5
PSO J071.8−12	0.469 (T2.7)	0.729 (<T0)	0.534 (T1.7)	0.768 (T2.5)	0.745 (T0.3)	T1.8±1.1	T2:
PSO J076.7+52	0.253 (T4.9)	0.454 (T4.2)	0.336 (T5.1)	0.499 (T4.5)	0.260 (T4.6)	T4.7±0.3	T4.5
PSO J103.0+41	0.588 (T0.4)	0.708 (<T0)	0.576 (T0.6)	0.982 (T1.1)	0.778 (L9.9)	T0.5±0.5	T0
PSO J105.4+63	0.435 (T3.2)	0.660 (<T0)	0.462 (T3.2)	0.732 (T2.8)	0.586 (T2.0)	T2.8±0.6	T2.5
PSO J109.4+46	0.651 (L8.7)	0.750 (<T0)	0.540 (T1.6)	0.895 (T1.6)	0.888 (L7.7)	L9.9±2.0	T0
PSO J133.8−02	0.588 (T0.4)	0.673 (<T0)	0.627 (L9.1)	0.882 (T1.7)	0.798 (L9.6)	T0.2±1.1	T0 pec
PSO J135.7+16	0.548 (T1.3)	0.714 (<T0)	0.588 (T0.3)	0.897 (T1.6)	0.852 (L8.6)	T0.4±1.4	T0 pec
PSO J136.3+10	0.613 (L9.8)	0.667 (<T0)	0.559 (T1.1)	0.861 (T1.8)	0.675 (T1.2)	T1.0±0.9	T1
PSO J159.2−26	0.502 (T2.2)	0.619 (T0.9)	0.568 (T0.8)	0.862 (T1.8)	0.693 (T1.0)	T1.4±0.6	T1.5
PSO J160.0−21	0.456 (T2.9)	0.595 (T1.5)	0.550 (T1.3)	0.750 (T2.7)	0.647 (T1.4)	T2.0±0.8	T2 pec
PSO J168.1−27	0.547 (T1.3)	0.667 (<T0)	0.517 (T2.1)	0.753 (T2.7)	0.391 (T3.4)	T2.4±0.9	T2.5

Table 9—Continued

Name	Index Values (Derived Spectral Types) ^a						Adopted SpT (visual) ^b
	H ₂ O- <i>J</i>	CH ₄ - <i>J</i>	H ₂ O- <i>H</i>	CH ₄ - <i>H</i>	CH ₄ - <i>K</i>	SpT (avg.)	
PSO J175.8–20	0.573 (T0.7)	0.580 (T1.8)	0.521 (T2.0)	0.838 (T2.0)	0.551 (T2.2)	T1.8±0.6	T2
PSO J180.1–28	0.711 (L7.0)	0.874 (<T0)	0.646 (L8.5)	0.976 (T1.1)	0.733 (T0.5)	L8.7±1.8	T0
PSO J183.4+40	0.387 (T3.8)	0.472 (T3.9)	0.385 (T4.5)	0.595 (T3.9)	0.195 (T5.4)	T4.3±0.7	T4
PSO J192.5+26	0.148 (T5.9)	0.383 (T5.3)	0.269 (T6.1)	0.241 (T6.5)	0.104 (≥T7)	T6.0±0.5	T6
PSO J192.6–21	0.556 (T1.1)	0.708 (<T0)	0.523 (T2.0)	0.783 (T2.4)	0.547 (T2.2)	T1.9±0.6	T2.5
PSO J202.1–03	0.218 (T5.2)	0.492 (T3.6)	0.280 (T5.9)	0.492 (T4.6)	0.219 (T5.1)	T4.9±0.9	T4.5
PSO J207.7+29	0.497 (T2.3)	0.656 (<T0)	0.614 (L9.5)	0.923 (T1.4)	0.840 (L8.8)	T0.5±1.6	T0: pec
PSO J218.4+50	0.440 (T3.2)	0.420 (T4.8)	0.584 (T0.4)	0.723 (T2.9)	0.552 (T2.2)	T2.7±1.6	T2.5
PSO J224.3+47	0.109 (T6.5)	0.265 (T6.9)	0.256 (T6.3)	0.238 (T6.5)	0.106 (≥T7)	T6.6±0.3	T7
PSO J231.2+08	0.468 (T2.8)	0.638 (T0.4)	0.517 (T2.1)	0.910 (T1.5)	0.636 (T1.5)	T1.7±0.9	T2:
PSO J241.1+39	0.523 (T1.8)	0.630 (T0.6)	0.572 (T0.8)	0.807 (T2.2)	0.602 (T1.8)	T1.5±0.7	T2
PSO J242.9+02	0.585 (T0.4)	0.716 (<T0)	0.594 (T0.1)	0.923 (T1.4)	0.648 (T1.4)	T0.9±0.7	T1
PSO J244.6+08	0.341 (T4.2)	0.528 (T2.9)	0.355 (T4.9)	0.571 (T4.0)	0.246 (T4.7)	T4.2±0.8	T4.5
PSO J258.2+06	0.532 (T1.6)	0.639 (T0.4)	0.636 (L8.8)	0.820 (T2.1)	0.773 (L9.9)	T0.6±1.3	T0 pec
PSO J260.1+61	0.636 (L9.2)	0.505 (T3.3)	0.561 (T1.0)	0.941 (T1.3)	0.588 (T1.9)	T1.4±1.5	T2
PSO J261.2+22	0.212 (T5.2)	0.342 (T5.9)	0.376 (T4.6)	0.418 (T5.1)	0.168 (T5.8)	T5.3±0.5	T5
PSO J263.5+50	0.380 (T3.9)	0.392 (T5.2)	0.456 (T3.3)	0.523 (T4.4)	0.216 (T5.1)	T4.4±0.8	T4
PSO J265.0+11	0.607 (L9.9)	0.685 (<T0)	0.567 (T0.9)	1.053 (<T1)	0.802 (L9.5)	T0.1±0.7	T0.5
PSO J268.7+18	0.552 (T1.2)	0.679 (<T0)	0.547 (T1.4)	0.887 (T1.7)	0.552 (T2.2)	T1.6±0.4	T2.5
PSO J272.0–04	0.471 (T2.7)	0.640 (T0.4)	0.513 (T2.2)	1.013 (<T1)	0.700 (T0.9)	T1.6±1.1	T1.5 pec
PSO J272.4–04	0.657 (L8.6)	0.772 (<T0)	0.630 (L9.0)	0.972 (T1.1)	0.720 (T0.7)	L9.4±1.1	T1
PSO J274.0+30	0.452 (T3.0)	0.527 (T2.9)	0.504 (T2.4)	0.651 (T3.5)	0.401 (T3.3)	T3.0±0.4	T3
PSO J284.7+39	0.318 (T4.4)	0.417 (T4.8)	0.428 (T3.8)	0.641 (T3.5)	0.396 (T3.3)	T4.0±0.6	T4
PSO J291.2+68	0.660 (L8.5)	0.795 (<T0)	0.621 (L9.3)	1.023 (<T1)	0.708 (T0.8)	L9.5±1.2	T1
PSO J307.6+07	0.625 (L9.4)	0.698 (<T0)	0.586 (T0.4)	0.878 (T1.7)	0.548 (T2.2)	T0.9±1.3	T1.5
PSO J310.9+62	0.567 (T0.9)	0.600 (T1.4)	0.565 (T0.9)	0.897 (T1.6)	0.649 (T1.4)	T1.2±0.3	T1.5
PSO J319.3–29	0.669 (L8.2)	0.772 (<T0)	0.619 (L9.3)	0.955 (T1.2)	0.744 (T0.4)	L9.8±1.3	T0:
PSO J329.8+03	0.556 (T1.1)	0.642 (T0.3)	0.508 (T2.3)	1.102 (<T1)	0.689 (T1.0)	T1.2±0.8	T1:
PSO J330.3+32	0.496 (T2.3)	0.649 (T0.1)	0.541 (T1.5)	0.763 (T2.6)	0.628 (T1.6)	T1.6±0.9	T2.5
PSO J331.6+33	0.588 (T0.4)	0.684 (<T0)	0.531 (T1.8)	0.915 (T1.5)	0.572 (T2.1)	T1.4±0.7	T1.5
PSO J334.1+19	0.425 (T3.4)	0.619 (T0.9)	0.406 (T4.2)	0.708 (T3.0)	0.425 (T3.1)	T2.9±1.2	T3
PSO J339.0+51	0.225 (T5.1)	0.405 (T5.0)	0.336 (T5.1)	0.411 (T5.2)	0.203 (T5.3)	T5.1±0.1	T5
PSO J357.8+49	0.707 (L7.1)	0.735 (<T0)	0.677 (L7.4)	0.945 (T1.3)	0.833 (L8.9)	L8.7±1.9	T0 (blue)
PSO J359.8–01	0.643 (L9.0)	0.777 (<T0)	0.628 (L9.1)	0.952 (T1.2)	0.767 (T0.0)	L9.8±1.1	T1

^aSpectral types were calculated using the polynomials defined in Burgasser (2007).

^bSpectral types determined by visual comparison with spectral standards, which we adopt as the final spectral types for our discoveries. Uncertainties for these visual spectral types are ± 0.5 subtypes, except for those listed with : (± 1.0 subtype) or :: ($\geq \pm 1.5$ subtypes).

Table 10. Low-Resolution Gravity Indices from Allers & Liu (2013a)

Name	FeH _z	VO _z	KI _J	H-cont	Index Scores ^a	Gravity Score ^b	Gravity Class ^c	SpT (visual)
M dwarfs								
PSO J133.8+06	1.170 ^{+0.021} _{-0.021}	1.080 ^{+0.014} _{-0.014}	1.078 ^{+0.010} _{-0.010}	0.926 ^{+0.011} _{-0.011}	0n10 (0n?0)	0.0 ^{+1.0} _{-0.0}	FLD-G ^d	M9
PSO J337.4+16	1.110 ^{+0.040} _{-0.042}	1.103 ^{+0.027} _{-0.028}	1.026 ^{+0.022} _{-0.022}	0.936 ^{+0.028} _{-0.029}	1n20 (1n20)	1.0 ^{+1.0} _{-0.0}	[INT-G]	M9
L dwarfs								
PSO J068.9+13	1.355 ^{+0.043} _{-0.045}	1.037 ^{+0.019} _{-0.019}	1.120 ^{+0.015} _{-0.015}	0.884 ^{+0.012} _{-0.013}	nnn1 (nnn?)	1.0 ^{+0.0} _{-1.0}	[INT-G]	L6 (red)
PSO J078.9+31	1.051 ^{+0.027} _{-0.028}	1.251 ^{+0.023} _{-0.023}	1.048 ^{+0.016} _{-0.016}	0.945 ^{+0.017} _{-0.018}	2221 (222?)	2.0 ^{+0.0} _{-0.5}	VL-G	L1.5
PSO J117.1+17	1.299 ^{+0.068} _{-0.074}	0.951 ^{+0.026} _{-0.027}	1.118 ^{+0.016} _{-0.016}	0.859 ^{+0.014} _{-0.015}	0n00 (0n00)	0.0 ^{+0.0} _{-0.0}	FLD-G	L5
PSO J127.4+10	1.073 ^{+0.083} _{-0.092}	1.110 ^{+0.054} _{-0.058}	1.040 ^{+0.020} _{-0.020}	0.934 ^{+0.016} _{-0.016}	2121 (202?)	1.5 ^{+0.5} _{-0.0}	[VL-G]	L4
PSO J135.0+32	1.334 ^{+0.023} _{-0.023}	1.080 ^{+0.011} _{-0.011}	1.113 ^{+0.010} _{-0.010}	0.917 ^{+0.008} _{-0.008}	0011 (00??)	0.5 ^{+0.0} _{-0.0}	FLD-G	L1.5
PSO J136.5−06	1.263 ^{+0.019} _{-0.020}	1.009 ^{+0.009} _{-0.009}	1.076 ^{+0.006} _{-0.006}	0.822 ^{+0.006} _{-0.006}	1010 (10?0)	0.5 ^{+0.0} _{-0.0}	FLD-G	L2 pec ^e
PSO J146.0+05	1.128 ^{+0.040} _{-0.043}	1.066 ^{+0.023} _{-0.024}	1.084 ^{+0.018} _{-0.018}	0.889 ^{+0.023} _{-0.023}	1010 (10?0)	0.5 ^{+0.5} _{-0.0}	FLD-G ^d	L1 ^e
PSO J149.1−19	1.188 ^{+0.032} _{-0.034}	1.020 ^{+0.015} _{-0.015}	1.080 ^{+0.009} _{-0.009}	0.784 ^{+0.008} _{-0.008}	1n10 (1n?0)	1.0 ^{+0.0} _{-0.0}	[INT-G]	L5 pec ^e
PSO J158.1+05	1.331 ^{+0.039} _{-0.040}	1.093 ^{+0.017} _{-0.018}	1.131 ^{+0.014} _{-0.014}	0.937 ^{+0.013} _{-0.014}	0011 (00??)	0.5 ^{+0.5} _{-0.5}	FLD-G ^d	L2
PSO J159.0−27	1.187 ^{+0.044} _{-0.046}	1.131 ^{+0.030} _{-0.031}	1.107 ^{+0.021} _{-0.021}	0.902 ^{+0.022} _{-0.023}	1110 (11?0)	1.0 ^{+0.0} _{-0.5}	[INT-G]	L2 (blue)
PSO J316.5+04	1.173 ^{+0.046} _{-0.049}	0.948 ^{+0.023} _{-0.024}	1.090 ^{+0.018} _{-0.018}	0.816 ^{+0.017} _{-0.018}	nnn0 (nnn0)	0.0 ^{+0.0} _{-0.0}	FLD-G	L6 (blue)
PSO J331.9−07	1.038 ^{+0.058} _{-0.062}	0.983 ^{+0.033} _{-0.035}	1.052 ^{+0.018} _{-0.019}	0.873 ^{+0.018} _{-0.018}	nnn0 (nnn0)	0.0 ^{+1.0} _{-0.0}	[FLD-G ^d]	L7
PSO J334.8+11	1.243 ^{+0.046} _{-0.049}	0.998 ^{+0.022} _{-0.022}	1.080 ^{+0.017} _{-0.018}	0.860 ^{+0.012} _{-0.012}	1n10 (1n?0)	1.0 ^{+0.0} _{-1.0}	[INT-G]	L5
PSO J336.9−18	1.005 ^{+0.062} _{-0.067}	1.112 ^{+0.047} _{-0.048}	1.005 ^{+0.022} _{-0.023}	0.958 ^{+0.019} _{-0.019}	nnn2 (nnn2)	2.0 ^{+0.0} _{-1.0}	VL-G	L6:: (red)
PSO J338.8+31	1.329 ^{+0.059} _{-0.062}	1.033 ^{+0.026} _{-0.026}	1.079 ^{+0.019} _{-0.019}	0.824 ^{+0.017} _{-0.017}	0010 (00?0)	0.0 ^{+0.5} _{-0.0}	FLD-G	L2 pec ^e
PSO J341.7−15	1.242 ^{+0.044} _{-0.047}	1.009 ^{+0.025} _{-0.025}	1.125 ^{+0.015} _{-0.015}	0.847 ^{+0.015} _{-0.015}	1n00 (1n00)	0.0 ^{+0.0} _{-0.0}	FLD-G	L5
PSO J342.3−16	1.250 ^{+0.029} _{-0.030}	1.000 ^{+0.014} _{-0.014}	1.068 ^{+0.013} _{-0.014}	0.802 ^{+0.010} _{-0.010}	1n10 (1n?0)	1.0 ^{+0.0} _{-1.0}	[INT-G]	L5: pec ^e
PSO J344.8+20	1.232 ^{+0.055} _{-0.059}	1.144 ^{+0.035} _{-0.036}	1.071 ^{+0.018} _{-0.018}	0.913 ^{+0.016} _{-0.016}	1121 (112?)	1.0 ^{+0.0} _{-0.0}	INT-G	L2.5
PSO J348.8+06	1.093 ^{+0.071} _{-0.078}	1.326 ^{+0.056} _{-0.060}	1.036 ^{+0.015} _{-0.015}	0.987 ^{+0.011} _{-0.011}	2222 (2222)	2.0 ^{+0.0} _{-0.0}	VL-G	L2

Note. — This table includes M7–L7 discoveries for which our spectrum has high enough S/N to extract useful measurements of the AL13 gravity indices, corroborated by visual inspection. No AL13 index is valid for spectral types later than L7, so objects with those spectral types are not included.

^aScores in parentheses were determined using the original AL13 classification scheme, in which objects with index values corresponding to INT-G but within 1σ of the FLD-G value are classified with a score of “?”.

^bThe overall gravity classification value and the 68% confidence limits calculated as described in Allers et al. (2015).

^cGravity classes in brackets are based on lower-S/N spectra and could not be confirmed visually, and therefore should be considered tentative. Higher-S/N spectra are needed to clarify the gravity.

^dAlthough this object is classified as FLD-G under the AL13 system, we note that within the uncertainties in our gravity score, this object shows signs of intermediate gravity. A higher resolution spectrum is needed to more accurately classify the gravity of this object.

^eStrong or medium candidate binary (see text). The spectral type may therefore be based on a composite spectrum.

Table 11. Other Objects Showing Low Gravity Spectral Features

Name	SpT (visual)	Reason for No Gravity Class ^a	Youth ^b
PSO J004.7+51	L7	Low S/N	Red
PSO J054.8–11	L3:	Low S/N	H band; Red
PSO J057.2+15	L7 (red)	Low S/N	H band; Red
PSO J100.5+41 ^c	L9 (red)	SpT > L7	Red
PSO J244.1+06	L9 (red)	SpT > L7; Low S/N	Red
PSO J353.8+45	L7.5	SpT > L7	Red

^a“SpT > L7”: None of the AL13 spectral indices are defined for spectral types later than L7. “Low S/N”: Spectra with J band S/N < 30 produced AL13 gravity scores with uncertainties too large to yield useful results.

^b“Red”: Redder-than-normal near-IR colors for the spectral type. “H band”: Triangular H band profile.

^cPreviously identified by Mace et al. (2013) as an “extremely red” L dwarf, WISE 0642+4101, and by Gagné et al. (2014) as a candidate member of the AB Dor young moving group (Section 6.2).

Table 12. Candidate Binaries

Name	SpT (Visual)	BG14 ^a Criteria	B10 ^b Criteria	Visual Signs ^c
Strong Candidates				
PSO J003.4–18	L5 pec	10	...	Y
PSO J049.1+26	T2.5	...	4	Y
PSO J071.6–24	L6 (blue)	8	...	Y
PSO J088.0+43	L4 pec	9	...	Y
PSO J133.8–02	T0 pec	...	5	Y
PSO J135.7+16	T0 pec	...	6	Y
PSO J136.5–06	L2 pec	9	...	Y
PSO J149.1–19	L5 pec	10	...	Y
PSO J159.2–26	T1.5	...	4	Y
PSO J160.0–21	T2 pec	...	6	Y
PSO J207.7+29	T0: pec	...	6	Y
PSO J218.4+50	T2.5	...	5	Y
PSO J241.1+39	T2	...	5	Y
PSO J258.2+06	T0 pec	...	6	Y
PSO J330.3+32	T2.5	...	5	N
PSO J338.8+31	L2 pec	8	...	Y
Medium Candidates				
PSO J004.1+23	T0	...	2	Y
PSO J100.5+41	L9 (red)	...	3	N
PSO J103.0+41	T0	...	2	Y
PSO J105.4+63	T2.5	...	3	N
PSO J146.0+05	L1	4	...	N
PSO J152.2+15	L1.5	5	...	N
PSO J180.1–28	T0	...	1	Y
PSO J272.0–04	T1.5 pec	...	3	Y
PSO J277.7+45	L9	...	3	Y
PSO J284.7+39	T4	...	2	Y
PSO J319.3–29	T0:	...	2	Y
PSO J342.3–16	L5:	5	...	Y
Weak Candidates				
PSO J052.7–03	L9:	...		Y
PSO J282.7+59	L9	...		Y
PSO J321.1+18	L9	...		Y

Note. — Our spectra for all binary candidates listed above have $S/N \geq 25$ averaged over the J band ($1.20 - 1.31 \mu\text{m}$).

^aNumber of index based-criteria (out of 12) for binarity from Bardalez Gagliuffi et al. (2014) satisfied by this object’s spectrum. These indices apply only to M7–L7 dwarfs (we included our L7.5 dis-

coveries).

^bNumber of index based-criteria (out of 6) for binarity from Burgasser et al. (2010) satisfied by this object’s spectrum. These indices apply only to L8, L9, and T dwarfs.

^cSee text (Section 4.5) for descriptions.

Table 13. Common Proper Motion Pairings

Name	$\mu_\alpha \cos \delta$ (mas yr ⁻¹)	μ_δ (mas yr ⁻¹)	Dist. (pc)	SpT	r (arcsec)	r (AU)
NLTT 687 ^a	-33 ± 5	-173 ± 5^b	$42^{+26}_{-16}^c$	M3 ^c	120.3	5053
PSO J003.4950–18.2802	-31 ± 12	-175 ± 13	46.1 ± 5.6	L5 pec		
Wolf 1154	121.0 ± 4.1	62.0 ± 4.0^d	$27.5^{+11.9}_{-6.3}^e$	M1 ^f	77.1	2313
PSO J330.3214+32.3686	105 ± 8	65 ± 9	20.1 ± 2.1	T2.5		
LSPM J2216+1952	146 ± 8	-96 ± 8^g	$30.0^{+11.2}_{-8.2}^h$	M4	52.2	1566
PSO J334.1193+19.8800	120 ± 8	-72 ± 9	30.7 ± 3.2	T3		

^aThis pairing was previously discovered by Baron et al. (2015).^bSalim & Gould (2003)^cBaron et al. (2015)^dHøg et al. (2000)^eLépine & Gaidos (2011)^fEstimated from $V - J$ and the color-SpT relation of Lépine & Gaidos (2011).^gLépine & Shara (2005)^hEstimated using the distance relations of Lépine (2005).

Table 14. Candidate Members of Young Moving Groups

Name	SpT (visual)	$d_{\text{phot}}^{\text{a}}$ (pc)	$\mu_{\alpha} \cos \delta$ (mas yr $^{-1}$)	μ_{δ} (mas yr $^{-1}$)	Youth ^b	BANYAN II YMG	Prob. (%)	$\log(L_{\text{bol}}/L_{\odot})$ (dex)	Mass ^c (M_{Jup})
PSO J004.7148+51.8918	L7	26.4 ± 3.7	293 ± 4	-12 ± 7	Red	Argus	79.9	$-4.36^{+0.12}_{-0.14}$	$10.3^{+1.4}_{-1.2}$
PSO J007.7921+57.8267	L9	11.2 ± 1.5	526 ± 2	-12 ± 4	...	Argus	98.7	$-4.54^{+0.12}_{-0.13}$	$8.8^{+1.3}_{-1.1}$
PSO J057.2893+15.2433	L7 (red)	31.5 ± 4.4	68 ± 11	-127 ± 12	H band; Red	β Pictoris	92.0	$-4.36^{+0.12}_{-0.13}$	$8.1^{+1.8}_{-1.5}$
PSO J071.8769-12.2713	T2:	25.9 ± 3.1	20 ± 19	-89 ± 19	...	β Pictoris	86.4	$-4.69^{+0.13}_{-0.14}$	6.1 ± 0.7
PSO J076.7092+52.6087	T4.5	18.1 ± 4.4	57 ± 4	-196 ± 7	...	Argus	71.4	-4.8 ± 0.2	$7.0^{+1.5}_{-1.2}$
PSO J100.5233+41.0320 ^d	L9 (red)	18.5 ± 2.6	12 ± 4	-372 ± 6	Red	AB Doradus	78.6	$-4.54^{+0.12}_{-0.13}$	15^{+4}_{-3}
PSO J272.4689-04.8036	T1	13.1 ± 1.3	-46 ± 4	-400 ± 13	...	AB Doradus	93.8	-4.65 ± 0.09	14 ± 2
PSO J319.3102-29.6682	T0:	15.6 ± 1.6	148 ± 4	-162 ± 4	...	β Pictoris	97.1	$-4.60^{+0.10}_{-0.11}$	$6.5^{+0.7}_{-0.6}$
PSO J331.6058+33.0207	T1.5	28.3 ± 3.4	176 ± 9	16 ± 11	...	Argus	74.6	$-4.67^{+0.12}_{-0.13}$	$8.0^{+1.2}_{-1.0}$
PSO J334.1193+19.8800	T3	30.9 ± 3.6	119 ± 11	-60 ± 9	...	β Pictoris	84.4	$-4.73^{+0.12}_{-0.13}$	$5.9^{+0.7}_{-0.6}$

^aPhotometric distances calculated using K_{MKO} magnitudes and the polynomial from Dupuy & Liu (2012).

^b“Red”: Redder-than-normal near-IR colors for the spectral type. “H band”: Triangular H band profile.

^cMass estimates derived assuming the objects are members of the given YMGs. We used L_{bol} and the “hybrid” evolutionary models of Saumon & Marley (2008), following the method described in Section 6.2.1.

^dPreviously identified by Gagné et al. (2014, 2015b) as a candidate member of the AB Doradus Moving Group. First discovered as WISE 0642+4101 (Mace et al. 2013).